

Contents

1	Introduction	4
1.1	Properties of TMDCs	4
1.2	Electronic properties	5
1.3	Optical properties	7
1.4	Phonon dispersion	11
2	Role of precursors in growth of monolayer WS_2	13
2.1	Introduction	13
2.2	Results	14
2.3	Conclusions	28
3	WSe₂	30
3.1	Introduction	30
3.2	Results	30
4	Transfer	37
4.1	Introduction	37
4.2	Experimental	37
4.3	Results	37
4.4	Conclusions	39
5	Low T PL	43
5.1	Introduction	43
5.2	Experimental	43
5.3	Results	43
6	1T' WSe_2	47
6.1	Introduction	47
7	TMDC phases - review	48
7.1	Introduction	48
8	Heterostructures - state of the art	49
8.1	Introduction	49
8.1.1	Properties of bilayer heterostructures	49

8.1.2	Fabrication of bilayer heterostructures	51
8.1.3	Transfer -approach	51
8.1.4	Direct synthesis of vertical heterostructures	51
8.1.5	Characterization of bilayer heterostructures	52
9	Heterostructures	59
9.1	Introduction	59
9.2	Results	59
9.3	Appendix	66
10	Conclusions	76
References		76

Physical Characterization of Atomically-Thin Transition Metal Dichalcogenides

Paweł Palczyński

May 31, 2019

Declaration

Acknowledgements

Abstract

List of abbreviations

List of figures

List of tables

1 Introduction

Following the discovery and characterisation of graphene in last decade the focus has been put on other 2D materials. Similar to graphene other bulk layered materials can exist in a monolayer or few layer form. Furthermore these thin layers also exhibit a significant change of properties when number of layers decreases from bulk all the way to monolayer. One of the most popular groups of these materials are transition metal dichalcogenides (TMDC). Their general form is MX_2 where M is a transition metal, and X is a chalcogen atom.

1.1 Properties of TMDCs

TMDCs in their layered form have been known, studied and utilised for a long time. They can be found commonly in use as stolid-state lubricants or catalysts. About 60 different TMDCs have been studied and characterised with a general formula of X-M-X where a plane of metal atoms (M) is sandwiched between two chalcogen planes (X). Out of those 40 can be considered layered materials where individual layers are strongly bonded in-plane and weakly bonded out-of-plane in between layers. These weak, interlayer, Van der Waals interactions allow to form a bulk material. These bonds are also what allows for those layers to slide on top of one another similarly to other layered materials like graphite. TMDCs consist of two transition metal and single chalcogen atoms covalently bonded. They can be found in 3 distinct structural polytypes: 1T (tetragonal symmetry, octahedral coordination) with single layer per repeat unit, 2H (hexagonal symmetry, trigonal prismatic coordination) with 2 layers per repeat unit and 3R (rhombohedral symmetry, trigonal prismatic coordination) with 3 layers per repeat unit [70] as can be seen in Figure 1.

Since graphene have proven to be difficult to work with in the fields of semiconductors due to its lack of natural finite electronic band gap its role as a successor in electronic and opto-electronic devices remains to be seen. However the techniques learned and effects observed during its characterisation were easily transferred to other layered compounds such as TMDCs. In particular the semiconducting, group VI-based TMDCs, containing sulphur and selenium as chalcogen atoms have proven to be more readily potentially useful as an active material in electronic and opto-electronic devices. This is due to their inherent electronic and optical bandgap in visible-near IR range.

As the number of layers changes from bulk to monolayer the properties of the TMDC

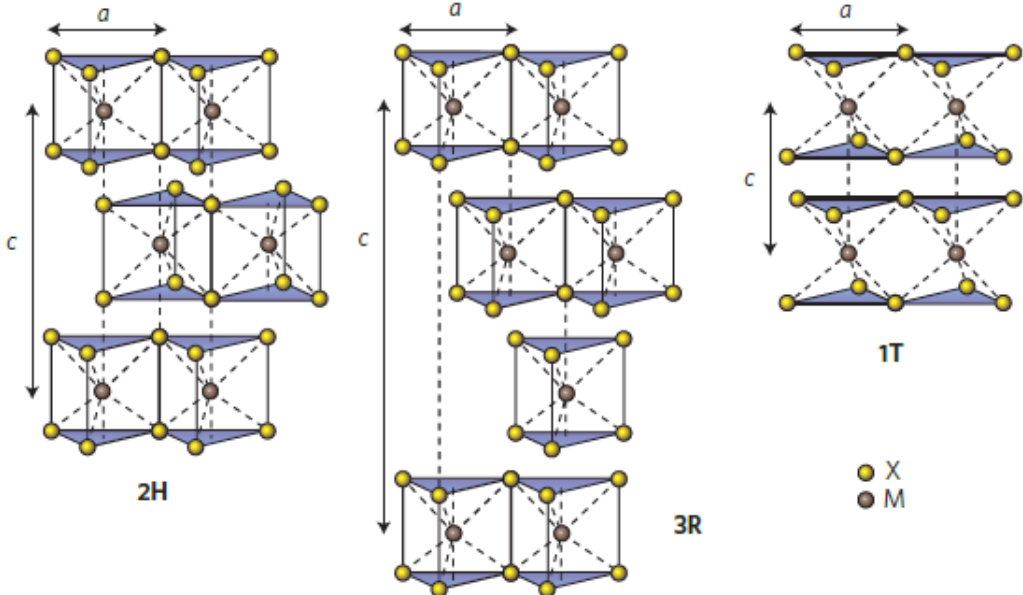


Figure 1: Schematics of the structural polytypes: 2H (hexagonal symmetry, two layers per repeat unit, trigonal prismatic coordination), 3R (rhombohedral symmetry, three layers per repeat unit, trigonal prismatic coordination) and 1T (tetragonal symmetry, one layer per repeat unit, octahedral coordination). The chalcogen atoms (X) are yellow and the metal atoms (M) are grey. The lattice constants a are in the range 3.1 to 3.7 Å for different materials. Adopted from [70]

undergo a significant change. In most TMDCs the bandgap changes from indirect to a larger direct one.

1.2 Electronic properties

One of the most interesting features that the layered TMDC materials exhibit is the shift in the bandstructure with the changing number of layers. Several studies have shown in simulations and experimentally that TMDCs have very similar electronic band structure as seen in example of WS_2 in Figure 2. In bulk WS_2 the maximum of the valence band (VBM) at Γ point and the minimum of the conduction band (CBM) at Λ form an indirect bandgap. As the number of the layers decreases the CBM at Λ point as well as VBM at K point increases causing the band gap to widen. At 2 layers the K point becomes the actual CBM and a new indirect bandgap forms between Γ point and K point. Finally in a WS_2 monolayer the VBM at K point as well as entire conduction band increases to form a new greater direct band gap at K point. This means that WS_2 bandgap changes from 1.3 eV indirect bandgap in bulk to 2.1 eV direct bandgap in monolayer.

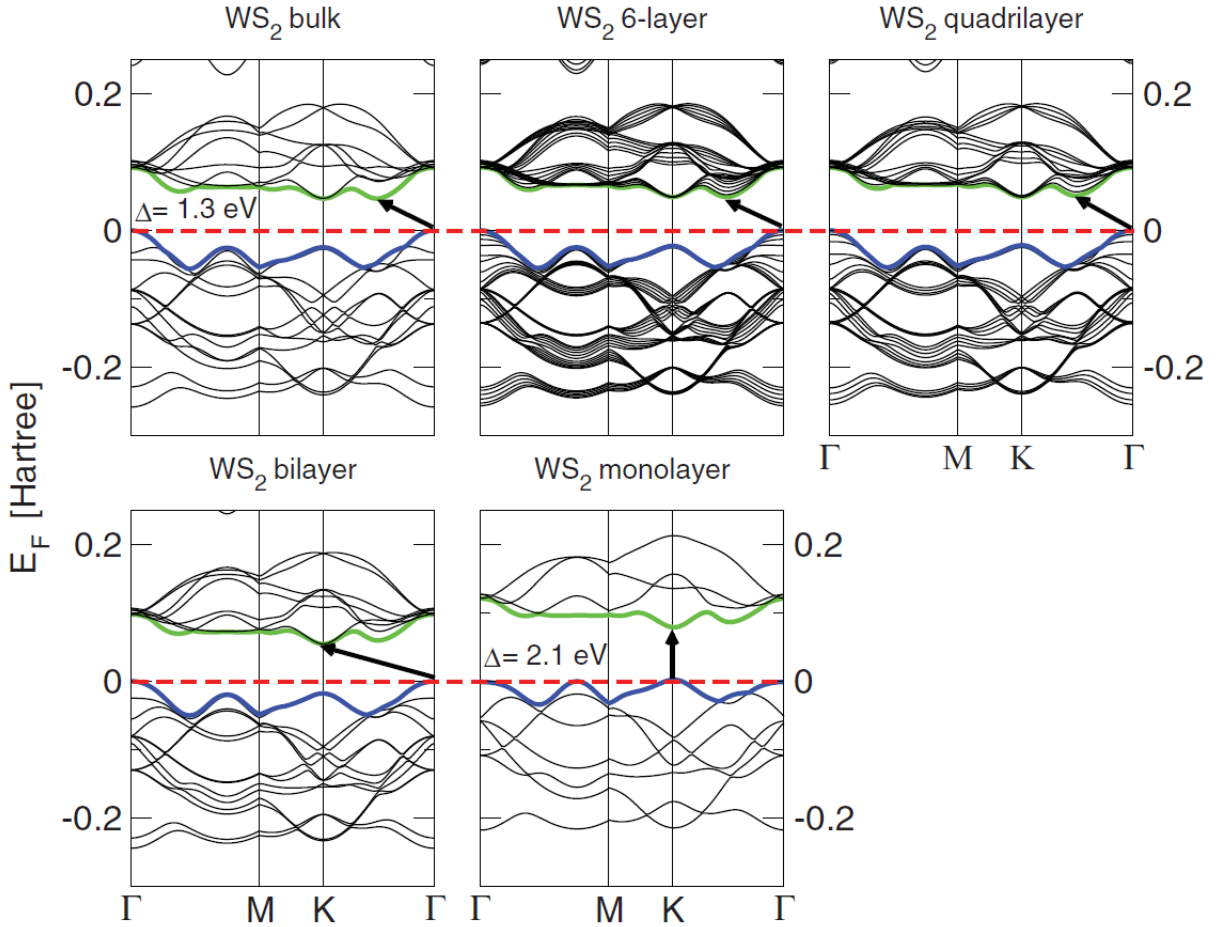


Figure 2: Band structures of bulk WS_2 , its monolayer, as well as, polylayers calculated from the density functional theory (DFT) simulation. The horizontal dashed lines indicate the Fermi level. The arrows indicate the fundamental band gap (direct or indirect) for a given system. The top of valence band (blue) and bottom of conduction band (green) are highlighted. Adopted from Ref. [34]

Like WS_2 other Mo and W based TMDC undergo similar transitions as seen in Table 1. In all cases the smaller indirect bandgap changes to greater direct bandgap with monolayer bandgap ranging from 1.1 eV to about 2.1 eV. Moreover the VBM at K points exhibits the orbit-spin band splitting at the K point of about 400 meV. This direct bandgap leads to presence of A and B excitons generated by transition between CBM and two VBMs at the K point. The conduction band as well as the valence band are dominated by the d-electron orbitals of the transition metal atoms and at the VBM and CBM they hybridize with the p-electron orbitals of the chalcogenide atoms. Because the hybridization happens mostly at the Γ point and the chalcogenide atoms are at the surface of the TMDC layer it leads to strong interactions between the layers. This leads to significant change in the

band structure at the Γ and rise of the indirect bandgap as a result of increased number of layers. On the other hand at the K point the d-orbitals of the transition metals remain mostly unaffected due to them being positioned in the middle of the layer [34] [63]

Table 1: Mo and W based TMDC bandgaps comparison

M\X	$-S_2$	$-Se_2$	$-Te_2$
Mo	Semiconducting	Semiconducting	Semiconducting
	1L: 1.8 eV	1L: 1.5 eV	1L: 1.1 eV
	Bulk: 1.2 eV	Bulk: 1.1 eV	Bulk: 1.0 eV
W	Semiconducting	Semiconducting	Semiconducting
	1L: 2.1 eV	1L: 1.7 eV	1L: 1.1 eV
	Bulk: 1.4 eV	Bulk: 1.2 eV	

1.3 Optical properties

TMDCs exhibit a wide array of opto-electronic effects due to their strong light-matter effects. These effects are mostly caused by the abundant presence of excitons, bi-excitons, trions or bound excitons. As a result the change in layer thickness from bulk to monolayer alters the photoluminescence, photoconductivity and absorption in the visible to infrared range.

The primary and most common quasi-particle that forms in such system is an exciton, which is a pair of a negatively charged electron and a positively charged hole bound together by Coulomb forces to form a structure similar to that of hydrogen atom. Such pair is electrically neutral and is of size exceeding size of single cell which makes it a Wannier–Mott exciton. The recombination of these excitons results in a photon emission which can be easily observed during photoluminescence characterisation. On top of excitons other quasi-particles such as trions, bi-excitons or bound excitons can be found. A trion is a group of 2 electrons and a hole or 2 holes and an electron, or otherwise described as a charged exciton. The exact nature of the trion depends usually on the type of intrinsic doping of the TMDC. A bi-exciton is a pair of excitons which is usually only observed in quantum dot systems but can be also seen in excitonically dense systems such as TMDCs. A bound exciton is similar to the free exciton but is trapped by a defect. In a typical photoluminescence spectrum several peaks can be observed depending on specific type of TMDC characterised. In WS_2 monolayer for instance as seen in Figure. 3 the

strongest peak (often labelled as an A peak) at about 1.97 eV is caused by the direct transition of single-photon generated exciton. Slightly redshifted by about 30 meV from the A peak a generally weaker peak caused by the trion recombination can be found. At higher energies another peak can be observed due to the presence of bi-excitons. At around the 1.3 eV a much weaker peak (I) can be seen caused by the indirect transition. Additionally a B peak can be observed blueshifted from the A peak which is caused by valley splitting as discussed in chapter 1.2. As seen in Figure 3 as the number of layers increases the main A peak becomes dramatically weaker due to lack of direct transition and redshifted following the pattern discussed in chapter 1.2. At the same time the I peak becomes relatively stronger and eventually dominates the bulk material.

Figure 3: Typical PL spectra of WS_2

Similarly the photoconductivity of the TMDCs is strongly reliant on the number of layers and incident photon energy. The MoS_2 for instance shows 3 times stronger photoconductivity in monolayer around 1.8 eV, where the direct transition is located, than in 2L MoS_2 around 1.6 eV. Additionally the photoconductivity appears to increase in steps with relation to the photon energy following the direct and indirect transitions. [70].

The sunlight absorption in TMDCs has been shown to be significantly more intense than in commonly used solar cell materials, at about 5-10% which is an order of magnitude greater compared to similar thickness of Si or GaAs. It is also stronger compared to 2-3% of sunlight absorption of graphene. As a result a excitonic solar cell based on MoS_2/WS_2 bilayer shows about 1% power efficiency, about 3 times greater than that of typical ultrathin solar cells [4].

During standard single photon excitation photoluminescence studies the excitons generated can be called "bright" since they appear in PL spectrum. The reason we can observe them easily is because the spin between an electron and a hole is conserved, and thus allowing for photon emission. However another combination is possible, called dark exciton, where both electron and the hole have the same spin. Because of that they cannot recombine by emitting a photon and therefore remain absent from the PL spectrum. Even though they exist much longer than their bright counterparts their presence is of course also more difficult to observe. One way to observe them is to use two photon excitation. Due to two photon selection rule the single photon excitation can be excluded and the dark excitonic states can be observed. In WS_2 the dark excitons result in two peaks at

2.28 eV and 2.48 eV. [Probing excitonic dark states in single-layer tungsten disulphide]

Defect engineering allows to tune the number of charge carriers. In MoS₂ or WS₂ the sulfur vacancies lead to increased number of electrons in the material. Because of that by increasing the number of defects in those materials the level of n-doping can be changed. An easy way to observe the presence of those defects and subsequent quenching of them is to expose the material to varying amounts of oxygen, nitrogen or water. Due to greater electronegativity (???) those species attract the electrons and therefore the electron population in the material decreases. This in turn leads to smaller trion population since trions require an extra electron to form. This then can be observed in PL as a more narrow direct peak, with especially smaller redshifted shoulder. The effect can also be of course reversed by decreasing the amount of oxygen, nitrogen or water in the environment since those exist in already in ambient conditions [Optical control of charged exciton states in tungsten disulfide].

In order to introduce and control the amount of vacancies in the TMDC different method have to be explored. One of the ways of achieving that in already grown material is the use of oxygen plasma. It has been shown that the number of defects can be controlled by limiting the plasma exposure. During the process the oxygen also chemically bonds to the MoS₂ at the defect sites and therefore partially negates the effect of defects on the optical properties. The PL can also be seen to increase in intensity with increasing number of defects with oxygen adsorbed due to the increased yield of bound excitons localised at these defects. [Strong Photoluminescence Enhancement of MoS₂ through Defect Engineering and Oxygen Bonding]

Similar effect has been shown using the 2,3,5,6-tetrafluoro-7,7,8,8-tetracyanoquinodimethane (F_4TCNQ), 7,7,8,8-tetracyanoquinodimethane ($TCNQ$) and (nicotinamide adenine dinucleotide) $NADH$ for chemical doping. Both F_4TCNQ and $TCNQ$ are p-type dopants while $NADH$ is a n-type dopant. By exposing the surface of MoS₂ to these compounds the change in PL intensity and FWHM have been observed. Similar to doping with O_2 , N_2 or H_2O , all of which are p-type dopants, the intensity of PL has increased in presence of F_4TCNQ and $TCNQ$. The effect has been similarly ascribed to lowering the number of defects and therefore the lowering the trion population and subsequently increasing the exciton population increasing the yield. The opposite observation has been made with use of $NADH$ with PL intensity decreasing. Similarly the increase in trion population with lower PL yield is ascribed to the lower PL intensity. [Tunable Photoluminescence of Monolayer MoS₂ via Chemical Doping].

It has also been shown that alloying can be used to fine tune the PL by varying the concentration of alloying material. In monolayer $Mo_{1-x}W_xS_2$ the PL peak position initially decreases from 1.575 eV (PL peak position of pure MoS₂) to 1.56 eV at x=0.21 and then increase up to 1.65 eV (PL peak position of WSe₂) at x = 1. This effect could be attributed to the linearity of VB and non-linearity of CB with regards to change in W composition. The PL position can therefore be engineered on a monotonic range from 1.56 eV to 1.65 eV. In bilayer $Mo_{1-x}W_xS_2$ alloy the position of both direct and indirect transition PL peaks increases monotonically from about 1.49 eV and 1.53 eV for pure MoSe₂ to 1.56 eV and 1.62 eV for pure WSe₂ as the W amount is increased. This opens another relatively easy way of engineering PL position [Two-Dimensional Molybdenum Tungsten Diselenide Alloys: Photoluminescence, Raman Scattering, and Electrical Transport].

Another effect that has been demonstrated that allows for certain degree of control of PL in TMDCs is relation between the helicity of incident light and valley population valley population. It has been shown that by exciting the monolayer MoS_2 with right-polarised light the resulting excitons will fill primarily the VB at K point. Similarly by exciting the MoS_2 with left-polarised light the excitons will fill the VB at K' point. After recombination the resulting photons will exhibit the same circular polarity as the photons that excited the electrons in the first place. [Tightly bound trions in monolayer MoS₂] [Control of valley polarization in monolayer MoS₂ by optical helicity]

The temperature effect on TMDCs has also been investigated. In WSe_2 monolayer it has been shown that as the temperature of the sample increases from room temperature to about 400K the position of the direct transition PL peak redshifts from about 1.65 eV to about 1.58 eV. When the temperature is decreased from room temperature to about 5K the same peak blueshifts to about 1.7 eV. Between 100K and 50K as well 20K and 5K the position of the PL peak does not change. Additionally around 120K another peak appears and as the temperature is lowered it also blueshifts although less than the RT peak. The peak only present at RT is attributed to free excitons whereas the peak appearing at 120K is ascribed to bound excitons. As bound exciton peak appears its intensity increases with lower temperature while the intensity of the free exiton peak decreases. This indicates that the population of free excitons decreases while the population of the bound excitons increases with decreasing temperature [66]

There has been many reports on the spatial distribution of PL in the TMDCs. One of the observed patterns in WS₂ and MoS₂ has been that of much stronger PL intensity at the edges of the flakes. That effect has been primarily observed in small flakes of about

$5 \mu m$ [20].

1.4 Phonon dispersion

The vibrational and phononic characteristics of TMDCs have been investigated at length by both theoretical simulations as well as experimental studies. The $2H - MX_2$ crystal structure of the TMDCs belongs to D_{6h}^4 point group and there are 18 lattice dynamical modes at the Γ point. Phonons belonging to these modes can be represented as Eq. 1 [71]:

$$\Gamma = A_{1g} + 2A_{2u} + B_{1u} + 2B_{2g} + E_{1g} + 2E_{1u} + E_{2u} + 2E_{2g} \quad (1)$$

In TMDCs 4 active Raman modes can be observed $E_{1g}, E_{2g}^1, E_{2g}^2, A_{1g}$. These can be seen in Figure 4. The E_{2g}^2 is a shear mode that involves 2 layers vibrating against each other. The E_{1g} is an in-plane vibration of chalcogen atoms but is forbidden in the back-scattering configuration. For monolayers therefore it leaves primarily the E_{2g}^1 which is an in-plane mode involving vibration of both metal and chalcogen atoms as well as A_{1g} which is an out-of-plane mode involving only chalcogen atoms.

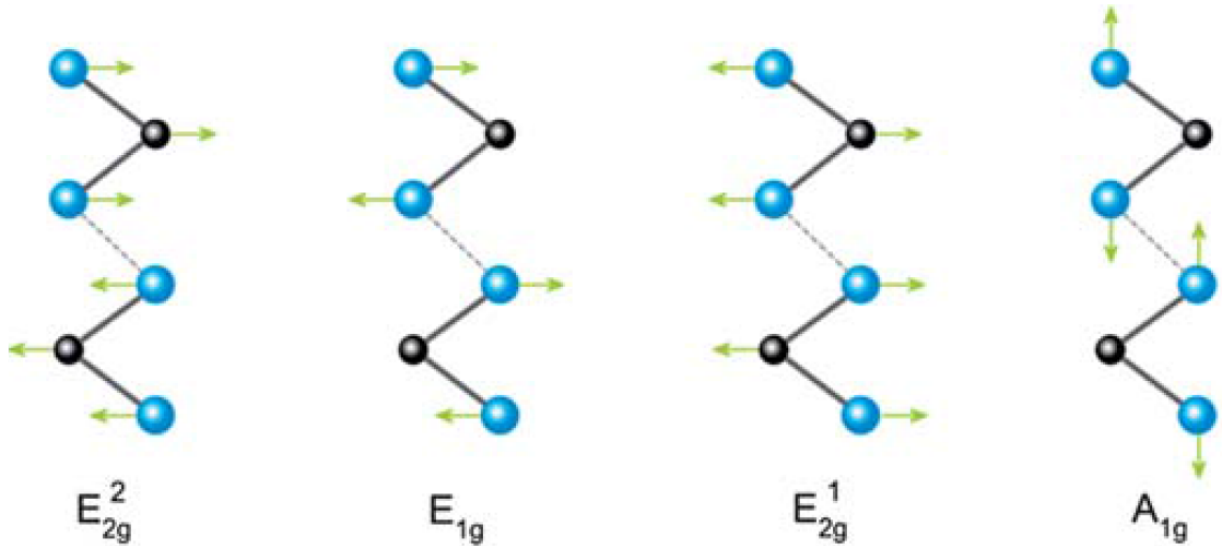


Figure 4: 4 active Raman modes in TMDCs. Metal atoms and chalcogen atoms are black and blue respectively. Adopted from [71]

These two peaks tend to dominate the spectrum of any TMDCs, whether monolayer or few-layer or bulk. The shear mode E_{2g}^2 appears at low Raman shift frequencies and is therefore difficult to observe but can be used to differentiate monolayer from few-layer

material. Since E_{2g}^1 is an in-plane mode it tends to be unaffected by the number of layers due to weak van der Waals forces between the layers but can be seen to be slightly redshifted as the number of layers increases. As seen in Figure 5 the E_{2g}^1 peak at about 352 cm^{-1} is overlapping with another stronger peak, a 2LA(M) peak at 350 cm^{-1} which is a longitudinal acoustic mode caused by in-plane collective oscillations of W and S atoms. The second strongest peak at around 416 cm^{-1} is an A_{1g} peak, caused by out of plane vibrations. Because of that it is much more sensitive to the number of layers and is seen to become blueshifted as the number of layers increases. This has been attributed to the restorative forces as well as increase in dielectric screening of the Coulomb forces. Combining both of these shifts in frequency with the changing number of layers the difference between these two peak position can be used to identify the number of layers in TMDCs as seen in Figure 6

Figure 5: Typical Raman spectrum of WS_2

Figure 6: Identification of number of layers by the difference in position of A_{1g} and E_{2g}^1 peaks.

2 Role of precursors in growth of monolayer WS_2

In this chapter the CVD growth of WS_2 using different precursors is investigated. The as grown samples were characterised by Raman and PL spectroscopy as well as XPS, XRD, AFM and electrical measurements. As a result it was concluded that using $H_2WO_4 + NaCl$ at 850 °C gives best results. Such grown samples exhibit biggest flakes up to 200 μm in size as well as show the strongest and most narrow PL peak with 36 meV FWHM. The samples grown using $H_2WO_4 + NaCl$ at 950 °C show also best transistor electron mobility in monolayer CVD grown WS_2 while that grown using $WO_3 + NaCl$ at 950 °C shows best transistor electron mobility in bilayer CVD grown WS_2 .

2.1 Introduction

Monolayers of transition metal sulphides and selenides exhibit range of interesting properties such as strong light absorption in the IR and visible range [47][4][85], valley polarisation [46] [25], spin-orbit interactions [76][86], tightly bound excitons [45] or second-harmonic generation [41]. Some of these effects can be attributed to the lack of free dangling bonds and configuration of d-orbitals [72], [39].

Among these materials one of the most promising is the WS_2 . Its visible range bandgap of 2eV as well as an easy and safe manufacturing route via CVD makes it one of the more interesting and studied TMDCs. The typical characterisation by photoluminescence spectroscopy allows to probe the varying synthesis conditions, the grain boundaries or defect population [20] [52] [38] [58]. The PL efficiency in as-grown monolayer WS_2 produced via CVD growth shows ~2-6% efficiency [52][81] [42]. This efficiency is caused mostly by defect-mediated non-radiative recombination centres [3]. LEDs have been successfully produced [31] showing external quantum efficiency up to 10% [83][73]. WS_2 is typically a n-type semiconductor due to the presence of sulphur vacancies [20][60][28]. In order to utilise this material in any potential future applications a reliable and scalable manufacturing method must be developed to ensure a high quality crystal on the wafer scale area. The main method for WS_2 synthesis that satisfies these conditions is Chemical Vapour Deposition (CVD) [21]. The growth of tungsten based TMDCs have been less successful than the equivalent molybdenum based TMDCs and has produced mostly isolated flakes of up to 40 μm [20] [84] [58] [13][77][15][37]. Even larger films of monolayer WS_2 have been shown, however they also exhibit low carrier mobility [32][16]. In the typical CVD synthesis process the sulphur and tungsten oxide are evaporated simultaneously in

a tubular furnace with a constant flow of carrier gas like argon at temperatures of at least 900 °C [20][84][58][13][77][15][37]. Such growth is predicated by topotactic transformation leading to low density distribution of domains on an amorphous [20][84][13][15][37] or crystalline substrate [58][77][49] possibly due to low evaporation rates of WO_3 . Since WO_3 requires high temperatures of 950-1000 °C to evaporate while the S becomes volatile at 90 °C the thermodynamics of the process are difficult to control. The low growth dictated by fast evaporation of S leads to limited domain growth and lack of continuous layer. One of the proposed solutions have been to spread the WO_3 on the target substrate [52][38][16][9][82][19][18]. This has however led to low reproducibility, poor control of thickness and stoichiometry and unreacted material left on the substrate. Another approach has been to use more volatile W precursors such as WCl_6 [5] or $W(CO)_6$ [32][12] together with organic compounds as S precursors. Such method while producing a large area domains at lower temperature has led to lower crystal quality and purity.

Here we propose a different method of CVD synthesis that allows for much larger flake growth of up to 800 μm at temperature of 750 degreeC. Such grown material exhibits high electron mobility in one and two layers of WS_2 , higher than other values reported in literature. The photoluminescence peak is also very narrow at 36 meV FWHM at room temperature.

2.2 Results

For the purpose of comparing the CVD synthesis method conditions the several sets of precursors were used: WO_3 , $WO_3 + NaCl$ and $H_2WO_4 + NaCl$. The standard growth procedure involves two separate crucibles placed at distance from each other in a quartz tube. Each of these crucibles is independently heated to ensure that the S and the W precursors evaporation rate is maximised at the same time. The vapours then are deposited on SiO_2/Si (285 nm) substrate which is placed close to the W precursor crucible. The entire process is performed under low vacuum and a supply of Ar gas. The furnace setup can be seen in Figure 7.

By following this method a reproducible deposition of large area flakes can be shown. As seen in Figure 8 the size of the flakes increases from left to right as the precursors used (WO_3 , $WO_3 - NaCl$ and $H_2WO_4 - NaCl$) change as well as demonstrating the lower temperature required to achieve these growths. All of these growths result in formation of triangular flakes with sharp edges and uniformity of colour throughout which suggest

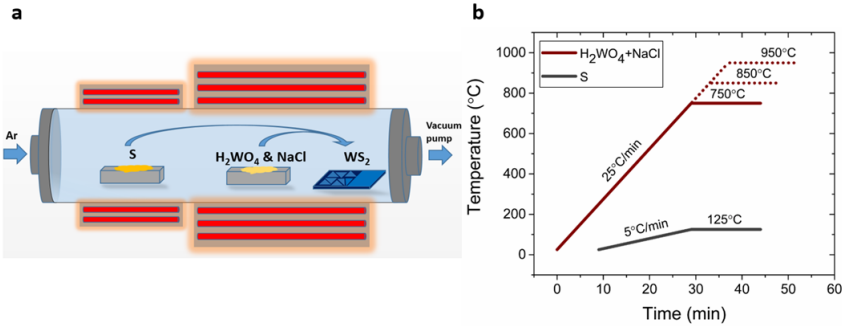


Figure 7: Illustration of: (a) CVD tubular furnace set-up; (b) temperature profile of the sulphur and the W-precursors heaters respectively. The sulphur reaches 125 °C when the metal precursors are at the maximum temperature. The SiO₂/Si wafers used as substrate for WS₂ growth are placed 1-8 cm downstream the W-precursors crucible and they are subjected to the same temperature.

a high quality, pristine material across the flake. The growth using only WO_3 results in formation of small flakes of 10 μm at 950 °C while no growth occurs at lower temperatures (Figure 8. This can be explained by the high sublimation temperature of WO_3 .

The growth can also be observed using $WO_3 + NaCl$ at 950 °C and 850 °C with the former showing flakes of size of about 60 μm while the latter showing smaller flakes of about 30 μm in size. To explain this difference in size a Robinson & Robin model can be used which states that at higher temperatures the diffusivity of the adsorbed precursors is favourable to the expansion of the existing domains. On the other hand the desorption of the adsorbed species is high leading which limits the supersaturation and formation of new domains. If the temperature is lowered even further to 750 °C then no growth is observed at all, most likely due to slow evaporation of WO_3 precursor.

With the change of precursors from WO_3 to H_2WO_4 a signifacnt change in size of flakes is observed at 850 °C and higher temperatures with lengths exceeding 200 μm . Additionally the growth have been shown to occur at 750 °C with flakes of the size of 50-200 μm . Moreover continuous monolayer areas of up to 0.8 mm in size has been shown (Figure ??). By increasing the growth pressure (1.6 mbar to 13 mbar) at 950 °C bilayer WS_2 flakes can be preferentially formed (Figure ??).

Original paper starts here. To be replaced or rewritten

By replacing WO_3 with H_2WO_4 the lateral size of the WS_2 monolayered domains significantly increases (Figure 1g,h,i). The triangular crystals have edge lengths exceeding 200 μm at temperatures higher than 850 °C and between 50-200 μm at 750 °C (Fig-

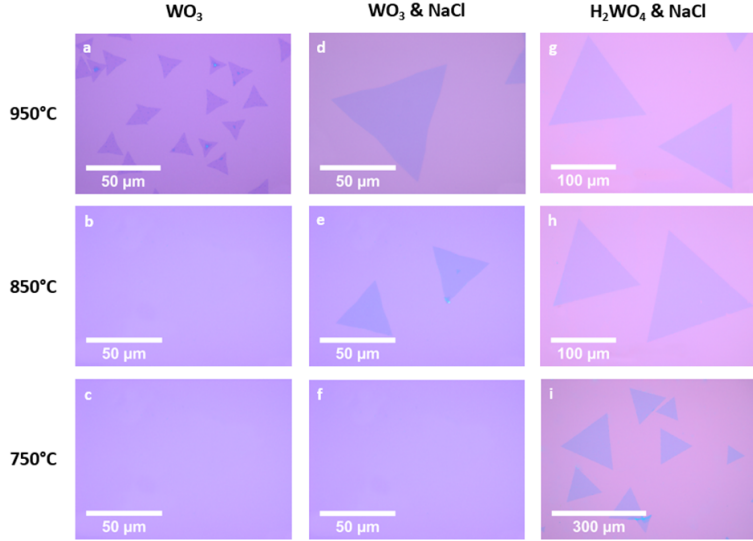


Figure 8: Optical micrographs of WS_2 triangles grown on SiO_2/Si substrates at different temperatures and using different precursors: (a) WO_3 at 950 °C; (b) WO_3 at 850 °C; (c) WO_3 at 750 °C; (d) $WO_3 + NaCl$ at 950 °C; (e) $WO_3 + NaCl$ at 850 °C; (f) $WO_3 + NaCl$ at 750 °C, the OM appears as a bare SiO_2 substrate; (g) $H_2WO_4 + NaCl$ at 950 °C; (h) $H_2WO_4 + NaCl$ at 850 °C; (i) $H_2WO_4 + NaCl$ at 750 °C.

ure 1g,h,i). Continuous polycrystalline monolayer coverage has been obtained over areas of ~ 0.8 mm extension (Figure S2). Increasing the growth pressure (from 1.6 mbar to 13 mbar) at 950 °C bilayered WS_2 flakes are preferentially formed (Figure S3). To understand the facilitated synthesis of WS_2 using H_2WO_4 and $NaCl$, we conducted X-ray diffraction (XRD) analysis of the reaction products between $H_2WO_4 + NaCl$ and $WO_3 + NaCl$ systems at different temperatures (500 °C, 650 °C and 750 °C) to understand the chemical differences (Figure S4). We found that the main products of the reactions between $NaCl$ and H_2WO_4 are: $NaxWyOz$ and tungsten oxychloride ($WClO_4$ and WO_2Cl_2). The $NaxWyOz$ possesses a high evaporation temperature as it remains in the crucible (Figure S5) after the synthesis of WS_2 is completed. Further, using this compound as precursors for a new growth of WS_2 at 950 °C did not lead to the formation of any WS_2 flakes, confirming the high evaporation temperature. On the bases of previous studies on the synthesis of bulk crystals, the formation of tungsten oxychloride species (WO_2Cl_2 and/or $WOCl_4$) is likely to occur while the formation of metal halides is less favourable (e.g. WCl_6) [][]. Tungsten oxychlorides are volatile already at 200 °C [] and they can be sulfidized in vapour phase and then be deposited onto the target substrate as atomic clusters. $WOCl_4$ has been previously used [43] as precursor for the CVD synthesis of WS_2 bulk films. De-

spite its strong tungsten oxygen double bonds, WOCl₄ proved to be an effective precursor with a clean decomposition pathway in the CVD process without formation of tungsten oxysulfide. We have verified that using this precursor is indeed possible to obtain WS₂ at temperatures as low as 550 °C (Figure S6a). The key role played by the oxyhalide species it becomes apparent if we try to grow WS₂ by using only hydrated tungsten oxide. As this decomposes to form WO₃, only small WS₂ domains are observed with similar PL characteristics to the WO₃ precursors-growth (Figure S6b). Furthermore, to confirm the key role played by Cl, we replaced NaCl with KCl and we obtained comparable growth results (Figure S6c).

End of paper

Incorporate XRD

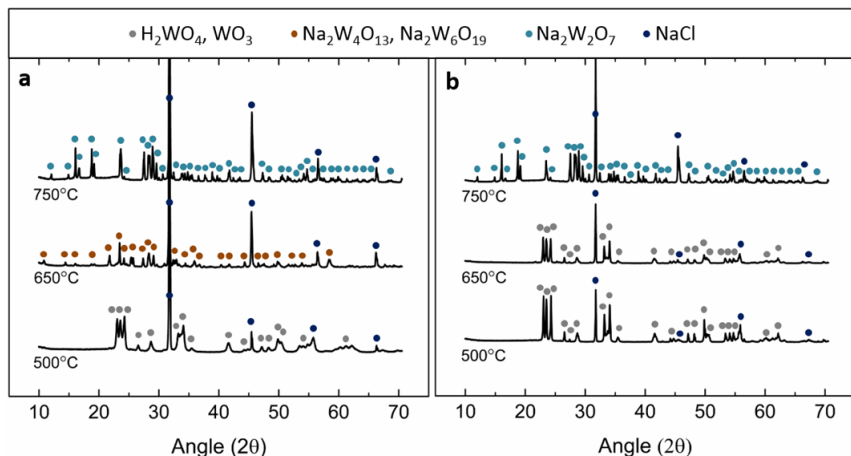


Figure 9: XRD pattern of the residual powder of W-precursors after thermal treatment at 500 °C, 650 °C and 750 °C respectivley, using (a) $\text{H}_2\text{WO}_4+\text{NaCl}$ and (b) WO_3+NaCl as precursor.

The flakes were investigated using HRTEM to confirm high crystallinity of the material (Figure 11. The lattice constant measured in this way has been found to be 0.3 nm, which is consistent with that of 2H-WS₂ (0.318 nm). The AFM characterisation allowed to confirm the presence of monolayer (Figure 11) and bilayer (Figure ?? flakes with the step of 0.8 nm [75][55].

The Raman spectroscopy characterisation of WS₂ flakes obtained under different growth conditions can be seen in Figure 11. All of these spectra exhibit the main 2 peaks at $\sim(351\pm0.53)$ cm^{-1} and $\sim(417.6\pm1)$ cm^{-1} . The latter peak corresponds to the A_{1g} vibrational mode while the former peak can be further resolved into two peaks, one related to 2LA vibrational mode and the second to E_{2g}^1 . As seen in the Figure 14a and

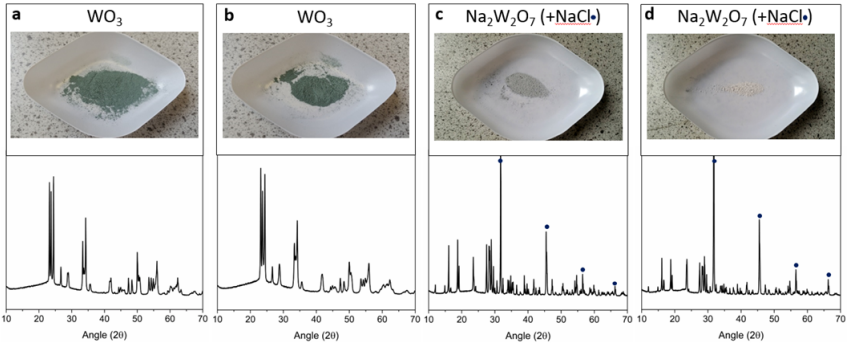


Figure 10: Residual powders of the W-precursors and their XRD patterns after thermal treatment at 750°C using (a) WO_3 , (b) H_2WO_4 , (c) WO_3+NaCl , and (d) H_2WO_4+NaCl as precursor. The blue dots in the XRD patterns indicate the presence of residual $NaCl$.

Figure 14c the distribution of intensity of both main peaks is uniform across the flakes. Similarly the difference between peak positions of A_{1g} and E_{2g}^1 is also uniformly distributed as seen in Figure 15 and is equal to $\sim(66.5\pm0.53)$ cm^{-1} which is indicative of monolayer [74].

As seen in Figure 12 maps of PL intensity has been collected for samples grown using different growth condition. The sample grown using WO_3 at 950 °C appears to be trisected into 3 symmetrical areas. The intensity is lowest along the the trisecting lines and highest in the centre of each of the sub-triangles. The PL peak position is inversely proportional to the intensity of the PL peak as seen in Figure 16a. The distribution of the PL peak positions seems to be bimodal with maxima at 1.96 eV and 1.94 eV. The FWHM is distributed mostly uniformly with few small areas of greater and few of smaller FWHM (Figure 16b with the average value of 65 meV. These peak position and FWHM values are comparable with those reported in literature [20][58][23][33]. The PL spectra taken from one of the three smaller parts of the flake are redshifted by about 0.02 eV and are wider than average. This can be explained by the presence of defects, in particular sulfur vacancies, which effectively cause the WS_2 to be n-doped [26][53]. This in turn increases the trion population which introduces new peak, redshifted by about 30 meV, which results in overall shift and broadening of the PL peak [67][20]. Additionally such localised changes in PL peak intensity and position can be caused by local strain [44][26]. To investigate the potential effect of strain on the observed PL pattern a flake was cut using high power 532nm laser. As seen in Figure 17 the resulting pattern remains the same as before treatment. Therefore the observed pattern is most likely caused by the local variation in defect density [43].

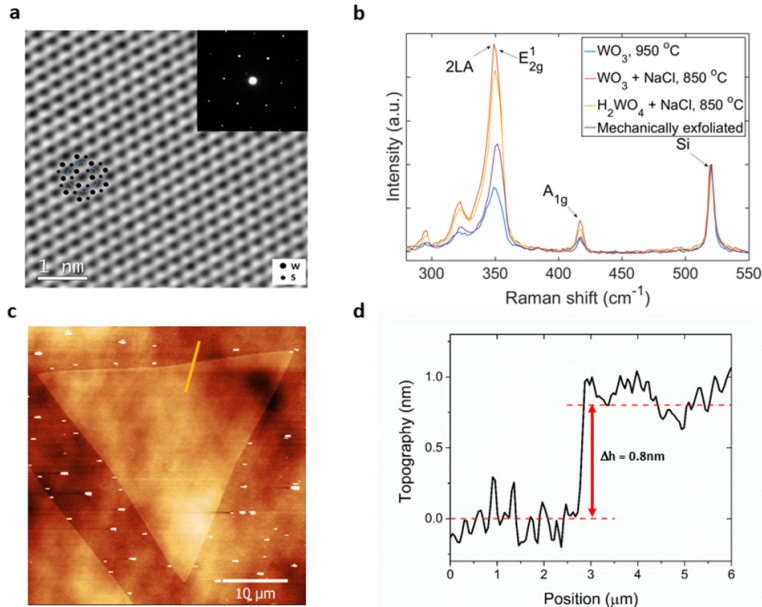


Figure 11: Structural and physical characterization of WS_2 triangles: (a) HRTEM image of the WS_2 lattice grown using $H_2WO_4 + NaCl$, the inset report a selected diffraction area which show a hexagonal pattern. (b) Raman spectra showing the characteristics active modes of WS_2 grown under different conditions and compared with mechanically exfoliated flakes. (c) AFM image and (d) corresponding thickness profile of monolayer WS_2 .

By introducing the $NaCl$ and mixing it with WO_3 precursor WS_2 samples are grown that exhibit higher energy and narrower PL peaks. The spectra are asymmetric and can be therefore deconvoluted to obtain an exciton and trion component (Figure 13). The spatial distribution of the PL position and width is mostly uniform throughout the flake. However the distribution of PL peak positions and FWHM across different flakes grown at the same conditions is bimodal (Figure 13). The PL peak position is found to be ($\sim 1.95 \pm 0.002$ eV and 1.96 ± 0.002 eV) while the FWHM is ($\sim 43 \pm 2.8$ meV and 51 ± 3 meV) which is smaller than most reported works [20][58][23][33]. This can be explained by smaller trion component in the PL spectrum which in turn means that WS_2 samples grown at these conditions contain less structural defects compared to the pure WO_3 growth. A difference in growth mechanism (topotactic or molecular conversion) which results in different defect distribution can be attributed to the differences in samples.

By changing the WO_3 precursor to the H_2WO_4 precursor a further shift in PL peak position, as well as increase in PL intensity and narrowing of he PL peak is observed as seen in Figure 12, 13. The PL peak position distribution across the flake is narrow and

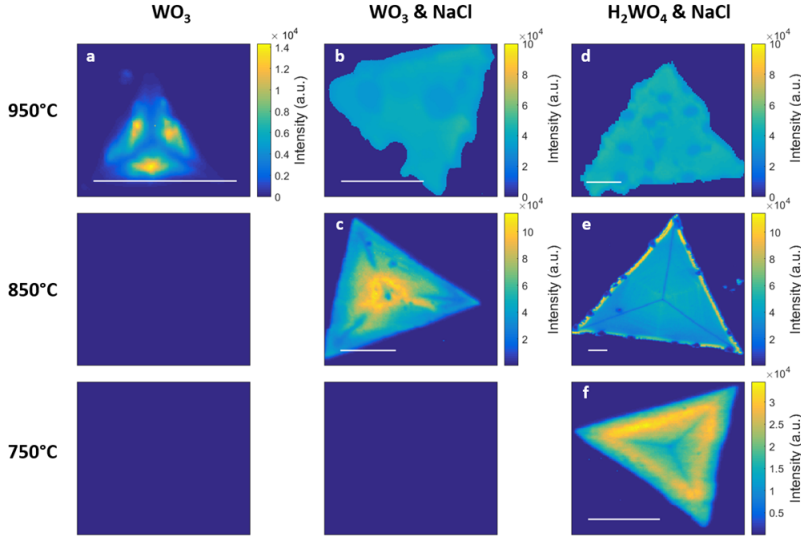


Figure 12: Spatial maps of PL intensity of WS_2 grown in the conditions exemplified in Figure 1. The scale bar length is $10\mu m$.

is ($\sim 1.980 \pm 0.005$ eV) which is higher than that of the WO_3 and $WO_3 + NaCl$ systems. The FWHM is found to be ($\sim 36 \pm 3$ meV) which is also smaller than that of the WO_3 and $WO_3 + NaCl$ systems. The PL peak width is also smaller than that reported in literature for CVD grown [20][58][23][33] exfoliated WS_2 [85][60]. At the same time it is comparable to the WS_2 grown on van der Waals substrates [49] as well as mechanically exfoliated WS_2 [31]. Additionally the peak position as well as FWHM variation is also smaller than that of other samples (5meV and 3meV respectively) (Figure 18d. The PL peak intensity map (Figure 12) shows that the spatial distribution of intensity is also much more homogeneous with faint weak pattern of three trisecting lines still visible.

Incorporate PL maps and scatter plots

As seen in Figure 14 the Raman peaks are generally uniform in both intensity and position for most samples. The irregularities in the intensity and position of both the E_{2g}^1 and A_{1g} in the sample grown at 950 °C with both $WO_3 + NaCl$ and $H_2WO_4 + NaCl$ are caused primarily by residue deposited on top of the flakes after the growth as seen in optical micrographs. Additionally as seen in Figure 14a the deviations from the mean value are located primarily at the edges of the sample. This suggests that the rest of flake is pristine and the deviations are associated with residue located at the edges. The coefficient of variation (CV) for the intensity and position for the samples grown at 950 °C with WO_3 and at 850 °C with $WO_3 + NaCl$ and $H_2WO_4 + NaCl$ is on the order of up to 10^{-4} which indicates a very high homogeneity across the samples. This further shows

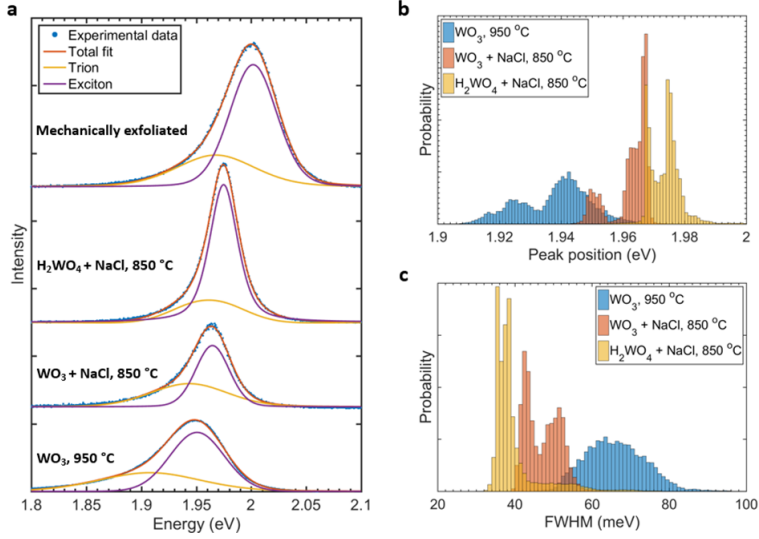


Figure 13: PL spectra characteristics of WS₂ grown using: WO₃ at 950 °C, WO₃+NaCl at 850 °C, H₂WO₄+NaCl at 850 °C: (a) individual spectra (dotted line) and deconvolution in exciton and trion components; (b) distribution of PL peak position and (c) distribution of PL FWHM for several WS₂ grown using the three different precursor systems.

that the crystal quality of the flakes is quite uniform regardless of the growth method.

By looking at the difference in position between A_{1g} and E_{2g}^1 peak positions as seen in Figure 15 it can be further concluded that the flakes are uniformly monolayer. The deviations from the mean are heavily localised and correlated with differences in PL as well as optical images and are most likely caused by precursors residue. Additionally no trisecting lines (as seen in Figure 12) can be seen in the maps of Raman spectra.

The maps of PL peak positions and widths can be seen in Figure 16. The PL positions map of the sample grown at 950 °C using WO_3 shows some variability with spots of lower energy that loosely correlate with the PL intensity. There is still faintly visible pattern of three trisecting lines of higher energy as seen in Figure 12. This indicates the areas with higher intensity correlate with lower peak position, especially along the trisecting lines. The other maps, especially the ones grown at 850 °C and 750 °C with $WO_3 + NaCl$ and $H_2WO_4 + NaCl$, are more uniform in terms of PL peak position and PL peak width. The deviations are again highly localised and correlated with the deviations in Raman and PL intensity. These deviations are generally of lower PL peak position as well as greater PL peak width which generally indicates lower crystal quality.

One possible explanation of the pattern of trisecting lines as seen in e.g. Figure 12 is the thermal strain caused by difference in thermal expansion coefficient between WS₂ and

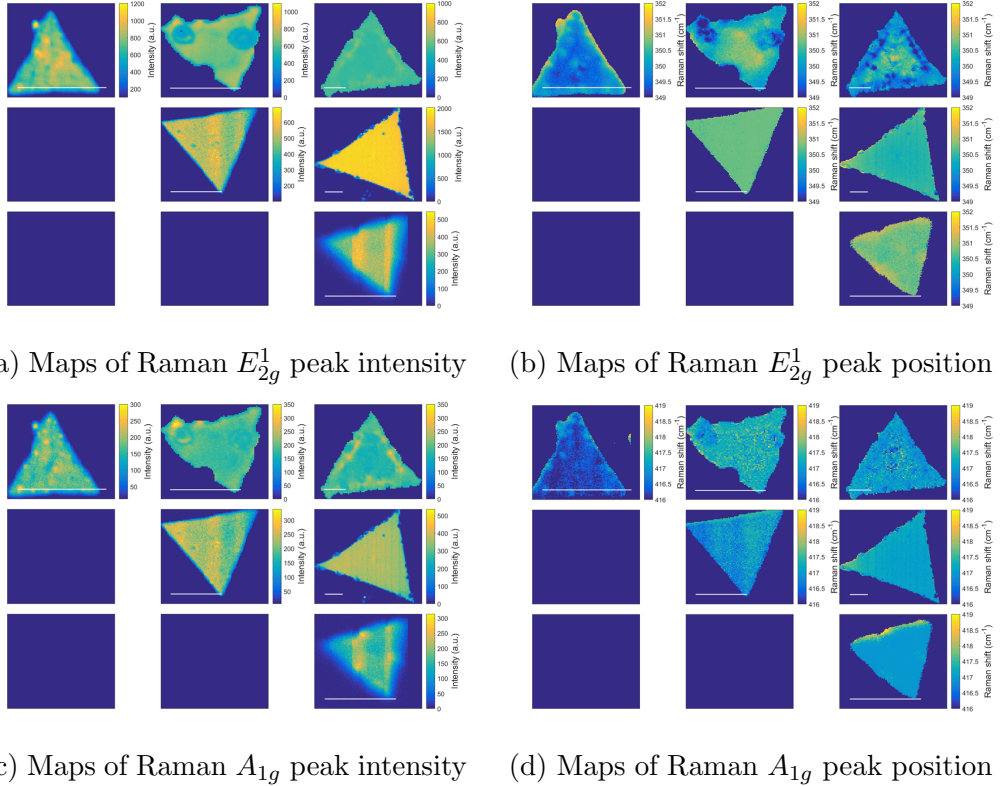


Figure 14: Maps of Raman peaks intensities and positions

the SiO_2 substrate. Since it is known that the strain in TMDCs including WS_2 can cause the change in Raman and PL spectrum [44][26] then removing a piece of the material should cause the strain to adapt to new bounding conditions. In order to investigate the trisecting pattern a flake with such pattern has been cut using 532 nm high intensity laser (50 mW). As seen in Figure 17 both the PL intensity maps and Raman E_{2g}^1 maps show a clear separation. The resulting PL and Raman intensity maps however do not show any significant change in the pattern. The trisecting lines as well as local maxima can still be seen in PL intensity map. The Raman shows few spots of increased intensity on the halves of the flake as well as a very weak increased intensity area along the cut. Since there is no observed increased intensity along any edges before cutting the flake it does not appear that the increased intensity along the cut is a result of strain being resolved into new bounding conditions. It appears therefore that cutting the material did not alter the pattern nor alter the rest of the PL or Raman spectra maps.

The spectral maps from different flakes grown with the same conditions were then collected and plotted as graphs of intensity or width versus position. As seen in Figure 18d the PL intensity seems to be largely independent of the PL position. If PL is present at given position then intensity is mostly uniformly distributed in terms of intensity. The

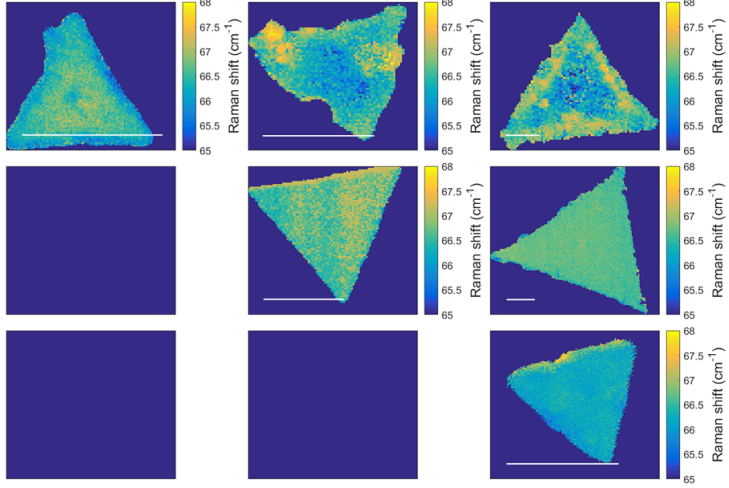
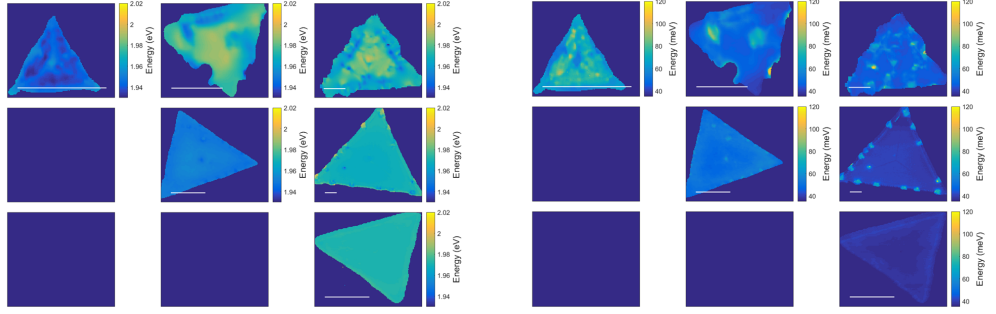


Figure 15: Raman spectroscopy: $2LA - A_{1g}$ energy differences. Scale bar is $10 \mu\text{m}$



(a) Maps of PL peak position

(b) Maps of PL peak width

Figure 16: Maps of PL peak positions and width

PL width seems to be inversely related with regards to PL position. In samples grown at 850°C with $WO_3 + NaCl$ the relation seems to be the strongest. Across all the samples the values vary between around 60-80 meV at low PL energies (1.92 eV) to 40-60 meV at high PL energies (1.98 eV). This seems to be related to overall quality of the crystals, i.e. the presence of defects, stoichiometry, crystallinity, doping, adatoms. The more uniform the sample the less mechanisms for peak broadening as well as fewer added energy levels facilitating different electron recombination paths.

The chemical composition of the flakes grown using $H_2WO_4 + NaCl$ has been investigated using XPS. The W 4f $5/2$ and W 4f $7/2$ core levels show peak positions that of the W^{4+} in WS_2 [6][48] (32.7 eV 34.8 eV respectively) with FWHM of 1 eV (Figure 19, the smallest possible using Mg K α x-ray source. It means therefore that the WS_2 is of perfect stoichiometric ratio of W and S. Additionally by integrating the intensity of the

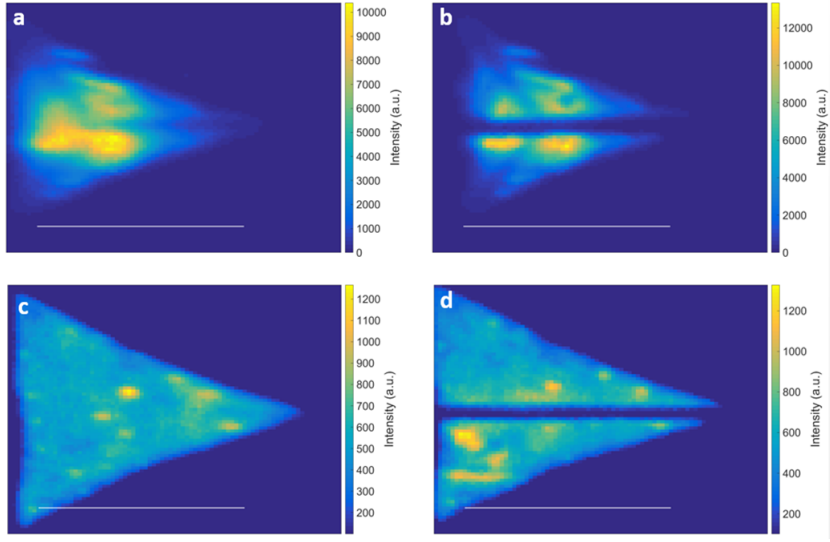
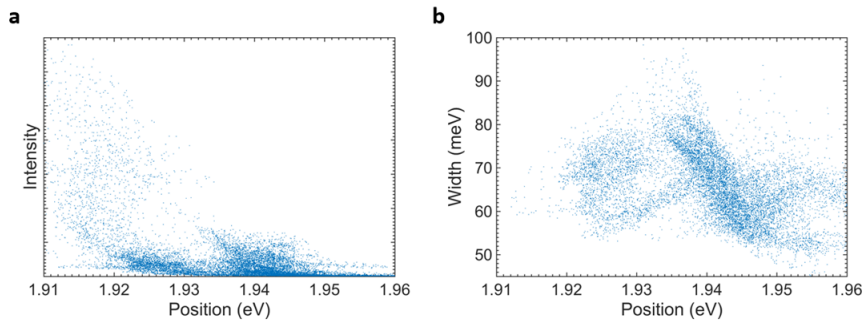


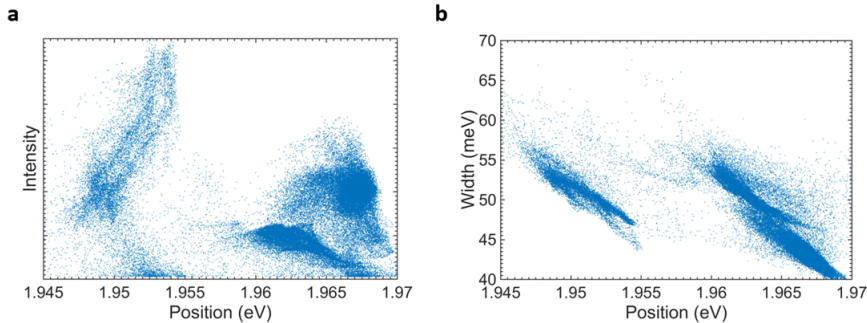
Figure 17: PL intensity (a) before and (b) after the cutting. $2LA + E_{2g}^1$ Raman intensity (c) before and (d) after the cutting. Scale bar is $10 \mu\text{m}$

$\text{W} 4\text{f}$ and $\text{S} 2\text{p}$ core level peaks the same result is achieved. Furthermore the $\text{S} 2\text{p}1/2$ and $2\text{p}3/2$ core levels are also present at the expected position for WS_2 (162.3 eV and 163.4 eV respectively, Figure 19) and small FWHM of 1 eV [48]. Small peaks indicative of W^{6+} ($\text{W} 4\text{f}5/2$ and $\text{W} 4\text{f}7/2$ at 35.9 eV and 38.1 eV respectively, Figure 19) can be attributed to presence of WO_3 and which partially overlaps with $\text{W} 5\text{p}$ core level (38.5 eV). These peaks however disappear after the flakes are transferred to another Si/SiO_2 substrate, suggesting that they can be caused by residue WO_3 given that the XPS spot size is relatively big ($\sim 1 \text{ mm}$). The FWHM of the $\text{W} 4\text{f}$ core levels was unchanged after the transfer, indicating that the crystallinity and the quality of the flakes was preserved with no extra defects introduced.

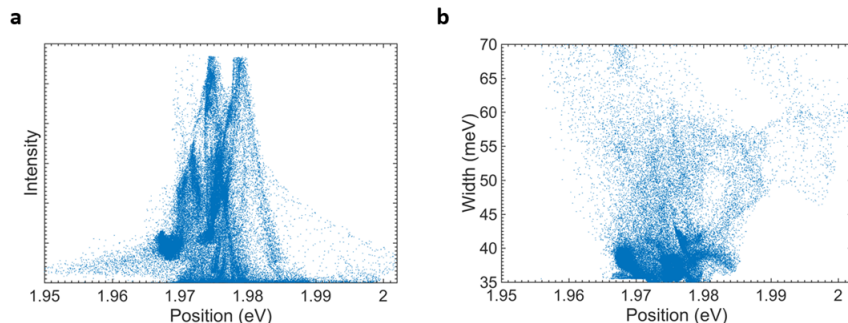
The WS_2 samples grown using $WO_3 + NaCl$ have been characterised by XPS as well and the stoichiometric ratio of 2:1 for S:W has been found. However the W^{6+} component, caused most likely by presence of WO_3 ($\text{W} 4\text{f}5/2$ and $\text{W} 4\text{f}7/2$ at 35.9 eV and 38.1 eV respectively) is more pronounced indicating incomplete sulfurisation. Similarly to the sample grown with $H_2WO_4 + NaCl$ this component disappears entirely upon transferring the sample onto new Si/SiO_2 indicating it is present around the flakes, distributed across the substrate. The W^{4+} 4f core levels peak width is $\sim 1.2 \text{ eV}$ which indicates higher defect concentration compared to that of the sample grown using $H_2WO_4 + NaCl$. This FWHM however increases after the transfer, which is most likely caused by the increase in the concentration of the defects caused by the mechanical stress during the transfer.



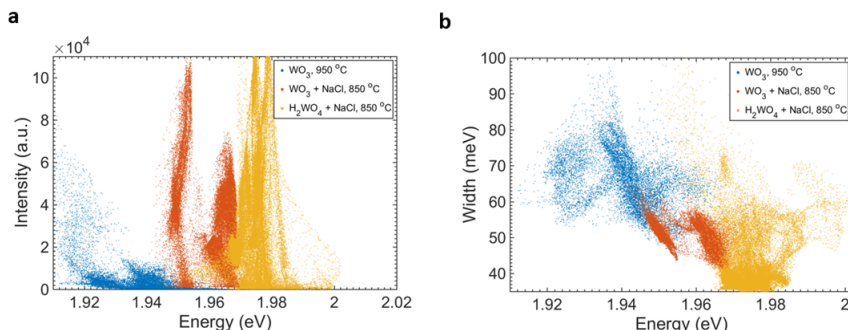
(a) (a) PL Intensity vs position, (b) PL FWHM vs position of WS_2 grown using WO_3 at 950 °C



(b) PL Intensity vs position, (b) PL FWHM vs position of WS_2 grown using $WO_3 + NaCl$ at 850 °C



(c) (a) PL Intensity vs position, (b) PL FWHM vs position of WS_2 grown using $H_2WO_4 + NaCl$ at 850 °C



(d) (a) PL Intensity vs position, (b) PL FWHM vs position of WS_2 grown using WO_3 , $WO_3 + NaCl$, $H_2WO_4 + NaCl$

In conclusion the H_2WO_4 is shown to be a better precursor compared to WO_3 .

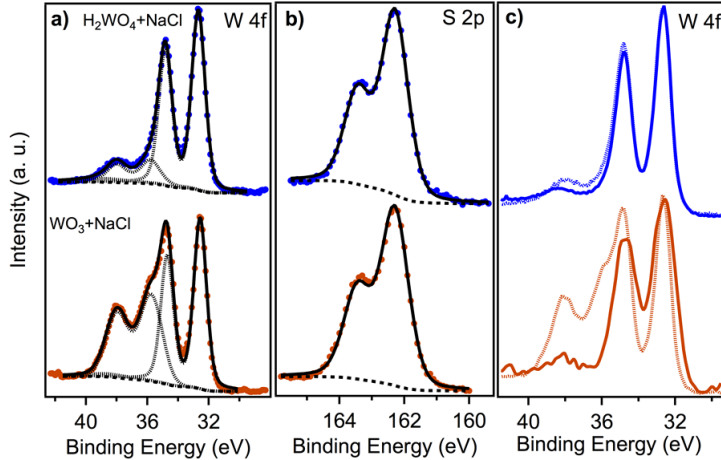


Figure 19: XPS spectra of the W 4f and S 2p core level peak regions. (a) Comparison of W 4f_{5/2}, W 4f_{7/2} and W 5p core levels of WS₂ grown using $H_2WO_4 + NaCl$ at 950 °C (blue spectrum) with WS₂ grown using $WO_3 + NaCl$ at 950 °C (red spectrum). The deconvolution of W 4f_{5/2}, W 4f_{7/2} and W 5p core levels and overall fit of the spectrum are reported as black dashed and a continuous line respectively. (b) The S 2p_{1/2} and 2p_{3/2} core levels for each of the two growth conditions are reported in the central panel. (c) W 4f_{5/2}, W 4f_{7/2} and W 5p core levels before (dashed line) and after transfer (continuous like) onto a new SiO₂/Si substrate are compared showing the complete disappearance of the residual WO_3 components. The spectra were fit by Doniach-Sunjic function after subtracting a Shirley background (black dashed line).

The samples were further characterised for their electrical properties. Bottom-gated field effect transistors were prepared as seen in Figure 20. The FET transfer curve indicates accumulation-type n-channel transistor, where the drain current increases with applied gate bias after a threshold is crossed. Once the current-bias curve reaches linear range it can be described by $I_d = \mu_n C_{ox} (W/L)((V_{gs} - V_{th})V_{ds})$, where μ_n is the electron field-effect mobility, C_{ox} is the oxide dielectric and V_{th} is the threshold voltage. As seen in Figure 20 a typical response curve for both the as grown as well as transferred samples of WS₂ grown with H_2WO_4 show an asymmetry around $V_{ds} = 0$ V due to difference in the source and drain potentials. The Schottky barrier at the source is pinned by the gate, while the barrier at the drain diminishes proportionally to the drain bias and vice versa. The contacts however become more "Ohmic", when the bands bend more at the semiconductor/metal interface while the gate bias increase, leading to more significant

tunnelling current.

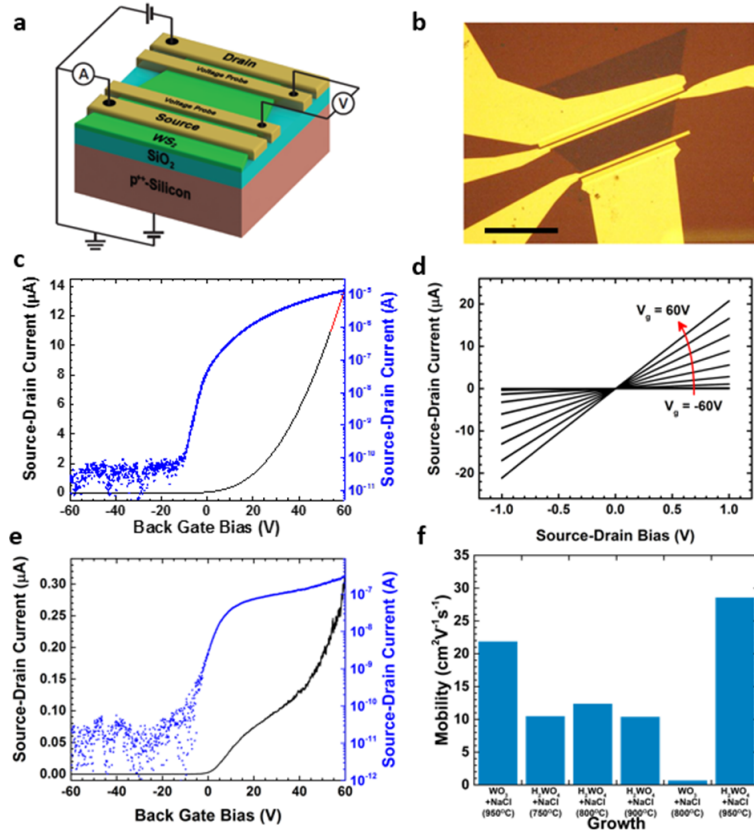


Figure 20: Electrical characteristics of monolayer WS_2 : (a) Schematic of the bottom-gated field effect transistors; (b) optical micrograph of the device (scale bar is $20\mu m$); (c) FET transfer curve for the monolayer WS_2 grown using H_2WO_4+NaCl at $950\text{ }^\circ C$ showing the highest mobility of $28\text{ }cm^2/Vs$ (linear region of the transport graph marked with a red-dashed line); (d) Response curves at different gate biases for a WS_2 triangle grown using H_2WO_4+NaCl ; (e) FET transfer curve for the monolayer WS_2 grown using WO_3+NaCl at $800\text{ }^\circ C$; (f) electron mobilities of monolayer WS_2 grown using different conditions.

By looking at the linear regime of the transport graph (red-dashed line in Figure 20) the field-effect mobility can be calculated as $\mu_n = C_{ox}^{-1}(d\sigma/dV_{gs})$. The electron mobility calculated for WS_2 grown with H_2WO_4+NaCl is generally higher than that of WS_2 grown with $WO_3 + NaCl$ (Figure 20) which further indicates higher crystal quality when using H_2WO_4 . The monolayer WS_2 exhibits electron mobility of $28\text{ }cm^2V^{-1}s^{-1}$, the highest reported value for CVD grown WS_2 and transferred onto SiO_2 [38][32][16][84][77][37][82][2][36][27][10] and comparable to mechanically exfoliated WS_2 [74][29][17][30]. The highest mobilities were recorded in WS_2 grown at $950\text{ }^\circ C$, grown with either H_2WO_4+NaCl or WO_3+NaCl ,

which indicates a role of the growth temperature in improving the quality of the WS_2 . As the temperature is lowered the difference between precursors becomes more pronounced in terms of the crystal quality. The $H_2WO_4 + NaCl$ precursor system grown WS_2 shows electron mobility of 10 to 20 $cm^2V^{-1}s^{-1}$ at temperatures of 750 °C and 850 °C. The electron mobilities of WS_2 grown using $WO_3 + NaCl$ are much lower, $\sim 2 cm^2V^{-1}s^{-1}$ at 800 °C. Bilayer WS_2 samples have overall greater electron mobility than their monolayer equivalent (between $\sim 38 cm^2V^{-1}s^{-1}$ and $52 cm^2V^{-1}s^{-1}$), similarly to the mechanically exfoliated flakes [50][30]. The electron mobility of bilayer WS_2 ($52 cm^2V^{-1}s^{-1}$) (Figure 22 and Figure 21) is also higher than that of other CVD grown WS_2 as well as mechanically exfoliated onto SiO_2 samples of WS_2 reported [28][50][30]. The highest mobility has been obtained for bilayer system using $WO_3 + NaCl$ indicating that the precursor choice is less important for electron mobility in such systems.

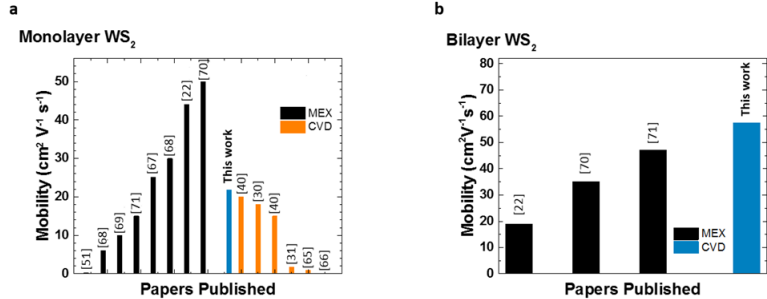


Figure 21: Comparison of our results with the literature of CVD grown material and mechanically exfoliated WS_2 (MEX) : electron mobility for (a) monolayer WS_2 and (b) bilayer WS_2 . The histograms show our record values for both monolayer and bilayer amongst the best values reported for CVD grown WS_2 .

2.3 Conclusions

In conclusion a synthesis route has been developed that allows for high quality monolayer and bilayer WS_2 CVD growth. This quality is demonstrated by highest recorded electron FET mobility for both monolayer and bilayer CVD grown WS_2 compared to the literature and comparable to that of mechanically exfoliated ones. Additionally the triangle flakes grown using $H_2WO_4 + NaCl$ are much larger (up to $\sim 200\text{--}300 \mu m$) compared to ones grown using standard WO_3 . The CVD growth using H_2WO_4 has also been demonstrated to work at lower temperatures, down to 750 °C compared to more commonly used 950 °C. Finally the PL of the WS_2 grown using H_2WO_4 is uniform throughout the flake and

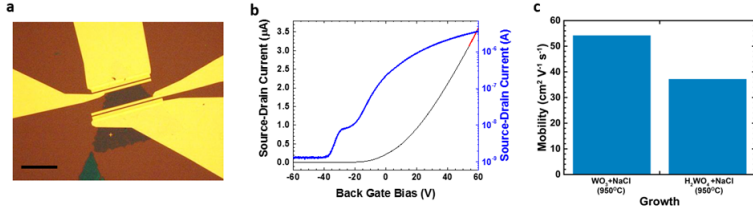


Figure 22: Electrical characteristics of bilayer WS₂: (a) Optical micrograph of the device (scale bar is 30μm); (b) FET transfer curve for the bilayer WS₂ grown using WO₃+NaCl at 950 °C showing the highest mobility of 52 cm²/Vs (linear region of the transport graph marked with a red-dashed line); (c) electron mobility of bilayer WS₂ grown by using different precursor systems.

has very FWHM (36 meV) which again points to high crystal quality and lack of defects in form of sulfur vacancies. These findings allow to develop further the TMDCs synthesis method of CVD and can potentially lead to industrially scalable synthesis of monolayer *WS*₂ or other TMDCs over large area.

3 WSe₂

3.1 Introduction

WSe₂ is a TMDC material very similar to the *WS₂*. The main difference is its bandgap which for monolayer is about 1.65 eV. This allows for potential application in the near infrared range. Its crystal structure is the same as the other TDMCs as outlined in 1.4. The electronic structure can be seen in Figure 23 and it is very similar to that of the *WS₂*.

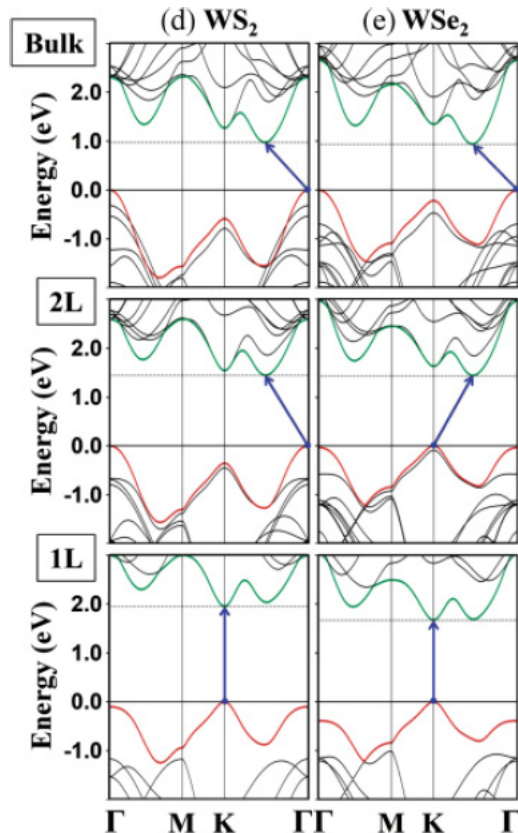
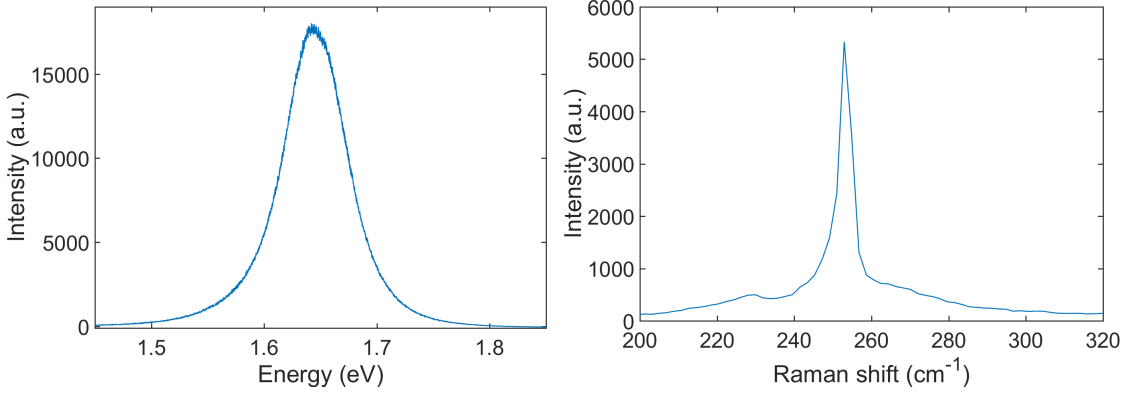


Figure 23: *WS₂* and *WSe₂* electronic band structure for 1, 2 and many layers (bulk)

3.2 Results

A typical PL and Raman spectrum can be seen in Figure 24. The PL peak is mostly symmetrical with little to no trion component as seen in *WS₂* flakes. The peak is centred at around 1.645 eV with FWHM of 66 meV. The Raman peak around 250 cm^{-1} is a convolution of 2 peaks, a E_{2g}^1 and A_{1g} peaks.

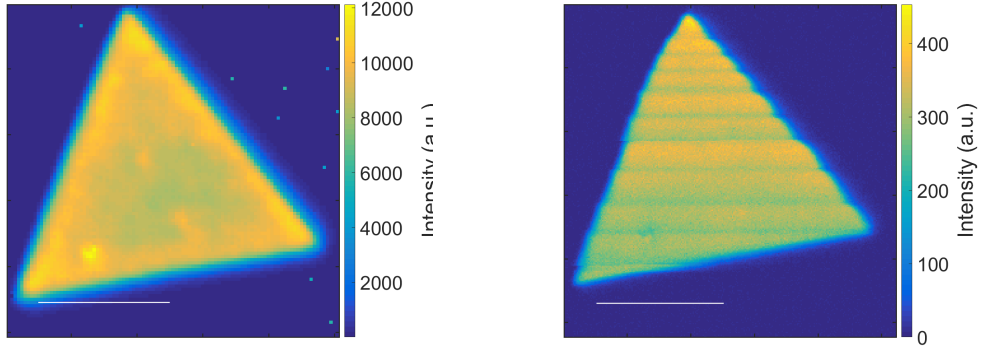
A typical map of PL intensity of a *WSe₂* sample can be seen in Figure 25a. The PL



(a) Typical PL spectrum from monolayer WSe_2

(b) Typical Raman spectrum from monolayer WSe_2

Figure 24: PL and Raman spectra from monolayer WSe_2



(a) PL intensity

(b) Raman E_{2g}^1 intensity

Figure 25: PL intensity and Raman E_{2g}^1 intensity maps

intensity is homogeneous throughout the flake. It does not exhibit the trisecting pattern as seen in WS_2 samples e.g. Figure 25a.

A comparison of PL peak positions and widths between different samples of WSe₂ can be seen in Figure 26.

By plotting the intensity and width of the PL peaks against the peak position as seen in Figure 27 certain patterns can be observed. The intensity is mostly grouped around maximum values and relatively narrowly spread across the position spectrum. The thick flakes show much more even distribution of intensity across the position, which combined with the wide distribution of positions results in a much more inhomogeneous sample. The width and positions are generally well grouped with flakes with smaller width having

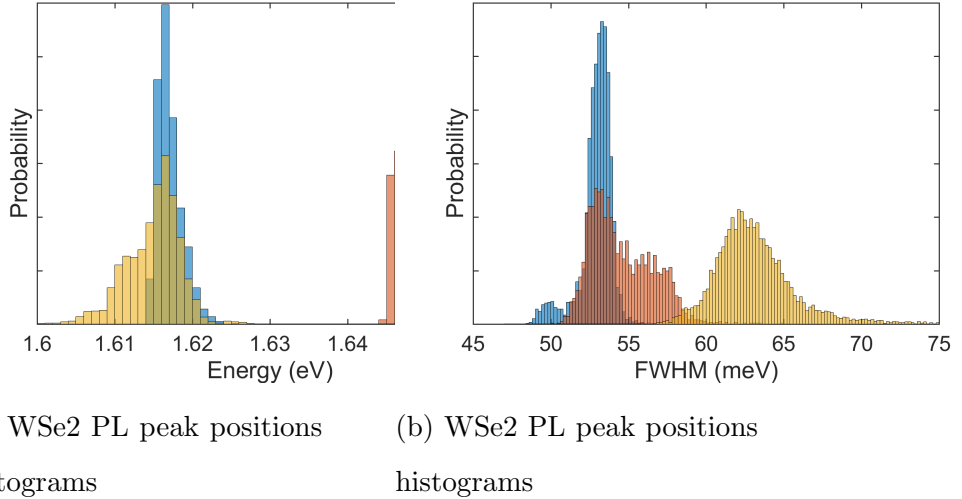


Figure 26: Comparison of PL peak positions and widths in different WSe_2 samples

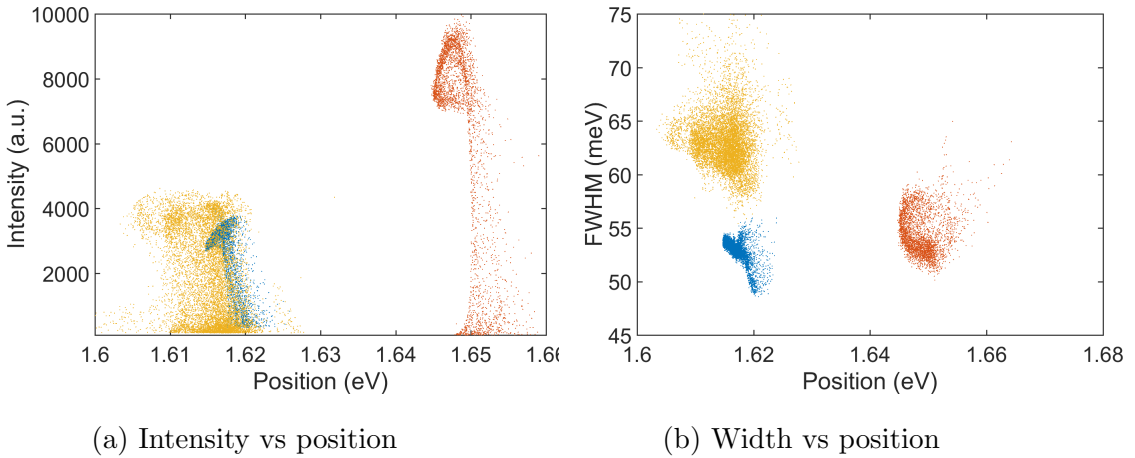


Figure 27: PL peak parameters distribution

more narrow distribution than those with greater width. Also few-layer flake shows a smaller peak width. Overall there is no obvious relation between position and width.

The Raman spectroscopy is a very useful characterisation technique for TMDCs. For most TMDCs it can be used to identify the number of layers or strain within the layer. However in the case of WSe_2 the position of the E_{2g}^1 and A_{1g} largely overlaps and therefore it is difficult to accurately determine the difference in their position. Because of that this method of identifying the number of layers cannot be employed easily. It is however still possible to examine the strain within the layers by noting the shift of the E_{2g}^1 peak. A Raman E_{2g}^1 peak position distribution from a representative sample can be seen in Figure 28. The strain can be then determined from the mean position of $250.678 \pm 0.095 \text{ cm}^{-1}$

to be 2.44 % [11].

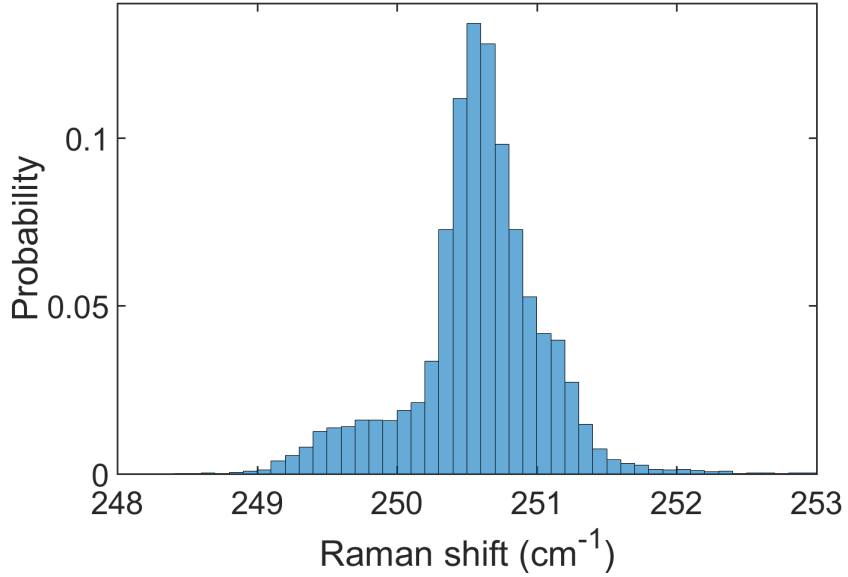


Figure 28: Histogram of Raman E_{2g}^1 peak position from monolayer WSe_2

The sample has been further characterised with XPS. Three areas were selected for measurements, one with thin, mono or double layer WSe_2 , one with thick bulk WSe_2 and one with no visible WSe_2 flakes. The Figure 30 shows W4f core levels measured in those spots. The first area (Figure 30a), with thin flake shows one doublet at 32.08 eV and 34.23 eV and a second doublet at 35.33 eV and 37.68 eV. The first doublet corresponds to WSe_2 while the second one can be attributed to WO_3 . Since the spot size in the measurement covers both the flake as well as some surrounding substrate it is possible that the WO_3 is located outside of the flake. Furthermore the background indicates that the emission from WS_2 came from surface and therefore the WS_2 flake is not contaminated with WO_3 . The second area with thicker flakes (Figure 30b) shows similarly two doublets: one at 32.28 eV and 34.43 eV and a second one at 35.38 eV and 37.63 eV. Similarly to the thin area with thin flake we can ascribe the former to the WS_2 and the latter to WO_3 . There is a small shift of 0.2 eV between WS_2 from the thin flake and WS_2 from the thick flake. It is possible that XPS is sensitive to the number of layers in WSe_2 and TMDCs in general since it is known that number of layers does modify the electronic structure of the material. The WO_3 is found to be at the same position in both areas. The WO_3 peak is also relatively weaker in the area with the thick flake than in the area with thin flake which could be a result of the thick flake having larger surface area than the thin flake and smaller presence of WO_3 around the flake. Additionally and empty area (Figure 30c)

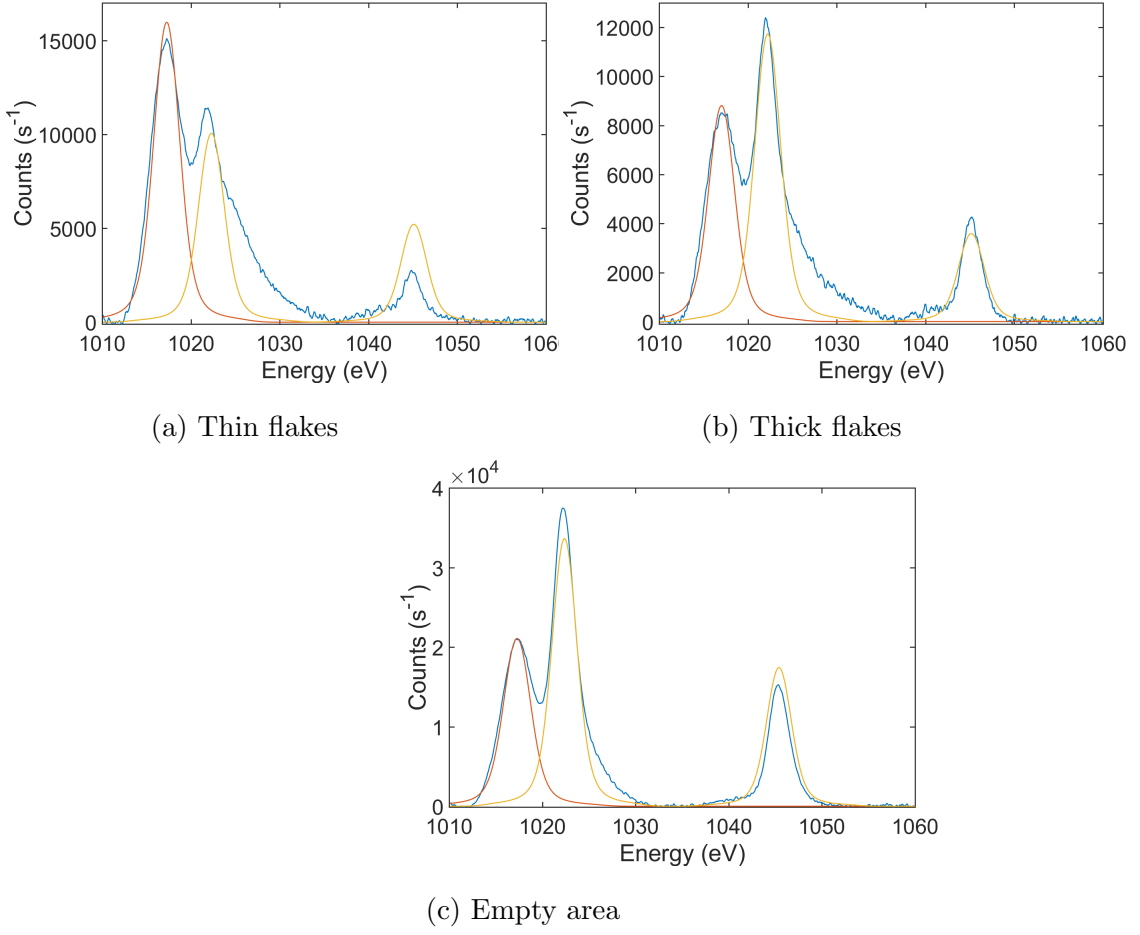


Figure 29: XPS spectra of Zn2p peaks in different areas of the sample

with no visible flakes have been measured. Similarly two doublets, one at 32.58 eV and 34.73 eV and a second one at 35.48 eV and 37.58 eV have been fitted and their presence can be again explained by presence of WS_2 and WO_3 . The WS_2 peak is shifted in relation to that from the thin flake by 0.5 eV which could indicate presence of a highly defective WS_2 or very small amounts of very bulk WS_2 . The WS_2 peak is also much weaker than that of the WO_3 which is expected since no visible WS_2 flakes were observed.

We can also look at Se3d core levels measured at the same locations. As seen in Figure 31a, taken from an area with the thin flake, we can fit it with one doublet corresponding to the presence of WS_2 at 54.48 eV and 55.23 eV. Similarly in Figure 31b we can see Se3d peaks taken from area with the thick flake and can fit it with a doublet at 54.63 eV and 55.38 eV which also corresponds to the WS_2 . Similar to the W4f levels there is a shift of 0.15 eV between those two flakes which can be explained by their thickness which changes the electronic structure. The Se3d levels measured in the reference empty area also can be fitted with a doublet at 54.53 eV and 55.33 eV which can be attributed to

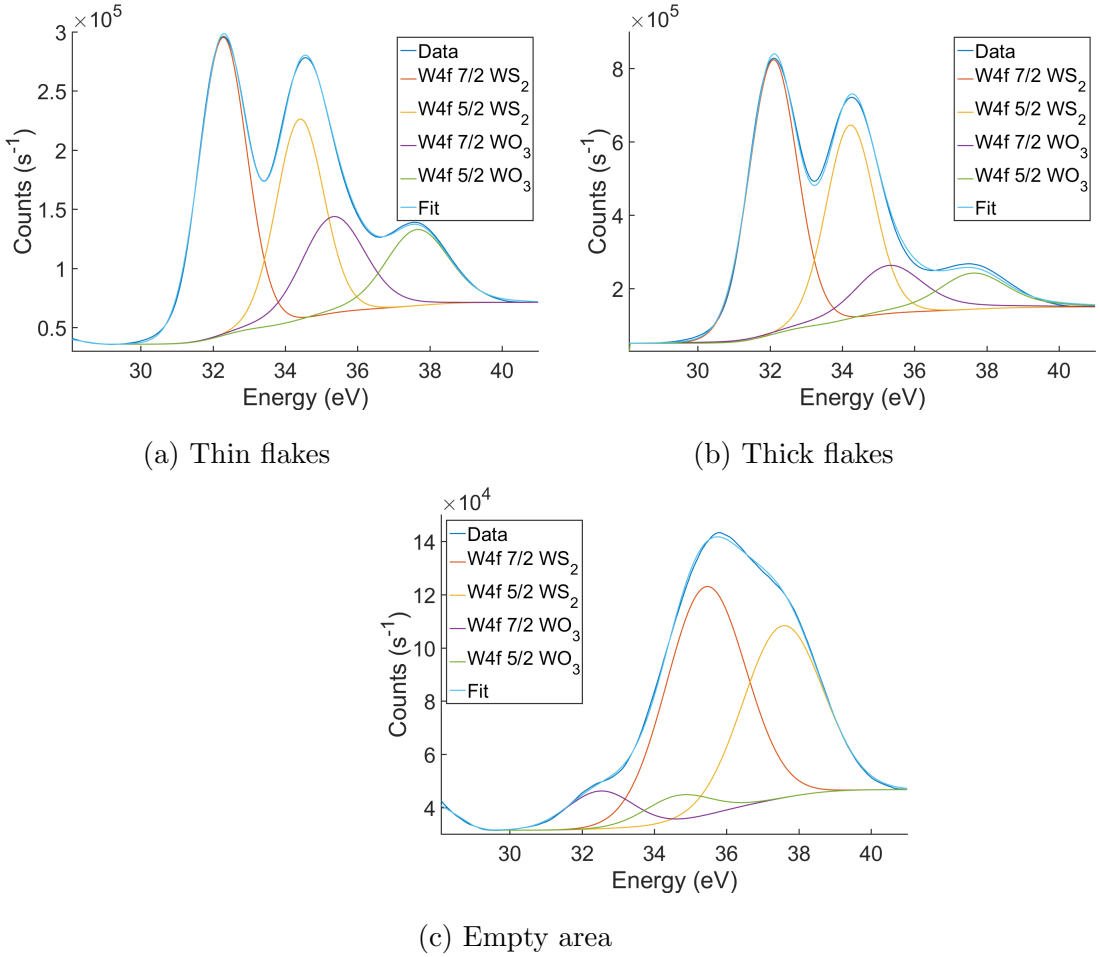


Figure 30: XPS spectra of W4f peaks in different areas of the sample

WS_2 . Similarly there is a shift of 0.05 eV from the peak associated with the thin flake, which is much smaller than the W4f peak shift. The Se3d peak from the empty area is about a magnitude weaker than that from either the thin or thick flake which is expected as no visible flake was observed. It does however indicate a non insignificant presence of WS_2 , perhaps in the form of nuclei that never grew into proper flakes or flakes that shrunk or became etched and are highly defective and thinner than monolayer. The Se3d from the empty area also exhibits a steep background which indicates that the Se is covered with some layer, perhaps that of WO_3 .

Finally the Zn2p levels were measured across the same areas. As seen in Figure ?? a doublet can be identified at

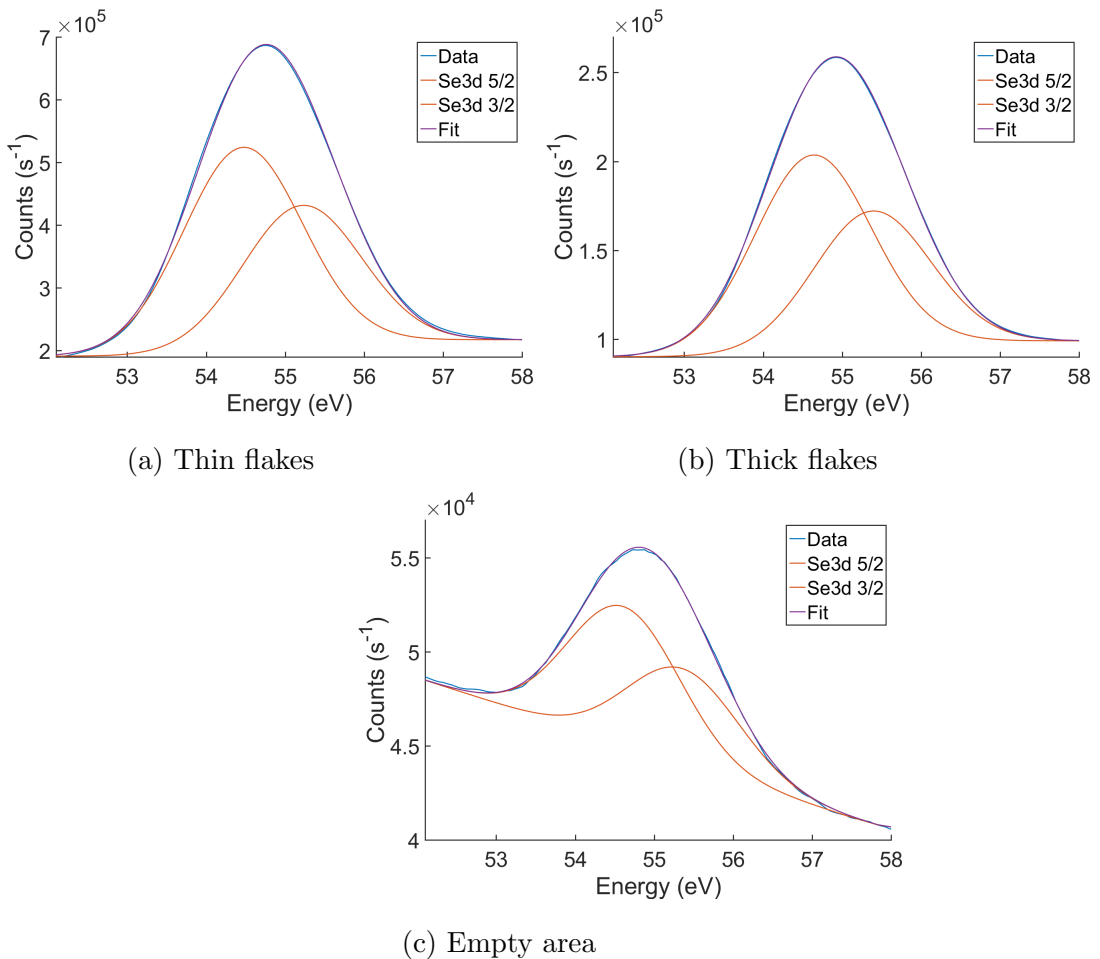


Figure 31: XPS spectra of Se3d peaks in different areas of the sample

4 Transfer

4.1 Introduction

The most common method of producing the TMDCs is CVD. During the CVD growth the process the substrate and the sample are heated to very high temperatures, up to 1000 °C. Because of that there is substantial thermal expansion in both substrate and sample. However due to difference in thermal expansion coefficient between those two elements there is potential build up of thermal strain. Additionally because the substrate, upon which the sample is grown, is heated to such high temperatures that it cannot be used for electrical measurements. More specifically the thermal expansion coefficients of WS_2 and SiO_2 are on the order of 10^{-3} and $10^{-7} K^{-1}$ respectively [24][64]. Therefore it is expected that during cooling down the WS_2 will come under tension due to thermal expansion coefficient misalignment. Moreover in order to use TMDCs as components in devices different layers have to be arranged together either vertically or laterally. Due to aforementioned reasons there is a need to develop methods for transferring single layers of TDMCs from one substrate to another one. In this chapter a focus is put on transferring WS_2 monolayer flakes from SiO_2/Si onto other surfaces.

4.2 Experimental

The most common method of transferring flakes synthesised via CVD method is a wet transfer method utilising as an intermediate substrate. In such procedure a thin layer of PMMA is first spun on top of the substrate. After drying the substrate is placed in a KOH aqueous solution (6% to 8%) heated to about 50 °C. As a result the thin layer of SiO_2 on top of Si is dissolved leaving a PMMA with the sample attached to it floating on top of the solution. The PMMA is then rinsed in water several times and scooped up onto a new substrate. Next the sample is dried and annealed to ensure good adhesion and remove wrinkles and strain. Then the PMMA is removed with a solution of acetone and IPA at about 50 °C. Any remaining PMMA can be removed by annealing the sample at about 100 °C.

4.3 Results

A sample has been investigated using Raman and PL spectroscopy before and after transfer. In Figure 32 a comparison between samples before and after transfer can be seen in

PL spectra. The as grown sample shows mostly homogeneous PL intensity, position and FWHM across the sample with the exception of the edge and trisecting lines in the middle where the PL intensity is higher and lower accordingly. In the sample after transfer the PL intensity, position and FWHM is more randomly distributed across the flake and there is a distinct lack of edge enhancement or the presence of trisecting lines.

The position of the PL peak from the as grown sample is $1.9765 \pm (9.8445 \times 10^{-4})$ eV, while the PL peak position from transferred sample $1.9703 \pm (8.3518 \times 10^{-3})$ eV. Therefore the peak position is shifted by 6.2 meV after transfer while the relative standard deviation is about 8.5 times greater in the transferred sample than in the as grown sample. The FWHM in the as grown sample is 36.3693 ± 0.7982 meV while in the transferred sample the FWHM is 83.2706 ± 6.7947 meV. The FWHM then increases by 46.9013 meV while the relative standard deviation increases 3.726 times compared to the as grown sample.

The Raman E_{2g}^1 peak position in the as grown sample is 350.8681 ± 0.2064 cm^{-1} while in the transferred sample is 351.3407 ± 0.2893 cm^{-1} . The relative uncertainty is therefore 1.3997 greater in the transferred sample. The position of the Raman A_{1g} peak in the as grown sample is 418.6530 ± 0.2829 cm^{-1} while in the transferred sample it is 417.3195 ± 0.4760 cm^{-1} . The relative uncertainty is therefore 1.6879 times greater in the transferred sample. The position difference between these two peaks is 67.7862 ± 0.2411 cm^{-1} in the as grown sample while it is 66.0040 ± 0.4757 cm^{-1} in the transferred sample. The relative uncertainty increases therefore by 2.0264 after the transfer. The intensity ratio between those peaks in the as grown sample is 5.7471 ± 0.6844 and after transfer it is 7.1609 ± 0.8899 . The relative uncertainty changes 1.5835 times after transfer.

It can be therefore seen that after transfer the relative uncertainty increases for every parameter of Raman and PL spectra maps. This indicates that the sample after the transfer is much less homogeneous. Because both the position of PL as well as the position of Raman peaks is affected by the strain the inhomogeneity can indicate a relaxation or build up of strain. Since the CVD growth method involves heating up the sample and the substrate to very high temperatures, up to $850^\circ C$, there is possibility of residual thermal strain after cooling down. Since the PMMA is much more flexible than the SiO_2 , that the sample is grown on, the WS_2 can relax before being placed on a new SiO_2 substrate. On the other hand the water present in between the WS_2 and PMMA can also be a source of strain. During the water evaporation the surface tension can induce local strain leading to high inhomogeneity. The PMMA can also have varying thickness and can swell to small degree therefore contracting in size during drying. Any or all of these effects can

potentially contribute to the variation in parameters observed.

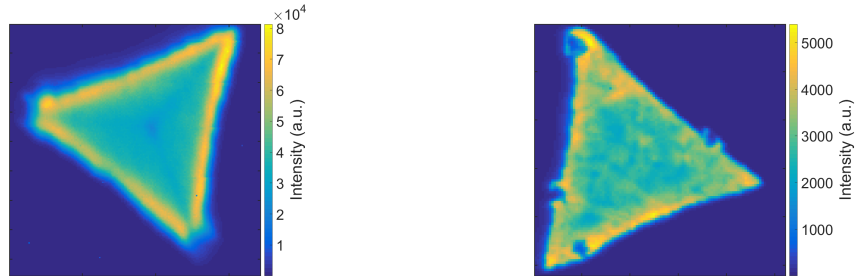
The average values of peak fitting parameters can be then compared between the two sample states to estimate the strain in the sample. The average position of $E_{2g}^1 + 2LA$ peak changes from 350.8601 cm^{-1} to 351.3407 cm^{-1} , a 0.4806 cm^{-1} difference. Since the position of this peak changes by $-3.1\text{ cm}^{-1}/\%$ this indicates the change in strain of -0.155% . The $E_{2g}^1 + 2LA$ peak intensity change ($\Delta I/I_0$) of 23.15% indicates a 0.23% change in strain. The average value of A_{1g} peak position changes from 418.6530 cm^{-1} to 417.3195 cm^{-1} , a difference of 1.3335 cm^{-1} . This indicates then a strain of -4.445% . The intensity change of A_{1g} peak of 25.64% corresponds to 0.3344% strain.

The PL peak position changes from 1.9765 eV to 1.9703 which corresponds to change from about 1% to 0.75% strain, a -0.25% change.

By comparing different average Raman and PL peaks fit parameters it is not clear to what extent the WS_2 is strained before or after the transfer. Neither the direction nor the extent of strain can be estimated then in the sample overall. The difference in deviation of these values however indicates that the sample after transfer is less homogeneous than before. Therefore while it cannot be said that the sample strain changes on average as a whole, there is a change in strain across the sample. While the thermal strain should result in the sample as a whole being under tension due to thermal expansion and contraction other effects could still take place like aforementioned variation in water presence, inhomogeneity of PMMA layer thickness or folds in PMMA layer.

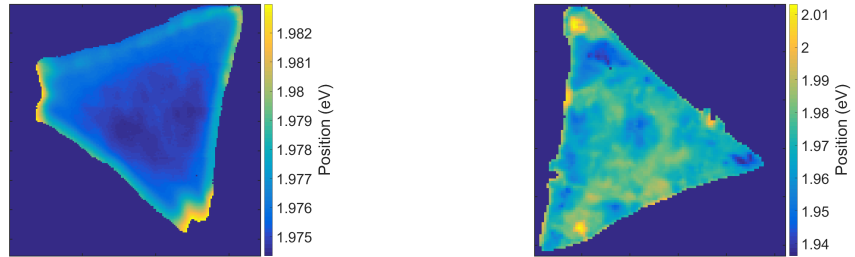
4.4 Conclusions

It is unclear to what extent the CVD grown WS_2 sample is strained prior to transfer or after it. The difference in relative uncertainty of different fitting parameters of PL and Raman spectra however reveals that the sample becomes less homogeneous following the procedure. This could indicate that the strain becomes introduced during the transfer via a non uniform presence of water, non uniform thickness of PMMA layer, folds in the PMMA layer or presence of residue PMMA.



(a) PL Intensity map of as grown sample

(b) PL Intensity map of transferred sample



(c) PL Position map of as grown sample

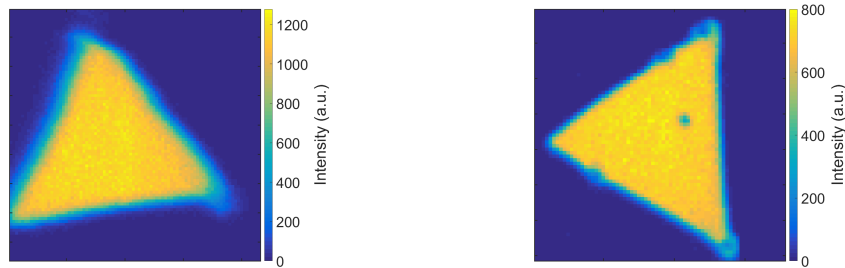
(d) PL Position map of transferred sample



(e) PL FWHM map of as grown sample

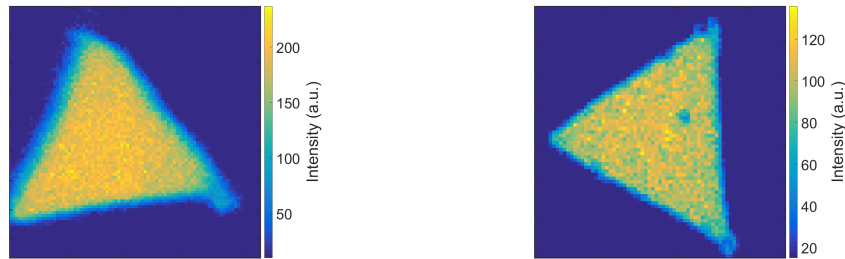
(f) PL FWHM map of transferred sample

Figure 32: PL spectra maps of samples before and after transfer



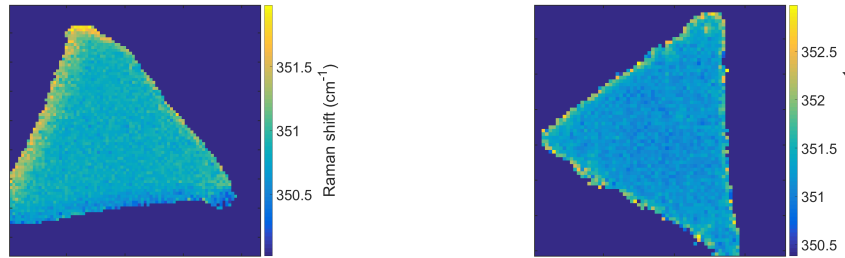
(a) Raman E_{2g}^1 intensity map of as-grown sample

(b) Raman E_{2g}^1 intensity map of transferred sample



(c) Raman A_{1g} intensity map of as-grown sample

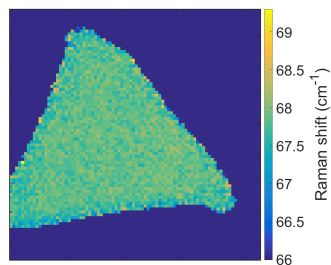
(d) Raman A_{1g} intensity map of transferred sample



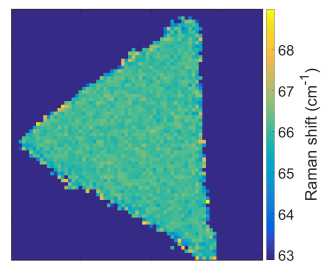
(e) Raman E_{2g}^1 position map of as-grown sample

(f) Raman E_{2g}^1 position map of transferred sample

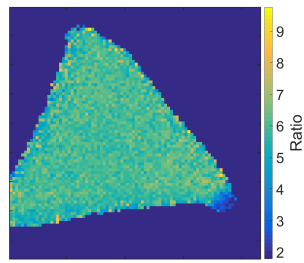
Figure 33: Raman spectra maps of samples before and after transfer



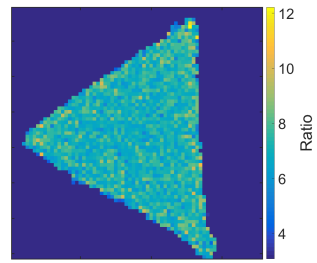
(a) Raman peak position difference map of as grown sample



(b) Raman peak position difference map of transferred sample



(c) Raman peaks ratio map of as grown sample



(d) Raman peaks ratio map of transferred sample

Figure 34: Raman spectra maps of samples before and after transfer

5 Low T PL

5.1 Introduction

As the temperature of the semiconductor goes down the number of charge carriers decreases. Because of this in WS_2 the number of electrons is expected to be lower at low temperatures. Additionally as the temperature drops the peak broadening due to temperature effects i.e. Gaussian broadening decreases. At room temperature the thermal energy is equal to about 25 meV which limits the smallest possible width of the peak and therefore the resolution. Both of those effects should result in the peak at low temperatures to be overall weaker and more narrow than that at the room temperature. Additionally the lower electron density should result in lower population of trions. Due to lower temperature the electron and hole mobility should also decrease and cause the excitons to be more often trapped at defects sites also known as bound excitons.

5.2 Experimental

In order to perform the low temperature measurement the sample was placed in an environmental stage, Linkam THMS350V. The stage allows the sample to be cooled down to the temperatures of liquid nitrogen (LN_2) and at pressures of down to 10^{-3} mbar. The stage was then placed in a Renishaw Raman spectroscope chamber and the spectra were collected using 532nm green laser.

5.3 Results

The PL measurements were taken from the WS_2 monolayer on Si/SiO_2 sample at different conditions. As seen in Figure 35 the PL from has been measured in the same spot at lower pressure (2×10^{-2}) and different temperatures, room temperature and liquid nitrogen (LN_2) temperature ($-196^\circ C$). The PL from that spot at room temperature is centred at 1.957 eV and has FWHM of 44.3 meV. After lowering the temperature to that of LN_2 i.e. $-196^\circ C$ the PL measurement was taken again and the intensity of the peak was found to be about 0.81 that of the RT. Additionally the position of the PL at lower temperature was found to be 1.969 eV and the FWHM was 37.9 eV.

The PL spectra were then fitted with 2 peaks to resolve the trions and excitons. The results can be seen in Figure 36. Similarly the PL spectrum from room temperature has been fitted with two peaks. The intensity ratio between the exciton and trion in the low

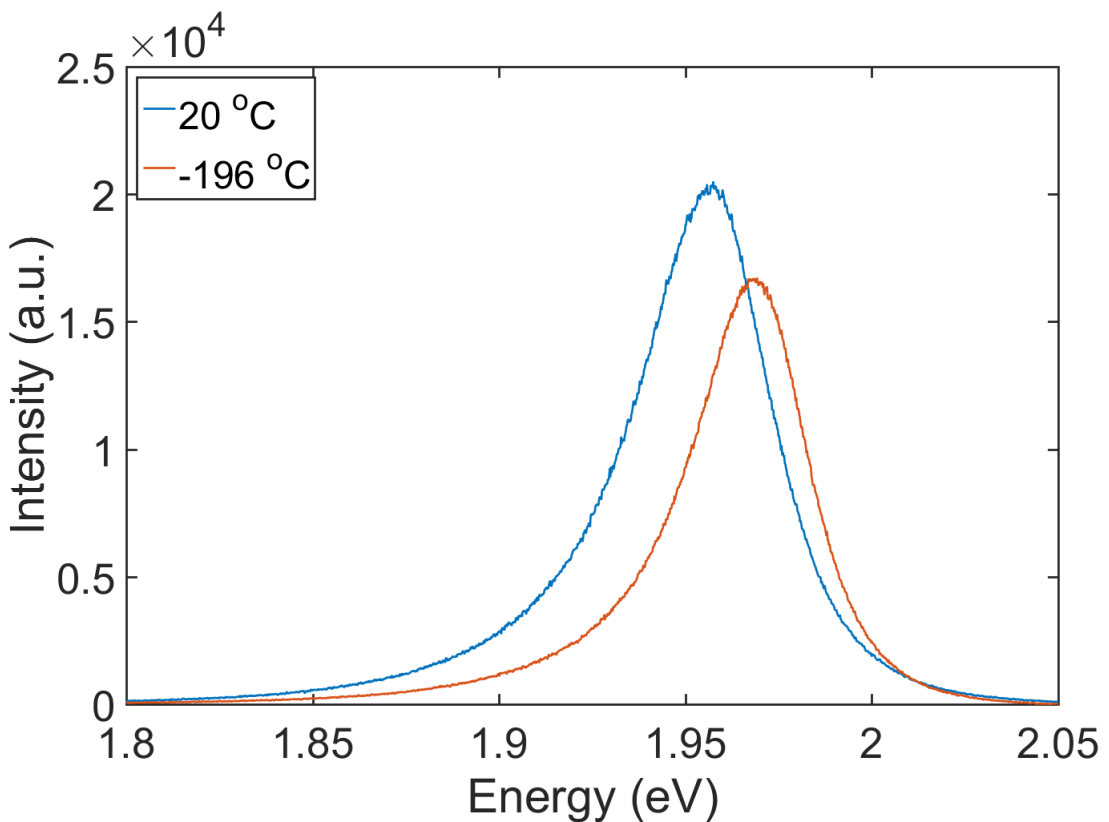


Figure 35: PL spectra of samples at room temperature and LN_2 temperature at 2×10^{-2} mbar

temperature sample is about 4, while at the room temperature it is 3. The FWHM of the exciton peak also lowers from 36 meV to about 32 meV.

This indicates that indeed as the temperature is lowered the FWHM of the PL peak and especially the exciton component also lowers. However the difference between the FWHM at room temperature and low temperature is not as big as expected if temperature was the main contributor to the peak broadening. For room temperature a thermal energy contribution should be about 25 meV while at LN_2 temperature (77 K) the contribution should be about half of that, i.e. 12 meV. The peak was fitted mostly with Gaussian lineshape (about 70%) and therefore the temperature should be a significant contributor to the peak width. It is possible that the laser heats up the sample during measurement since the thermal contact between the substrate and the cooled stage is weak. Additionally the glass window separating the stage and the room environment as well as the substrate itself can be covered in water droplets which could introduce refraction and therefore peak broadening.

Due to the low FWHM of the PL peaks a strong trion component can be observed as

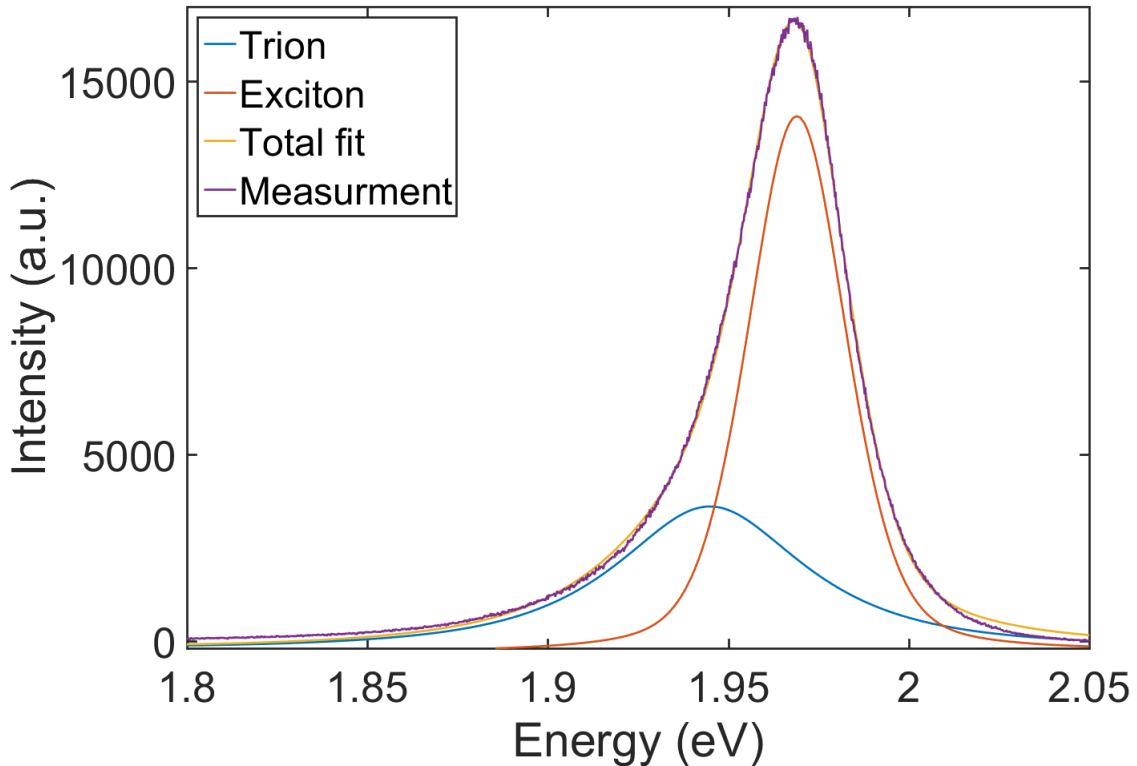


Figure 36: PL spectra at low temperature with trions and excitons components resolved

seen in Figure 37. While the lower temperature of the substrate can explain the small FWHM, the trion component is much stronger than in standard measurement environment. This could be caused by the low pressure which results in less oxygen and water molecules adsorbed at the defect sites. At standard conditions (1 atm) these species adsorb at the defect sites and attract electrons which as a result lowers the overall n-doping level of the material.

In order to check the influence of the pressure on the PL and potential effect of the adsorbed oxygen, nitrogen and water molecules measurement at different pressures was conducted. As seen in Figure 38 as the pressure is lowered by several orders of magnitude the PL peak is shifted to the red. The FWHM of the PL peak at the ambient pressure is about 41 meV while at lower pressure (1.5×10^{-2} mbar) it is about 44 meV. The exciton to trion intensity ratio changes from 3.387 to 3.25 from the ambient pressure to low pressure. It therefore indicates that as the pressure is lowered the trion component becomes more prominent and the peak overall shifts to lower energies.

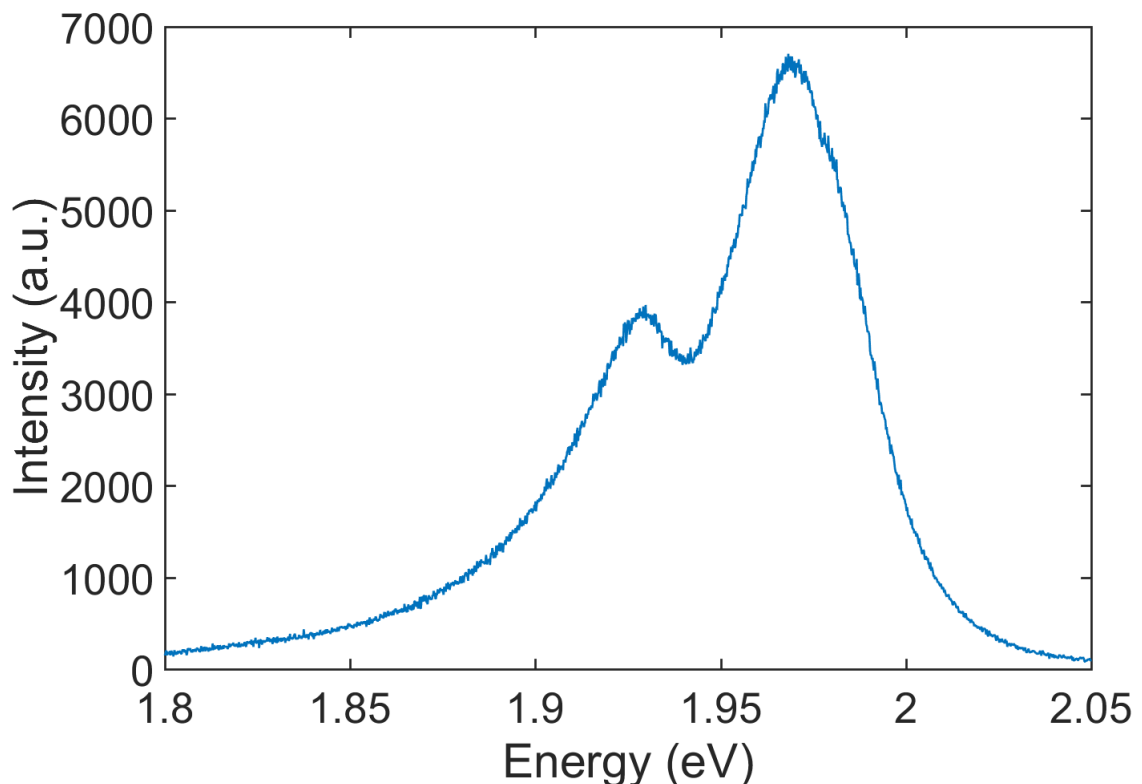


Figure 37: Low temperature PL spectrum with easily resolved strong trion component

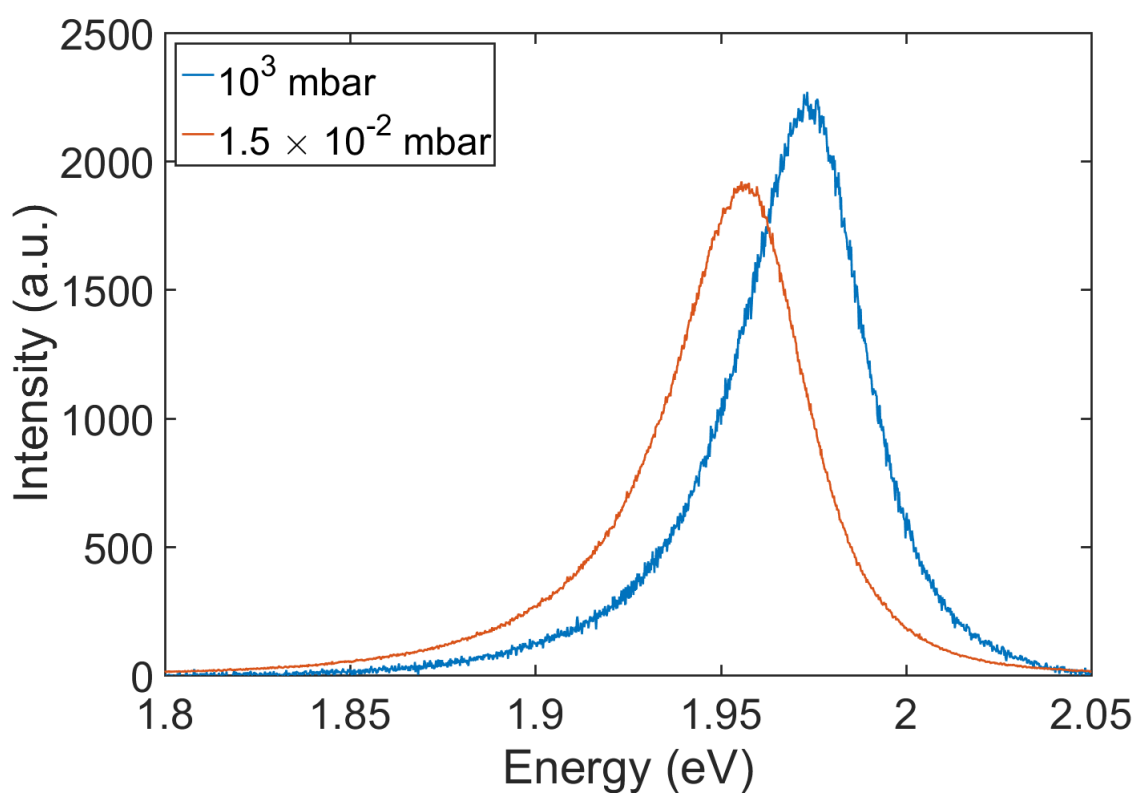


Figure 38: PL measurements at different atmospheric pressures

6 1T' WSe_2

6.1 Introduction

The

7 TMDC phases - review

7.1 Introduction

TMDCs, as mentioned in the introduction 1.4, are layered materials. In addition to the number of layers they can be also be primarily differentiated based on their structural polytype. The most common polytype seen in both mechanically exfoliated as well as CVD grown materials is the 2H phase. The name of it refers to the number of layers required to repeat the pattern as well as the symmetry, in this case the hexagonal symmetry.

8 Introduction

As two-dimensional TMDCs have emerged as promising candidate materials for next-generation electronic and optoelectronic technologies with valley functionalities it has become apparent the need of enhancing some of their properties in view of their applications. For instance, creating band offsets between different monolayer TMDCs would enable efficient separation of charge carriers and rectification of charge flow. This would offer a mechanism for designing devices made by entirely van der Waals atomically thin materials. Furthermore, the semiconducting monolayer TMDs—MoS₂, MoSe₂, WS₂ and WSe₂—are also interesting because they possess direct bandgap in the visible region at energy degenerate band edges (valleys), spin–valley coupling and valley-contrasting electronic and excitonic properties. The valley physics of TMD excitons have been intensely studied in the past few years, with recent advances including the optical generation and control of exciton valley coherence. However, as the valley degree of freedom is affected by very fast recombination time (picosecond timescale) would impede any possible exploitation of the valley-functional optoelectronic devices based on valley excitons in monolayer TMDs in practical applications. The fabrication of bilayered van der Waals (vdW) heterostructures would enable to fully exploit the potential of TMD in electronic, opto and valleytronic applications.

9 Properties of bilayer heterostructures

As it has been explained in Chapter 1, TMDs undergo a crossover from indirect bandgap in the bulk to direct bandgap in the monolayer form. As a consequence of this direct band gap, monolayers absorb and emit light rather efficiently. The band structure changes as a function of the number of layers due to the strong interlayer coupling, which results in different shifts in the conduction and valence band edges at various symmetry points in the Brillouin zone as a function of the layer number. Vertical sTMDs heterostructures formed by stacking up different monolayers offer a rich collection of physics and functionalities. Theory predicts that any stacked MX₂ heterostructures form type II semiconductor heterojunctions and thus it facilitate efficient electron–hole separation. This would be particularly beneficial for light harvesting and light detection applications. It has been

further demonstrated that the charge separation can occurs over ultra fast time scales, such as femtosecond [22]. In type II semiconductor heterojunctions, the conduction band minimum and valence band maximum are found in two separate materials. If electrons and holes are photoexcited they will then prefer to stay in different materials. The alignment of electronic bands of MoS₂ and WS₂ monolayers as predicted [] is reported in Figure ???. It shows that monolayer MoS₂ and WS₂ have bandgaps of 2.39 eV and 2.31 eV, respectively, and the MoS₂ valence band maximum is 350 meV lower than that of WS₂ and the conduction band level is also lower. Thus in this material system, the conduction band minimum resides in MoS₂ and the valence band maximum in WS₂. This heterojunction structure can lead to efficient charge transfer upon optical excitation with separated electrons and holes residing in two layers. XX et al has demonstrated that the electron-hole separation occurs in 50 fs. The fast separation can be particular beneficial in solar-driven applications such as photoelectron catalysis and solar cells as it reduces the chances of immediate recombination of the charges. We have demonstrated that the formation of this type of heterojunction of chemically exfoliated MoS₂/WS₂ and assembled in a form of thin films can be beneficial for photoelectrochemical water splitting []. In Chapter XX we discuss the formation of MoS₂/WS₂ heterostructures in the form of thin films via CVD and their identification via physical characterization. The same structures have been used for photoelectrochemical water splitting. In general, the most studied bilayer heterostructures is formed by MoS₂ and WS₂ monolayers. This is due to the fact that synthesis of these materials via CVD is better established as compared to the selenides materials.

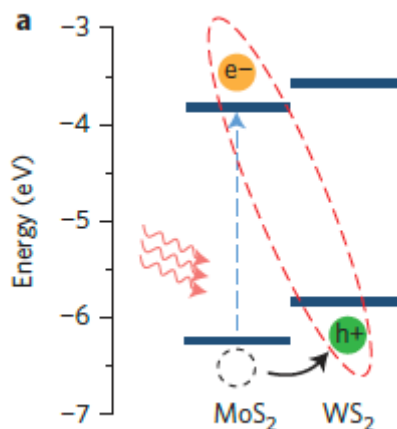


Figure 39: Charge separation across heterojunction following photoabsorption

10 Fabrication of bilayer heterostructures

The first studies of heterostructures of TMDCs have been based on CVD materials. Two different approaches have been adopted. The first strategy was based on the transfer of two monolayers priorly synthesized independently. While the second approach, which has not seen nearly any further work on, was based on the direct synthesis of heterostructures via CVD.

10.0.1 Transfer -approach

WS₂/MoS₂ heterostructures have been prepared from conventional PDMS stamping method from CVD grown monolayers [1]. In the first report about this [1], MoS₂ and WS₂ monolayers have been grown by high-pressure CVD technique onto SiO₂/Si substrates. The CVD MoS₂ monolayers were continuous over 1mm with large, single-domain crystals reaching up to 75 microns while the CVD WS₂ monolayers were in the form of individual triangle islands of 5-50 microns in size. The fabrication process consisted in a first transfer of the WS₂ monolayers onto PDMS substrates, followed by stamping the WS₂ monolayers onto CVD MoS₂ monolayers, which formed vertical heterostructures of WS₂/MoS₂ [1]. The overlap region (approximately 40 μm) of MoS₂ and WS₂ monolayers show slightly darker contrast under the optical microscope and it is the region which has been characterized by Raman spectroscopy and photoluminescence and electrical measurements.

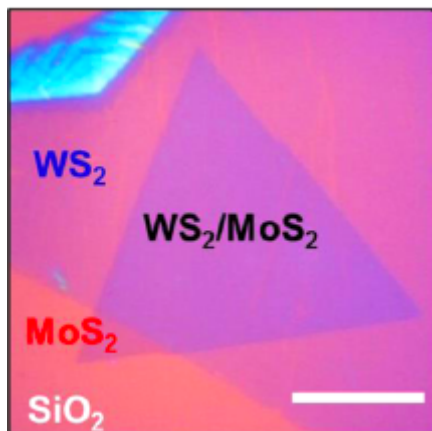


Figure 40: Optical micrograph of the heterostructure of WS_2/MoS_2

10.0.2 Direct synthesis of vertical heterostructures

Firstly, with the term, vertical heterostructures, we differentiate those from the lateral heterojunction created by two adjacent and consecutive layers of two different TMDs. This terminology differentiates these two different types of heterojunction which can be obtained by direct CVD synthesis. The direct synthesis of bilayer heterostructures have been obtained via CVD where molybdenum trioxide (MoO_3) powder was placed in front of a bare SiO_2/Si wafer for the growth of MoS_2 in a tubular furnace. A mixed powder of tungsten and tellurium was scattered on the wafer for the growth of WS_2 . A small amount of tellurium was used to accelerate the melting of tungsten powder during the growth [1]. Upstream in a low-temperature zone, the sulphur powder was placed. The furnace was heated up to the temperature range of 650-850 °C and argon gas was used as a carrier gas to protect the system from oxygen and carry sulphur vapour from the upstream of the tube during the reaction. The difference in the nucleation and growth rates of MoS_2 and WS_2 and the chosen growth temperature favours the sequential growth of MoS_2 and WS_2 , instead of the formation of their ternary alloy ($Mo_xW_{1-x}S_2$ alloy). Vertically stacked bilayers were found to grow preferentially at temperature of 850 °C, whereas in-plane lateral heterojunctions were found at 650 °C. The CVD synthesis can lead to clean interfaces [same nature materials paper][our paper submitted] between the two monolayer components, in contrast with mechanical transfer of layers or assembly from liquid phase. A typical optical, SEM and atomic force microscopy (AFM) images of the layers are shown in Fig XXX. The bilayers can be easily distinguished from monolayers via optical contrast (Figure 41), with MoS_2 monolayers showing a light purple colour and the bilayer regions a much darker purple.

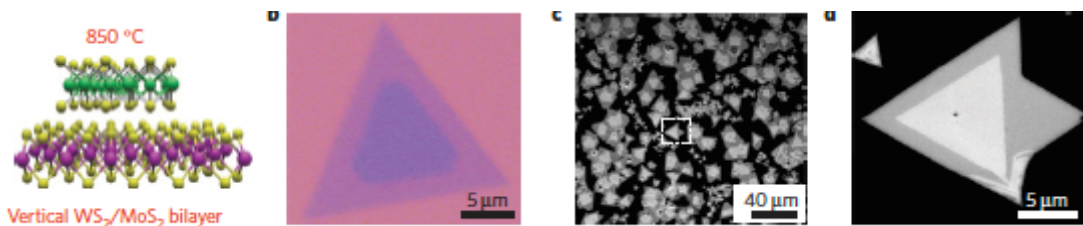


Figure 41: Heterostructure imaging

10.1 Characterization of bilayer heterostructures

10.2 Raman spectroscopy

Heterostructures fabricated by both these approaches were characterized by Raman spectroscopy. As the vibrational modes of MoS_2 and WS_2 are quite different the Raman spectrum of the heterostructure displays in-plane (E_{2g}^1) and out-of-plane (A_{1g}) modes of MoS_2 and WS_2 at the same frequencies as in their monolayers. The WS_2 E_{2g}^1 and A_{1g} modes are located at 350 cm^{-1} and 416 cm^{-1} while for MoS_2 they are at 380 cm^{-1} and 405 cm^{-1} respectively. Spatial maps show consistently distinct signal from each of the two layers using both fabrication techniques (Figure ??). In the transferred bilayered heterostructures there is a clear difference between the Raman modes position of the as transferred materials versus an annealed heterostructure. The position of the peaks for each material in the as transferred materials is compatible with monolayers while after annealing (at the temperature of XXC) the peaks are affected by redshift/blueshift as it is characteristics of bilayer materials. This result suggest that as a consequence of annealing ($120\text{ }^\circ\text{C}$ at $\sim 0.13\text{ Pa}$ for 6 h) there is an increased interlayer interaction. The fact that no changes are observed in the E modes in plane can be explained with the fact that they are generally less sensitive to changes in the environment. The increased interaction has been also revealed by AFM where the step height of the bilayer heterostructure can be reduced from 1.6 nm toward the expected 0.8 nm by annealing. This can be explained with the possibility that such annealing is able to drive out trapped residual molecules, such as water. In the CVD grown materials, the Raman peaks appears at XXXcm⁻¹ respectively for WS_2 and MoS_2 . These values are compatible with a bilayer structures of the annealed transferred samples. This suggest there is an increased interaction between the layers in CVD grown materials in line with layered bulk materials.

10.3 Photoluminescence

The vertical heterostructures were further characterized by photoluminescence (PL) spectroscopy. The as transferred heterostructures manifest PL peak typical of MoS_2 and WS_2 . The spectrum can be defined as additive. The PL peak of MoS_2 show intensity much higher WS_2 and this was attributed to possibly higher density of defects in WS_2 associated with its higher growth temperatures. After annealing the WS_2/MoS_2 heterostructures, the PL spectrum gradually changes. The transition as seen in Figure 44 from transferred

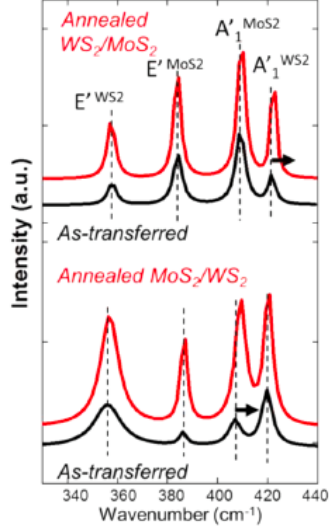


Figure 42: Heterostructure Raman spectrum

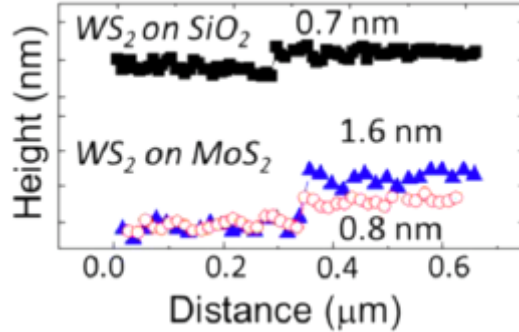


Figure 43: Comparison of AFM profiles of WS_2 on Si/SiO_2 and MoS_2

to fully annealed bilayer heterostructures occur through the followings: (1) A new PL peak (P_{hetero}) appears at 1.94 eV, and its integrated intensity grows for prolonged annealing time. (2) Upon the annealing, P_{MoS_2} and P_{WS_2} gradually decrease up to the point of appearing as small features at lower and higher energy of the P_{hetero} peak (3) at the end of 12 hours of annealing, another weak emission peak ($P_{indirect}$) appears at 1.75 eV, and the peak position rapidly and eventually red-shifts to 1.5 eV.

The explanation for this trend has been the following. As a consequence of the transfer the two monolayers end up well separated from each other due to residual water molecules and/or impurities trapped between the sheets. This large distance has been assessed by AFM (Figure XX). This system display PL peaks characteristics of isolated monolayer MoS_2 (P_{MoS_2}) and monolayer WS_2 (P_{WS_2}). After the annealing, the PL peak intensity of MoS_2 (P_{MoS_2}) and WS_2 (P_{WS_2}) decreases and two new peaks appear, called P_{hetero} and

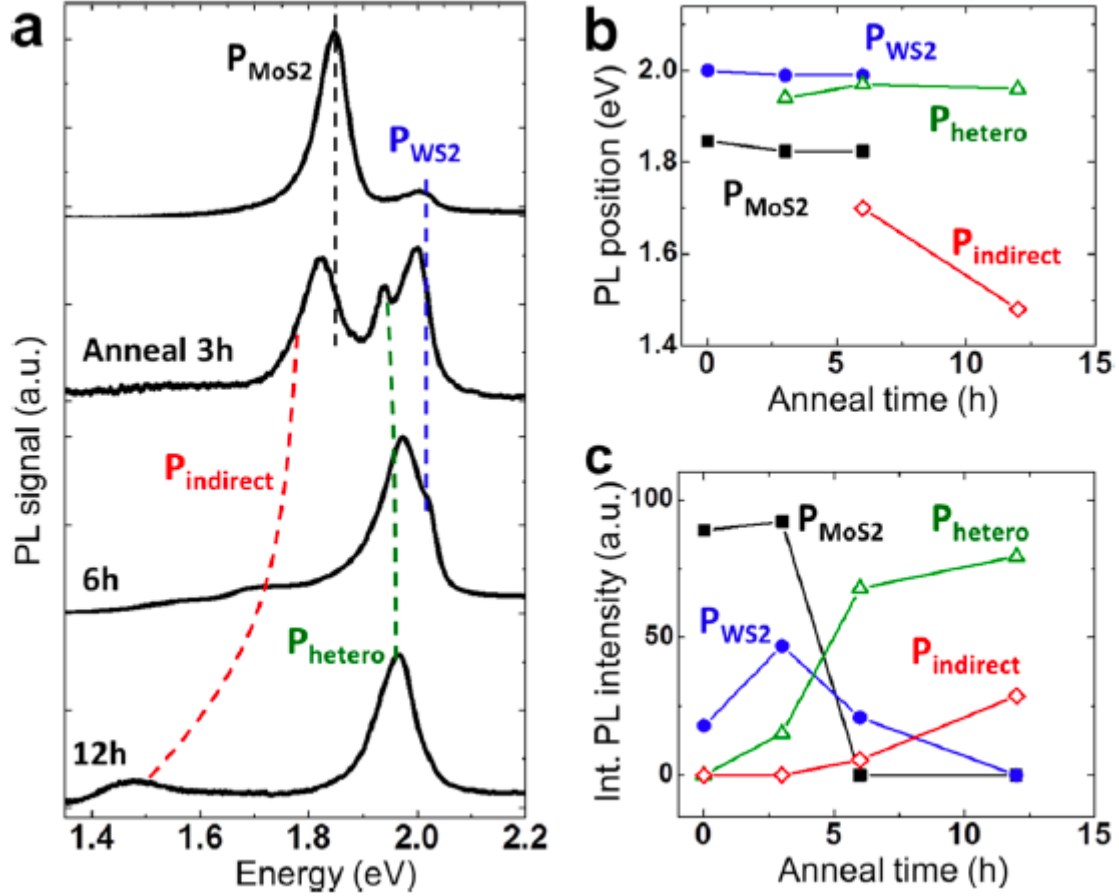


Figure 44: PL Spectrum of heterostructure

P_{indirect} , with the former arising from the electronic coupling between the two monolayer materials while the latter arising due to the indirect band gap formed at the interface of the heterobilayer (Figure XX). Because the P_{indirect} peak position changes rapidly with the degree of coupling (annealing time). This has been attributed to a phonon-assisted, indirect bandgap transition, which involves the valence band maximum (VBM) at the Γ -point and the conduction band minimum (CBM) at the K-point. To prove this hypothesis, the authors have fabricated by transfer method a $\text{MoS}_2/\text{MoS}_2$ heterostructure and the indirect peak has similar behaviour. This suggested that the indirect peak can be associated with a similar behaviour as the bulk material. DFT calculations has supported this hypothesis []. The formation of a type II heterojunction led to establishing a large electric field which develops across the 1 nm thick junction. This leads to strong exciton splitting by which holes (electrons) are rapidly swept from MoS_2 to WS_2 (from WS_2 to MoS_2).

The CVD grown heterostructures shows a bandgap of 1.42 eV while at the same time

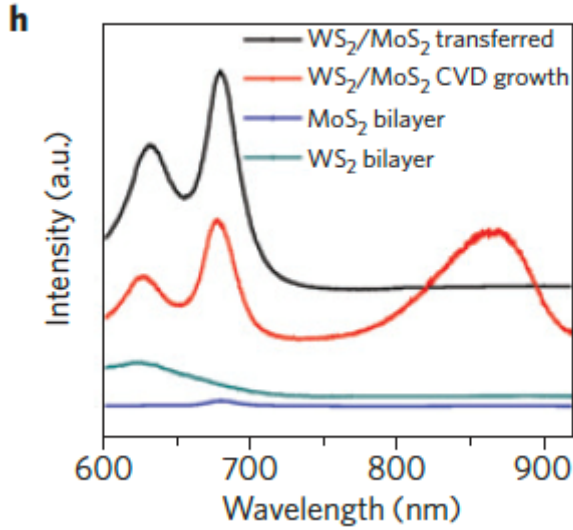


Figure 45: Comparison of PL spectra

separate pronounced PL peaks of MoS_2 and WS_2 can be seen (Figure 46 []). Subsequent studies have tremendously developed the understanding of the heterobilayer PL behaviour. The main factor which has been taken into consideration in the following studies is the mismatch angle between the lattices orientations of the two monolayers. Experimentally, it was found that the twist angle in a heterobilayer determines the photoluminescence efficiency of interlayer excitons (bound electrons and holes situated in adjacent layers) and their peak position. It has been hypothesized that twist-angle-dependent interlayer orbital hybridization can cause the variation in the photon emission energies of indirect excitons in heterobilayers (e.g. MoS_2/WSe_2) and also in MoS_2 bilayers. Additional experimental work has reported similar results [][].

Specifically, in a study by Kunstamnn [35] the heterobilayer region of MoS_2/WSe_2 shows the peaks of the two individual materials are discernible among with a new peak near 1.6 eV. This has been interpreted as the indirect exciton, and renamed as interlayer exciton (ILE). By altering the twist angle between the $MoSe_2$ and WSe_2 layers from 0° to 30° the ILE peak intensity has decreased and further from 30° to 60° the intensity has increased again. Similarly the ILE peak position has blueshifted from 0° to 30° and redshifted back from 30° to 60° . The separation between the layers is also found to be highest at about 30° and smallest at 0° or 60° . At the same time the other PL peaks, associated with monolayer WSe_2 and MoS_2 , are unaffected. The ILEs can be therefore associated with the K- Γ transition.

Very recently, Alexeev et al [1] have shown the latest achievement in the field consist

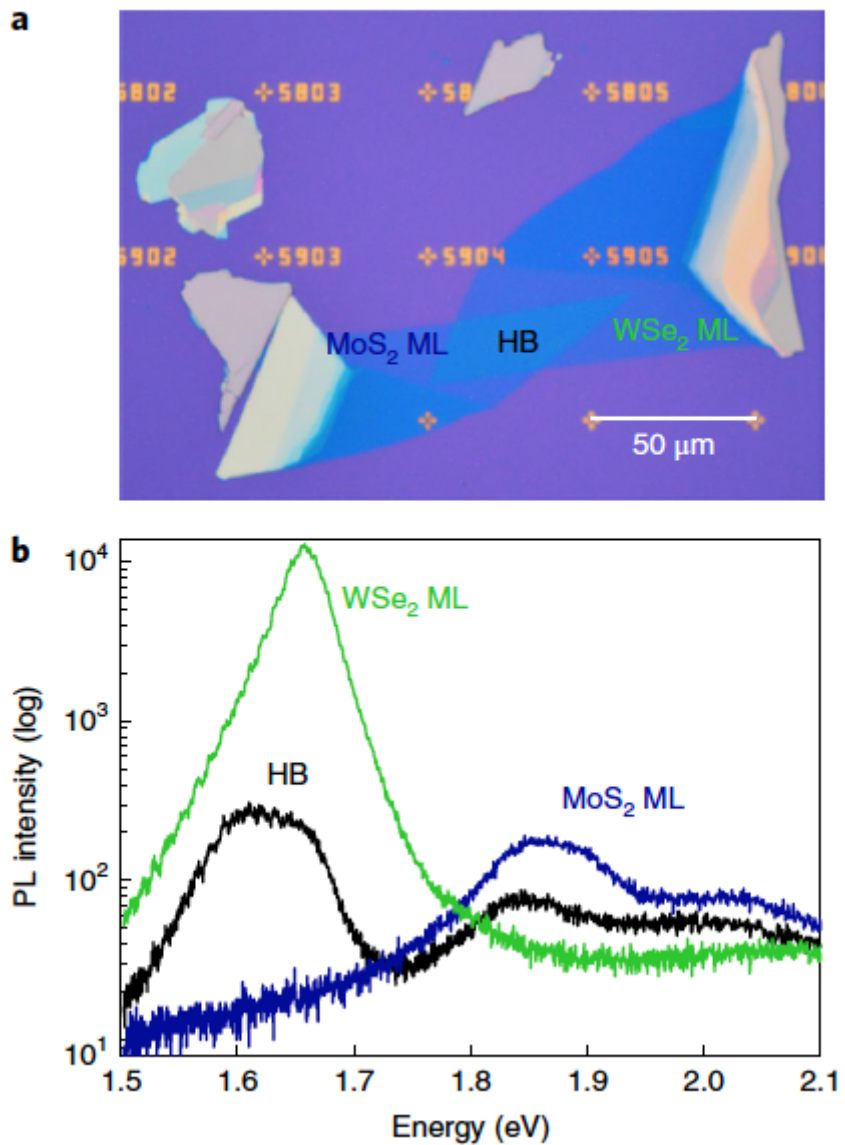


Figure 46: PL spectra taken from heterostructure [35]

of bilayered TMDs heterostructures formed by transfer of CVD grown TMD as well as mechanically exfoliated.

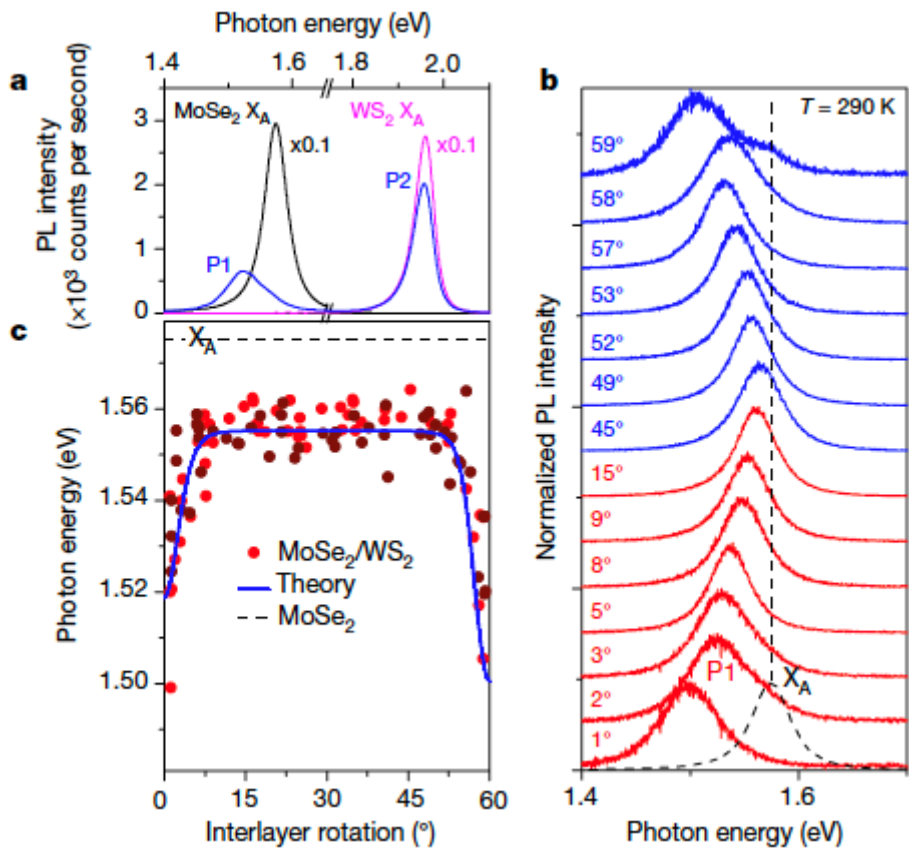


Figure 47: PL spectra of heterostructure [1]

11 Heterostructures

11.1 Introduction

One of the potential applications of the heterostructures is as photocatalyst for water-splitting reaction. The dimensionally confined materials, such as TMDCs offer many advantages in comparison to more commonly used materials. The large surface to volume ratio allows many catalytically active sites, generally higher carrier mobility and tunable bandgap of many of the TMDCs makes them suitable for efficient absorption of sunlight. Most commonly studied TMDCs, MoS_2 and WS_2 exhibit valence band edge more positive than the oxidation potential of water (1.23 eV) and can therefore act as a photoanode.

While a single material like MoS_2 or WS_2 can be used alone as a photocatalyst by forming a type II heterojunction additional benefits can be exploited. The presence of the heterojunction allows for holes to migrate to WS_2 valence band while electrons move to MoS_2 conduction band. As a result the physical charge separation delays the exciton recombination and allows for efficient water splitting.

Commonly a liquid phase exfoliation (LPE) has been used to deposit TMDC layers on a conduction substrates like gold. However this method results in highly defective material with small flakes and solvent residue adsorbed to the basal plane. In contrast the other commonly used technique of CVD has been utilised primarily to grow TMDC layers on top of resistive substrates like SiO_2/Si . In order to increase the size of the flakes as well as reduce the number of defects the heterostructures were grown by CVD onto gold substrate to allow for direct application as a photocatalyst.

11.2 Results

Monolyer MoS_2 , and WS_2 can form a type II heterojunction with matching crystal lattice parameters, which allows for ultra-fast charge separation and transfer between the discrete materials [7][69]. Recently, we have exploited the fast charge separation, demonstrating that MoS_2/WS_2 bulk heterojunctions obtained via deposition from solution of chemically exfoliated atomically thin layer are suitable photoelectrocatalysts for water oxidation [54] with efficiency higher than the individual components. In this system, the holes in the valence band of WS_2 are responsible for the oxidation of water. By combining WS_2 and MoS_2 in a heterostructure, charge carrier separation is promoted through the favourable band alignment of MoS_2 and WS_2 , where the holes accumulate into the

WS_2 valence band, and electrons are transferred to the MoS_2 conduction band. This physical charge separation suppresses fast electron/hole recombination, enabling efficient water oxidation to take place. However, it is emerging that crystal defects in TMDCs can significantly impair catalytic performance and lead to poor stability under electrochemical testing.[80][68][51][78][56]. Liquid phase exfoliated (LPE) 2D flakes are plagued by defects including sheet-edges, basal-plane S vacancies, and solvent residues adsorbed on their basal plane [80][79][62]. These defects are unavoidable for materials synthesized by LPE where the lateral size of the sheets is normally sub-micrometric. Chemical vapour deposition (CVD) can produce material with high crystal quality and extended over extended lateral sizes in a clean environment and thus it is a promising technique to address these issues [57]. Whilst CVD has been studied to produce bilayer MoS_2/WS_2 heterostructures, these are typically grown on resistive substrates, implying arduous transfer steps to test electrochemical properties [8]. Further CVD produces an epitaxial interface between heterostructure components reducing trap-states which limits the charge transfer between components [65].

Growth of MoS_2/WS_2 heterostructures Growth of uniform heterostructures was achieved via CVD from transition metal oxide hydrate precursors on gold foils over 2 cm^2 (for full experimental details please refer to supporting information Figure 48). The growth parameters were adapted from our previous work where we have demonstrated large lateral size and high mobility monolayer WS_2 on SiO_2/Si [57]. The high carrier mobility is crucial in minimizing the carrier recombination rate in PEC systems [40]. CVD growth on gold foils allows combined lateral and vertical growth modes of TMD flakes (Figure 49) [61].

The dual growth conformation where a vertical geometry of the flakes supersedes the initially formed flakes parallel to the substrate, can be more easily achieved on Gold rather than SiO_2 , due to the high capture rate of sulphur during the nucleation stage of CVD growth [16]. This ensures good adhesion to the substrate by the conformal flakes (Figure 49 b) and a high available surface area by the flakes grown perpendicular to the substrate (Figure 49 c-e). Further, the exceptionally large lateral flakes size are retained despite this change in nucleation and growth mode (Figure 49 d, e).

A WS_2/MoS_2 heterostructure has been prepared by one step growth CVD. As a first step the heterostructure has been grown on SiO_2/Si using parameters developed for monolayer growth. An optical micrograph of a select area of the sample can be seen in

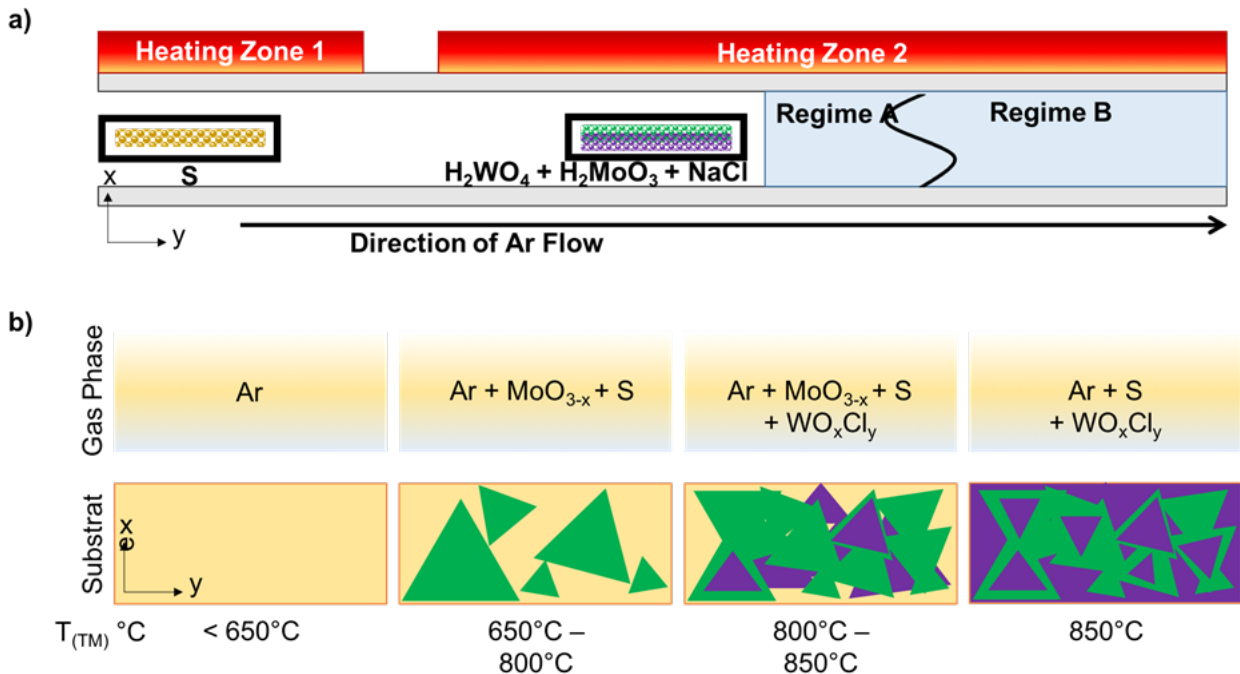


Figure 48: Schematic of the CVD growth process for tunable heterostructure and alloy synthesis; a) representation of the precursor positions, heating zone, and substrate in space; and b) simplified representation of the gas phase components and nucleation and growth on *Si/SiO₂* (green colour = Mo region; purple colour = W region).

Figure 50. The sample contains large areas of monolayer and bilayer TMDCs with some very small flake of bulk material. Overall the material coverage is quite high.

The sample was then characterised using Raman and PL spectroscopy. A measurement of Raman spectrum was taken from heterostructure and as seen in Figure 51 a distinct spectrum of *WS₂* and *MoS₂* can be distinguished. The Raman peak positions are 350.1 cm^{-1} , 382 cm^{-1} , 408.3 cm^{-1} and 417.7 cm^{-1} which can be ascribed to *WS₂* E_{2g}^1 , *MoS₂* E_{2g}^1 , *MoS₂* A_{1g} and *WS₂* A_{1g} respectively. Those peak positions correspond to multi layers of the individual materials which indicates a certain level of interaction between the layers.

There is a monolayer and bilayer *MoS₂* found around the heterostructure area with no *WS₂* grown indicating that the *WS₂* flake has grown on top of the *MoS₂* layer. The area surrounding the heterostructure shows a spectrum as seen in Figure 52.

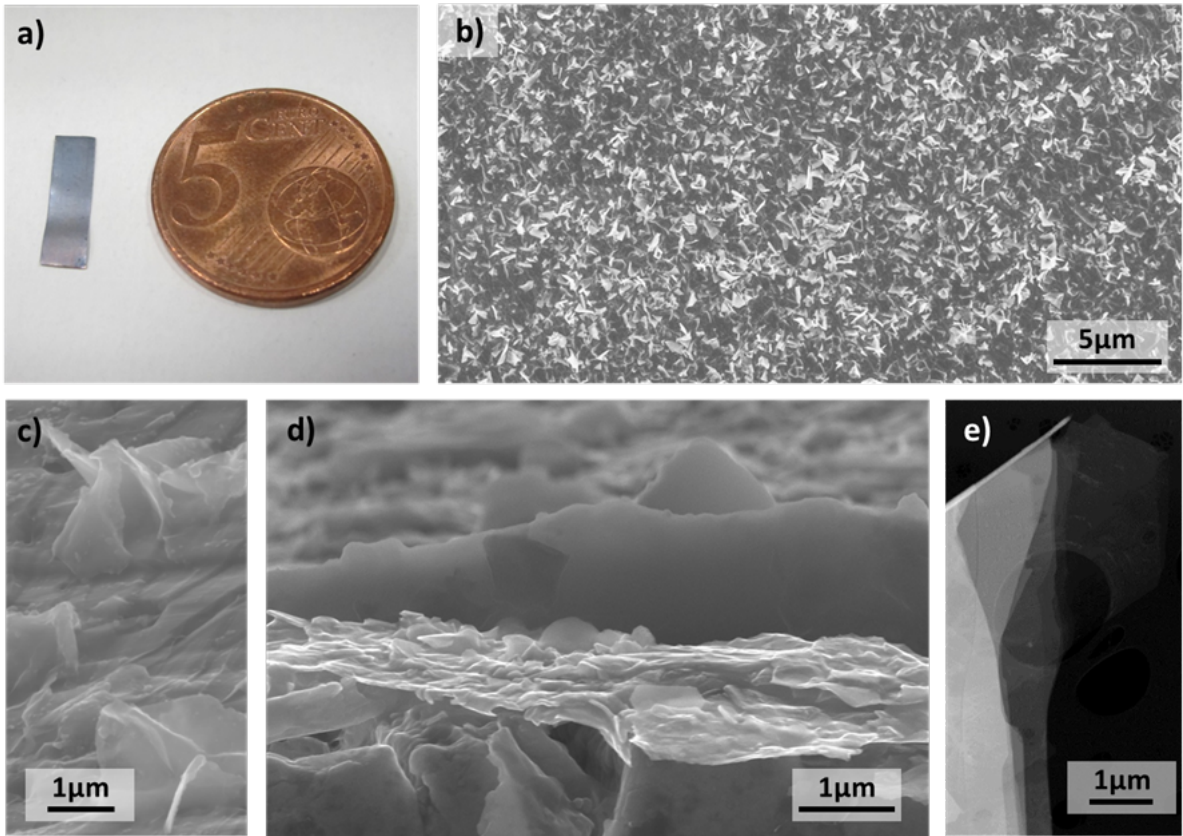


Figure 49: (a) Photograph of MoS_2/WS_2 heterostructure grown on gold; (b) scanning electron micrographs (SEM) of MoS_2/WS_2 heterostructures grown on gold showing continuous distribution of material; (c) side; (d) cross-sectional SEM image of combined lateral and vertical growth modes; and (e) STEM image of the edge of a flake.

The positions of the peaks are $382.7\text{ }cm^{-1}$ and $404\text{ }cm^{-1}$ for the monolayer and $382.4\text{ }cm^{-1}$ and $406.4\text{ }cm^{-1}$ for the bilayer.

The sample was then mapped using Raman spectroscopy. As seen in Figure 53 the intensity of E_{2g}^1 peak varies across the mapped area for both WS_2 and MoS_2 . The more intense areas indicate more layers of WS_2 which is placed on top of MoS_2 . Where the intensity of $WS_2 E_{2g}^1$ peak is higher and therefore there is more layers of WS_2 the intensity of $MoS_2 E_{2g}^1$ is reduced.

To better estimate the number of layers the difference between A_{1g} and E_{2g}^1 peak positions has been also calculated. By excluding the bulk flakes and leaving the flakes with less or equal to 3 layers of WS_2 it can be estimated that about 25% of the area is covered with WS_2/MoS_2 heterostructure.

The PL spectrum of heterostructure can be seen in Figure 55. There are two distinct peaks, one at 1.824 eV and second at 1.971 eV. The position of the MoS_2 PL peak

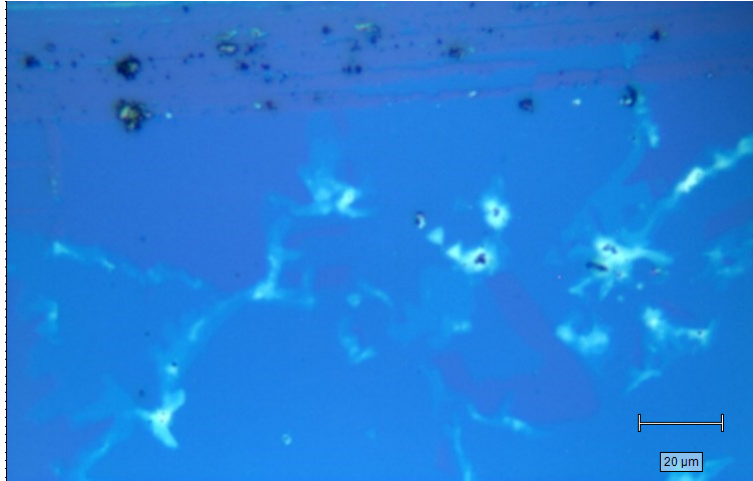


Figure 50: Optical micrograph of WS_2/MoS_2 heterostructure on SiO_2/Si

is consistent with the position of the monolayer MoS_2 as seen in Figure 56 which is 1.825 eV. Those PL peaks from heterostructure therefore correspond to both MoS_2 and WS_2 monolayers indicating that the spectrum is additive. The MoS_2 peak is also much stronger than WS_2 despite the fact that isolated monolayer of WS_2 shows much stronger PL than a monolayer of MoS_2 . The MoS_2 peak has a FWHM of 65.47 meV while the WS_2 PL peak has a FWHM of 142.4 meV.

The sample was also mapped using PL spectroscopy as seen in Figure 57. The most intense PL can be observed in areas of monolayer MoS_2 and much weaker everywhere else. The position map of PL peaks from both MoS_2 and WS_2 can be seen further in Figure ???. Most of the PL of MoS_2 is around 1.82 eV with some

The similar growth procedure was then used to grow WS_2/MoS_2 heterostructure on a gold substrate. As seen in Figure 59 the material coverage of the substrate is complete. The material also seems to be thick with irregular, rough surface. There are no visible triangles or continuous layers like seen in a SiO_2/Si substrate. This is most likely due to vertical growth which can occur on gold substrate as opposed to SiO_2/Si substrate.

The sample was then mapped using Raman spectroscopy. As seen in Figure ?? the WS_2 and MoS_2 Raman peaks E_{2g}^1 and A_{1g} can be identified.

As seen in Figure 61 the $MoS_2 E_{2g}^1$ can be seen across the entire scanned area. On the other the $WS_2 E_{2g}^1$ peak can be seen less spread around. Additionally the areas with high intensity $WS_2 E_{2g}^1$ coincide with low intensity $MoS_2 E_{2g}^1$. It implies therefore that similarly to the SiO_2/Si substrate the WS_2 grows on top of the MoS_2 which results in a weaker Raman signal from MoS_2 from areas where thick WS_2 has grown on top of the

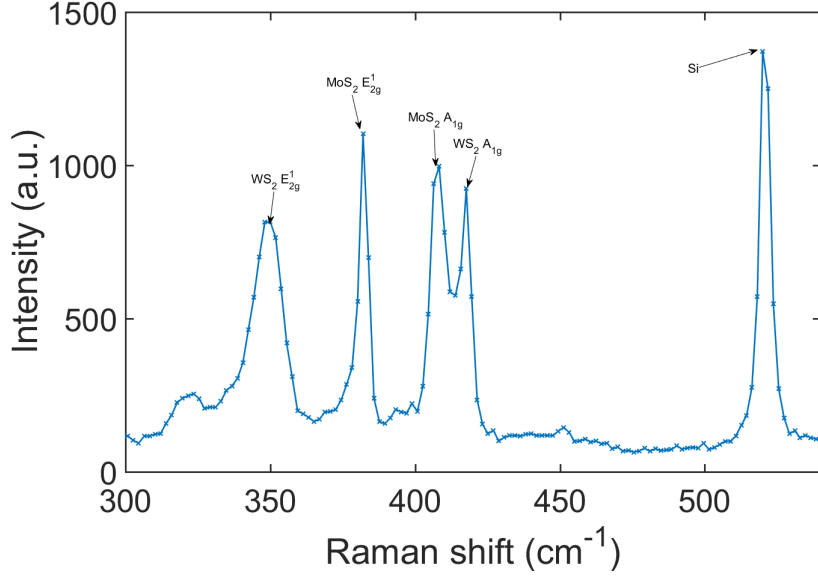


Figure 51: Raman spectrum of WS_2/MoS_2 heterostructure

underlying MoS_2 .

The peaks positions for WS_2 are on average $349.1\text{ }cm^{-1}$ and $418.5\text{ }cm^{-1}$ for E_{2g}^1 and A_{1g} respectively. Similarly for MoS_2 the peaks positions are $382.5\text{ }cm^{-1}$ and $408.6\text{ }cm^{-1}$ for E_{2g}^1 and A_{1g} respectively. This indicates that both MoS_2 and WS_2 are mostly few layers thick. It can be estimated that in the measured area the WS_2 coverage and therefore the WS_2/MoS_2 heterostructure presence is at least 8%.

Due to the gold substrate the PL is partially quenched which combined with weak PL signal coming from few layer WS_2 and MoS_2 makes it difficult to taken any meaningful measurement.

The fact that these flakes are epitaxial van der Waals heterostructures has been further proven by STEM energy dispersive X-ray spectroscopy (EDS) imaging (Figure 62 d-g, Figure 63). Further, these analysis elucidate that the growth mechanism can be described as initial nucleation of MoS_2 flakes prior to WS_2 due to the lower transfer temperature (and higher volatility of gas borne intermediates) of the utilised molybdenum oxide hydrate [$MoO_3 \cdot H_2O$] precursor ($750\text{ }^\circ C$) compared to the tungsten oxide hydrate [$WO_3 \cdot H_2O$] ($850\text{ }^\circ C$) [59][14].

High-resolution TEM imaging demonstrates a high crystalline nature of the basal planes of the heterostructures formed by atomic columns with the inter-planar distances of 2.6 \AA consistent with that of the (100) planes of 2H MoS_2 and WS_2 (2.73 \AA , the difference of 0.13 \AA falls within the expected error range) (Figure 66 b). Cross-sectional

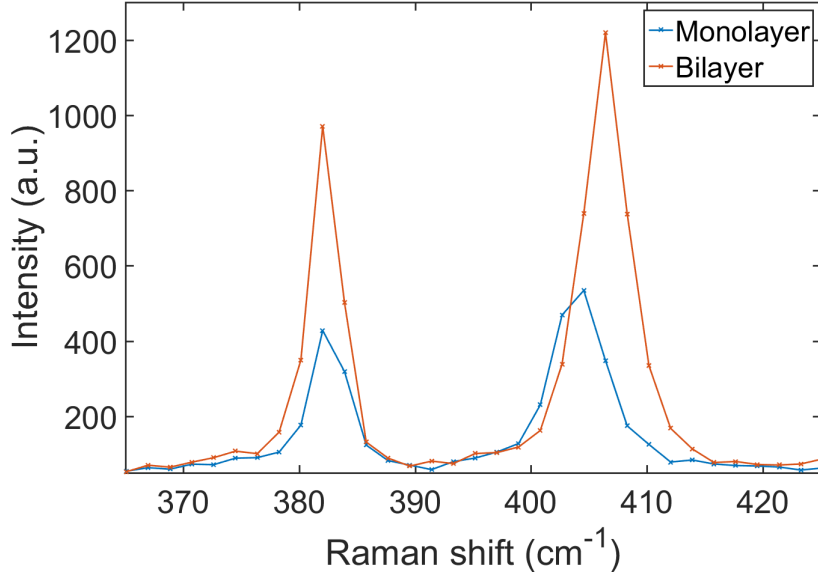


Figure 52: Raman spectra of mono and bilayer MoS_2

imaging along [002] direction additionally confirms a high crystalline nature of the lateral planes of the heterostructures. From SEM imaging, we can ascertain that the average sample thickness of the lateral growth mode is 80 ± 30 nm while the vertical growth modes reaches up to 400 nm vertically (Figure 64). STEM-EDS performed on individual, multi-layered, heterostructure flakes after photo-electrochemical cycling showed chemically pristine materials with individual sheets of MoS_2 (no W signal) and WS_2 (no Mo signal) within a single flake (Figure 65). The localized regions confirm the formation of individual sheets of MoS_2 and WS_2 within a single, epitaxial, van der Waals heterostructure.⁴⁵ The majority of flakes studied showed strong W and Mo signals due to overlapping regions of the heterostructures. The produced epitaxial MoS_2/WS_2 heterostructure forms a type-II heterojunctions with a stepped band alignment, allowing for hole transfer from the MoS_2 to WS_2 and electron transfer from WS_2 to MoS_2 , enhancing charge separation (Figure S7).[?][22][?]. The PEC activity of the heterojunctions for water oxidation are reported in the Appendix of this thesis.

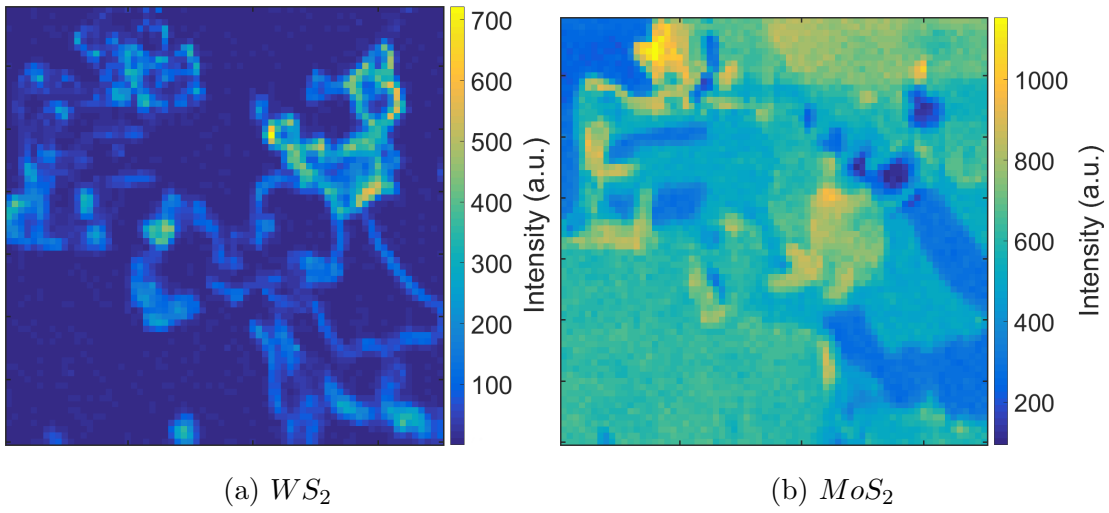


Figure 53: Map of Raman E_{2g}^1 peak intensity

11.3 Appendix

APPENDIX The PEC activity was studied in 3.5% w/v NaCl in DI water. Linear sweep voltammetry (LSV) was performed directly on as-synthesized samples with chopped illumination at 1.5 sun in both sweep directions, with visible bubbles appearing upon the electrode surface when illuminated at potentials ≥ 1.18 V vs RHE (Figure 67 a, b, Figure S8). An early onset of measureable photocurrent at $+0.48$ V vs RHE was observed with the maximum on off ratio at $+1.01$ V vs RHE (Figure S8 a). A bare gold foil, which had been subjected to the CVD process without the addition of Mo, W, or S precursors, was used as a control and showed no catalytic activity for water oxidation.

At potentials below $+0.4$ V vs RHE an inversion of the photocurrent was observed with significant instantaneous charge generation, however, negligible stable photocurrent was generated (Figure 67 b). This contribution arises due to the ambipolar characteristics of the TMDCs. In order to probe this effect, two stage chronoamperometry (CA) at -0.6 V vs Ag/AgCl and $+0.75$ V vs Ag/AgCl with chopped illumination was performed (Figure S8 b). The result of the chopped illumination at negative potentials was a slow increase in negative current flow upon illumination, which was recovered at approximately the same rate when the light source was blocked. When switched to positive potentials the previously described rapid water oxidation photocurrent was observed. CA performed at $+1.129$ V vs RHE, chosen to avoid oxygen bubble formation on the electrode surface, presented rapid charge generation immediately upon illumination followed by a stable photocurrent of 0.62 mA/cm² at 1.5 sun illumination intensity (Figure 67 c) (0.4

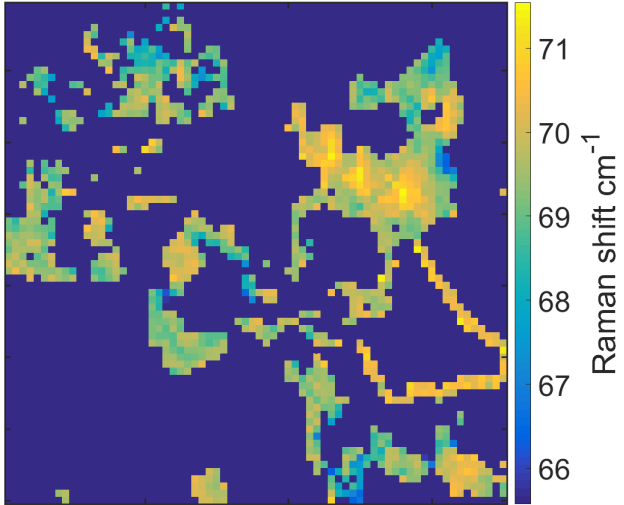


Figure 54: Difference between WS_2 A_{1g} and E_{2g}^1 peak position

mA/cm^2 at 1 sun, Figure S8 e). Sharp slopes in the chronoamperometry profiles collected under chopped illumination were observed, suggesting a faster charge carrier recombination as compared to liquid phase processed material [54]. The observed fast kinetics of charge carrier recombination allowed for photocurrent to be obtained at frequencies up to 1 Hz, while a stable photocurrent under constant illumination was observed for over 10 minutes (Figure S8 e). The photocurrent was confirmed to arise from the generation of oxygen through the use of an oxygen selective electrode, with an increase in the dissolved O₂ concentration from 5 to 17 $\mu\text{mol/L}$ upon illumination for 300 s (Figure S9). The Faradaic Efficiency (FE) for O₂ generation was calculated to be $83 \pm 15\%$, indicating a high proportion of photogenerated holes being available to produce oxygen. The use of monochromatic light to obtain incident-photon-to-current efficiency (IPCE) demonstrates that the photocurrent mimics the reflectance spectra of the heterostructure, with IPCE of 1.7% at 690 nm, confirming that these heterostructures are capable of operation in the visible range (Figure 67 d). The prominent features of both, reflectance and IPCE, are slightly red shifted from expected exciton positions for monolayer MoS_2 and WS_2 heterostructures (Table S1) [?]. The produced heterostructures demonstrates significant increase in efficiency compared to previously reported work on solution processed co-catalyst free TMDs for both hydrogen evolution (0.1 % IPCE) and water oxidation (0.1 % IPCE)[?][15]. The attained photocurrent of $1.7\text{ mA}/cm^2$ (increasing to $3.1\text{ mA}/cm^2$ in $NaClO_4$, Figure S7 c) at 1.19 V vs RHE in comparison to $5.35\text{ mA}/cm^2$ for the best-in-

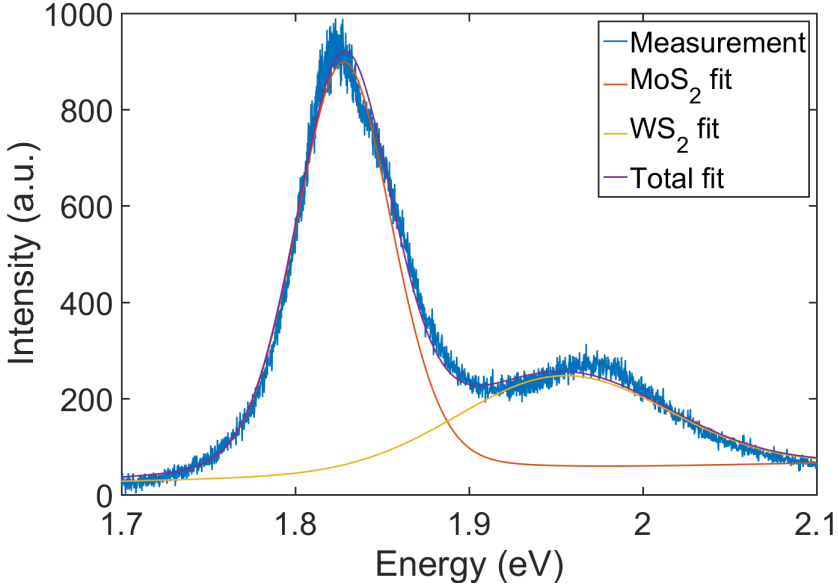


Figure 55: PL spectrum of MoS_2/WS_2 heterostructure

class $\text{FeOOH-NiOOH}/(\text{W},\text{Mo})-\text{BiVO}_4/\text{WO}_3$ materials is promising, especially at lower IPCE values [?]. Indeed, the highest measured photocurrent of $1.7 \text{ mA}/\text{cm}^2$ at 0.79 V vs Ag/AgCl is directly comparable to high performance Mo or W/ BiVO_4 composite systems $1.74 \text{ mA}/\text{cm}^2$ and $1.1 \text{ mA}/\text{cm}^2$ at 0.7 V and 1.1 V vs Ag/AgCl respectively.[?][?]. The FE of $83 \pm 15\%$ for the CVD grown heterostructure is comparable to reported efficiencies for high performance electro- and photo- catalysts [?]. This enhanced performance compared to analogous thin film hetrojunctions, [15] as recently elucidated for exfoliated WSe_2 ,[80][78] arises due to the highly crystalline nature of the flakes and their lateral size which is more than 100 times larger than the commonly used liquid phase exfoliated flakes. Large flakes sizes minimize recombination sites within our heterostructure and lead to the large grains overlapping with grain boundaries offset from one another. This offset allows for photo-generated charges to move laterally as well as vertically through the heterojunction with minimal recombination sites. These factors are proposed to minimize loss during charge transfer between MoS_2 and WS_2 layers. Finally, the relatively high volatility of utilized H_2WO_4 (and oxyhalide intermediates) ensures enriched WS_2 at the surface of the heterostructure (Figure 62) in contact with the electrolyte providing the ability for photo-generated holes, transferred in the WS_2 , to directly interact with water molecules. Additionally, the observed kinetics of charge carrier recombination has similar time-scales to those reported by Yu et. al. using WSe_2 (and WSe_2/Pt heterostructures) as photo-cathodes for the hydrogen evolution reaction.[?][80][79].

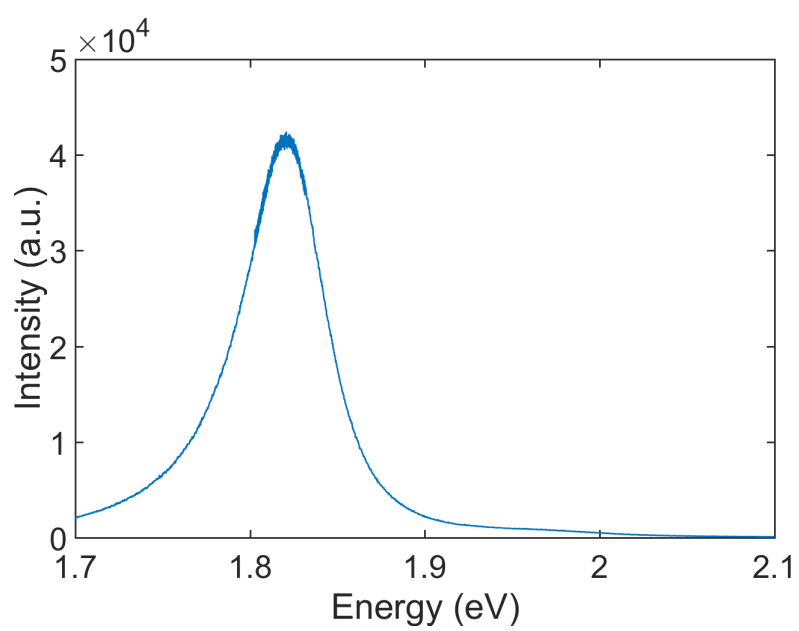


Figure 56: PL spectrum of MoS_2 monolayer

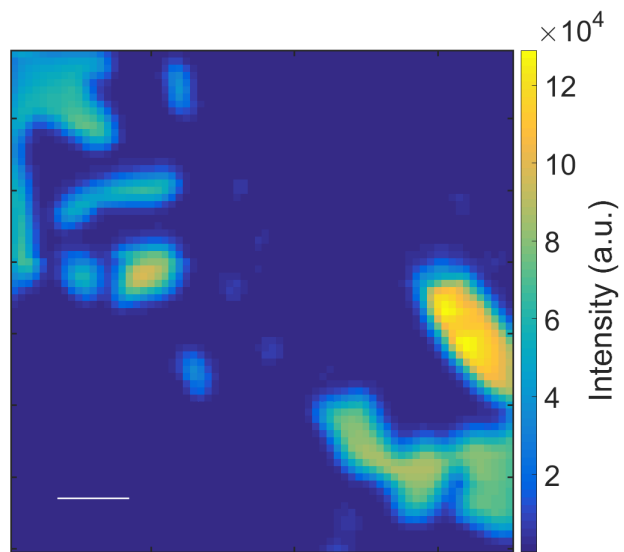


Figure 57: Integrated PL intensity

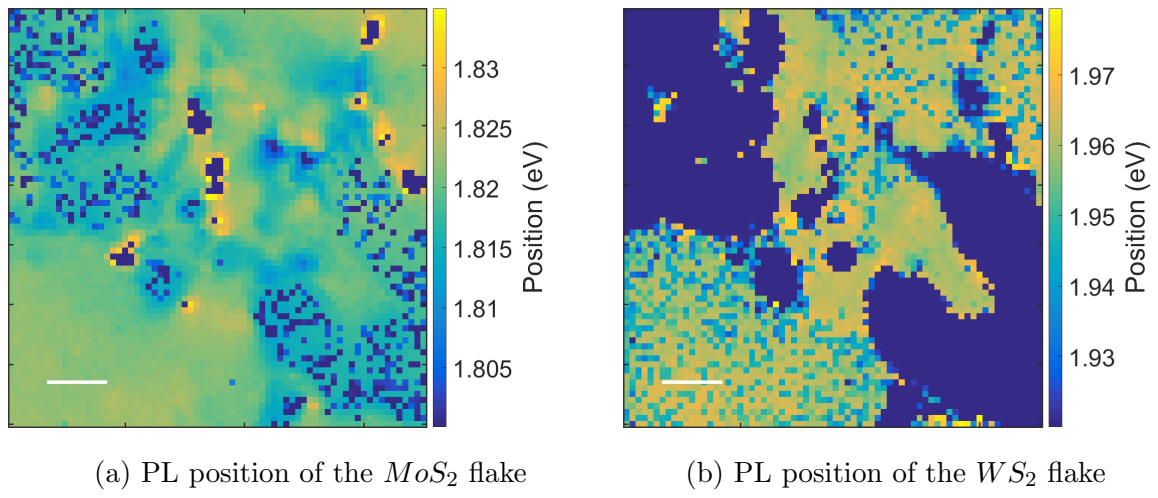


Figure 58: Map of PL peak positions

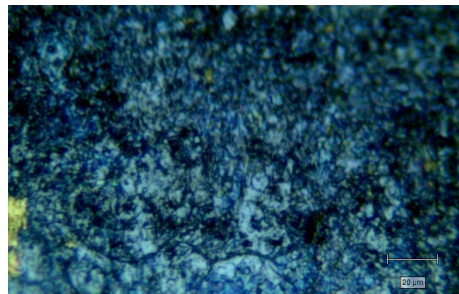


Figure 59: Optical micrograph of the WS_2/MoS_2 grown on gold substrate

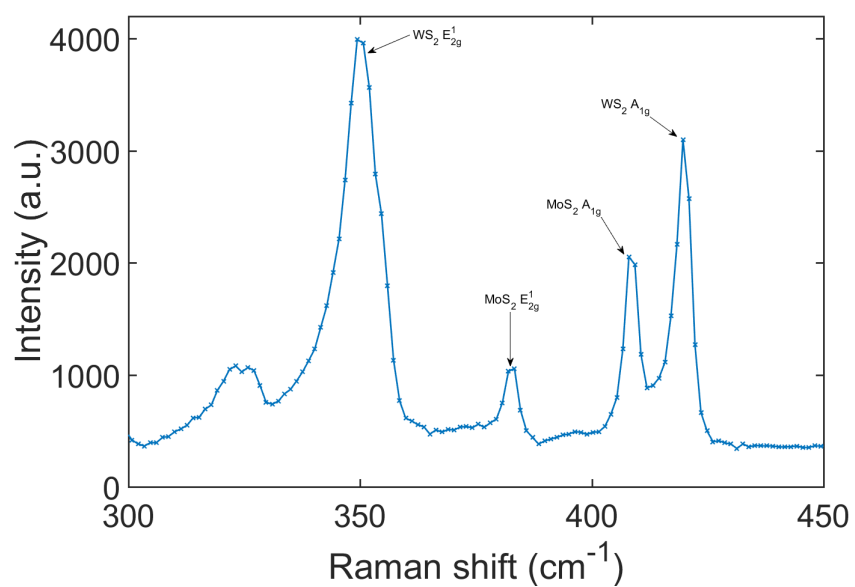


Figure 60: Raman spectrum of WS_2/MoS_2 on gold substrate

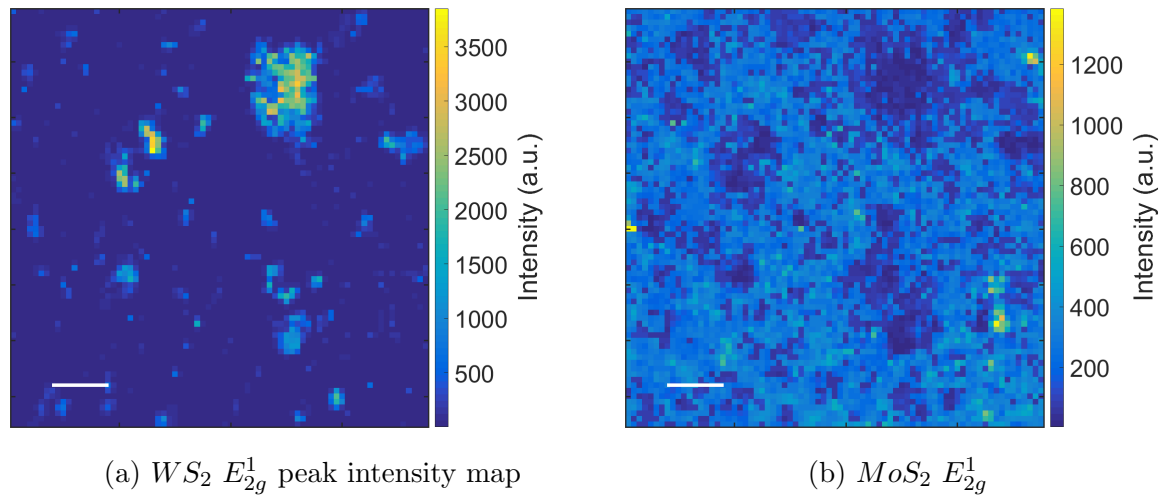


Figure 61: Raman E_{2g}^1 intensity maps

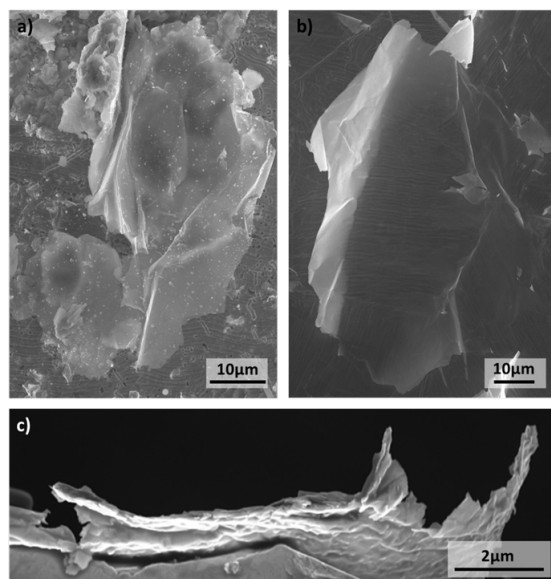


Figure 62: Scanning electron micrograph of (a,b) large lateral size flakes; and (c) cross-sectional area on gold foil

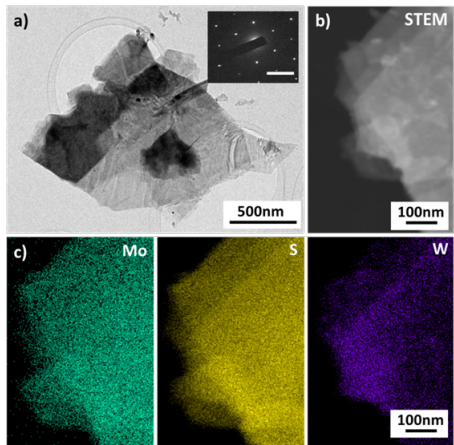


Figure 63: (a) Transmission electron micrograph of heterostructures flakes exfoliated via bath sonication in ethanol, post PEC characterization (inset: diffraction pattern taken from a molybdenum-rich area of the flake, scale bar = 5 nm^{-1}); (b) ADF-STEM image used for EDS spectral mapping; and (c) EDS spectral maps of intensity for Mo, S, W and the corresponding to (b) W and Mo localization in individual stacked flakes.

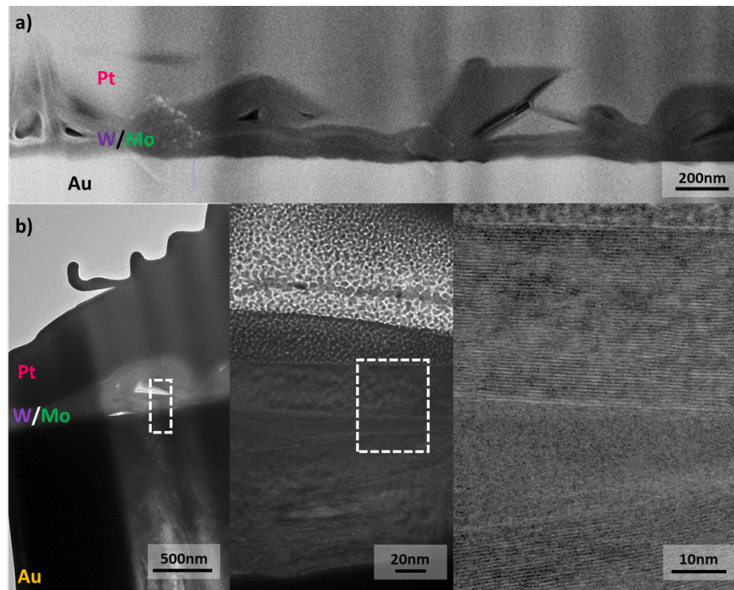


Figure 64: TEM images of FIB-extracted sample attained using the lift-out technique, showing film thickness of less than $1\mu\text{m}$, vertical growth modes, and crystalline flakes; (a) SEM image (visible squares correspond to HRTEM and STEM/EDS regions); and (b) sequential TEM images at increasing magnification.

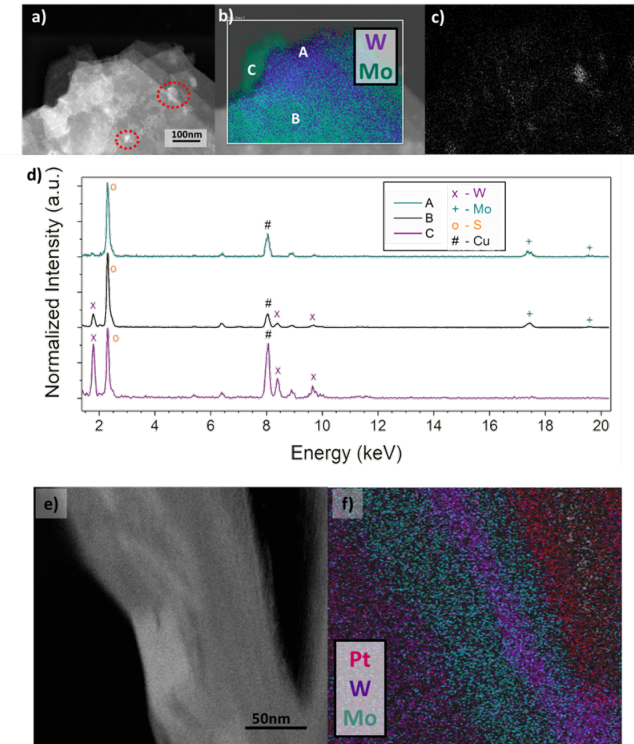


Figure 65: (a) STEM image of 2D crystal heterostructure post-PEC cycling; (b) overlap of EDS maps of W (purple) and Mo (cyan) highlighting localization of both elements in separate yet overlapped layers; (c) oxygen EDS signal post-PEC; (d) individual EDS spectra extracted from regions A, B, and C as highlighted in (b); (e) FIB-STEM of an equivalent flake structure to (a); and (f) EDS map of (d) showing W localization within Mo layers (S not shown for clarity). It should be noted that assignment of W, Au, and S signal required deconvolution using Aztec EDS software due to the overlap between W, Au, and S lines.

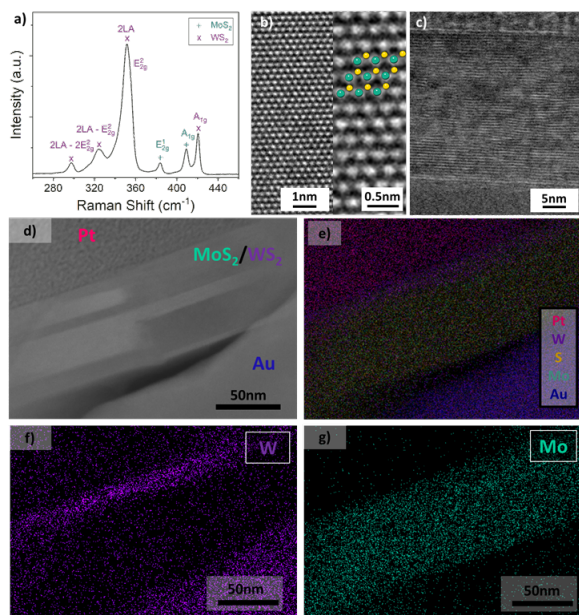


Figure 66: (a) Raman spectrum with independent modes of WS_2 and MoS_2 representative of heterostructure formation; (b) high-resolution TEM image with an atomic model overlaid showing crystallinity; (c) cross-sectional TEM obtained from a FIB cut sample; FIB-STEM-EDS mapping of a MoS_2/WS_2 heterostructure; d) STEM image; e) composite overlaid map showing sequentially: substrate (Au), MoS_2 layer, WS_2 layer; and protective Pt coating; and individual EDS maps for f) W; and g) Mo.

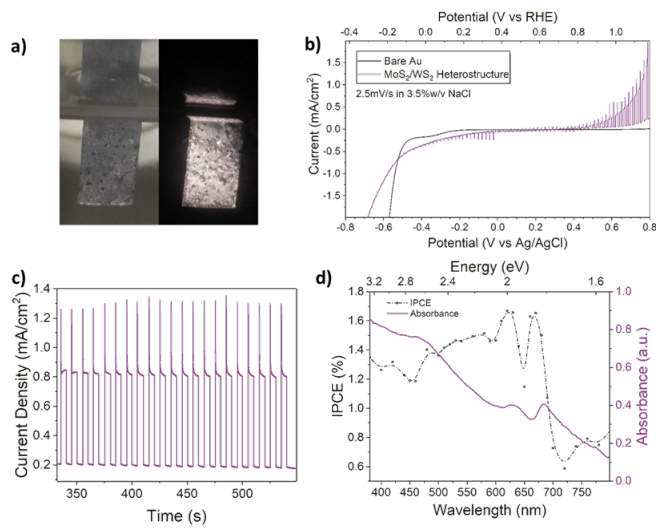


Figure 67: Photoelectrochemical characterisation of MoS₂/WS₂ heterostructure on gold in 3.5% w/v NaCl in DI water; (a) Photograph of active electrode at +0.75 V vs Ag/AgCl, left: no-illumination, right: illuminated, showing gas bubble formation; (b) linear sweep voltammetry at 2.5 mV/s from +0.8 to -0.8 V vs Ag/AgCl demonstrating the complete protection of the Au surface as minimal noble-metal hydrogen evolution is observed and negligible contribution of the substrate to either dark or photocurrent in the water oxidation region; (c) chronoamperometry at +0.75 V vs Ag/AgCl with chopped illumination at 0.2 Hz; and (d) photocurrent dependence on monochromatic light at +0.75 V vs Ag/AgCl and corresponding absorbance spectra of the heterostructures dispersed via sonication in ethanol.

12 Conclusions

References

Appendix

Publications

F. Reale *et al.*, "High-Mobility and High-Optical Quality Atomically Thin WS_2 " *Scientific Reports*, 2017 - submitted

F. M. Pesci *et al.*, "MoS₂/WS₂ heterojunction for photoelectrochemical water oxidation", *ACS Catalysis*, 2017 - accepted

Conferences

Graphene Week, 13-17 June, 2016. (Best poster)

UK Semiconductors, 14-15 July, 2017.

MRS Boston, 26 November - 1 December, 2017.

References

- [1] Evgeny M. Alexeev, David A. Ruiz-Tijerina, Mark Danovich, Matthew J. Hamer, Daniel J. Terry, Pramoda K. Nayak, Seongjoon Ahn, Sangyeon Pak, Juwon Lee, Jung Inn Sohn, Maciej R. Molas, Maciej Koperski, Kenji Watanabe, Takashi Taniguchi, Kostya S. Novoselov, Roman V. Gorbachev, Hyeyon Suk Shin, Vladimir I. Fal'ko, and Alexander I. Tartakovskii. Resonantly hybridized excitons in moiré superlattices in van der waals heterostructures. *Nature*, 567(7746):81–86, mar 2019.
- [2] Abdullah Alharbi and Davood Shahrjerdi. Electronic properties of monolayer tungsten disulfide grown by chemical vapor deposition. *Applied Physics Letters*, 109(19):193502, nov 2016.

- [3] M. Amani, D.-H. Lien, D. Kiriya, J. Xiao, A. Azcatl, J. Noh, S. R. Madhvapathy, R. Addou, S. KC, M. Dubey, K. Cho, R. M. Wallace, S.-C. Lee, J.-H. He, J. W. Ager, X. Zhang, E. Yablonovitch, and A. Javey. Near-unity photoluminescence quantum yield in MoS₂. *Science*, 350(6264):1065–1068, nov 2015.
- [4] Marco Bernardi, Maurizia Palummo, and Jeffrey C. Grossman. Extraordinary sun-light absorption and one nanometer thick photovoltaics using two-dimensional mono-layer materials. *Nano Letters*, 13(8):3664–3670, Aug 2013.
- [5] Claire J. Carmalt, Ivan P. Parkin, and Emily S. Peters. Atmospheric pressure chemical vapour deposition of WS₂ thin films on glass. *Polyhedron*, 22(11):1499–1505, jun 2003.
- [6] Mattia Cattelan, Brian Markman, Giacomo Lucchini, Pranab Kumar Das, Ivana Vobornik, Joshua Alexander Robinson, Stefano Agnoli, and Gaetano Granozzi. New strategy for the growth of complex heterostructures based on different 2d materials. *Chemistry of Materials*, 27(11):4105–4113, may 2015.
- [7] Hailong Chen, Xiewen Wen, Jing Zhang, Tianmin Wu, Yongji Gong, Xiang Zhang, Jiangtan Yuan, Chongyue Yi, Jun Lou, Pulickel M. Ajayan, Wei Zhuang, Guangyu Zhang, and Junrong Zheng. Ultrafast formation of interlayer hot excitons in atomically thin MoS₂/WS₂ heterostructures. *Nature Communications*, 7(1), aug 2016.
- [8] Kun Chen, Xi Wan, Jinxiu Wen, Weiguang Xie, Zhiwen Kang, Xiaoliang Zeng, Huan-jun Chen, and Jian-Bin Xu. Electronic properties of MoS₂–WS₂ heterostructures synthesized with two-step lateral epitaxial strategy. *ACS Nano*, 9(10):9868–9876, sep 2015.
- [9] Chunxiao Cong, Jingzhi Shang, Xing Wu, Bingchen Cao, Namphung Peimyoo, Caiyu Qiu, Litao Sun, and Ting Yu. Synthesis and optical properties of large-area single-crystalline 2d semiconductor WS₂monolayer from chemical vapor deposition. *Advanced Optical Materials*, 2(2):131–136, dec 2013.
- [10] Yang Cui, Run Xin, Zhihao Yu, Yiming Pan, Zhun-Yong Ong, Xiaoxu Wei, Junzhuan Wang, Haiyan Nan, Zhenhua Ni, Yun Wu, Tangsheng Chen, Yi Shi, Baigeng Wang, Gang Zhang, Yong-Wei Zhang, and Xinran Wang. High-performance monolayer WS₂field-effect transistors on high- κ dielectrics. *Advanced Materials*, 27(35):5230–5234, aug 2015.

- [11] A. M. Dadgar, D. Scullion, K. Kang, D. Esposito, E. H. Yang, I. P. Herman, M. A. Pimenta, E.-J. G. Santos, and A. N. Pasupathy. Strain engineering and raman spectroscopy of monolayer transition metal dichalcogenides. *Chemistry of Materials*, 30(15):5148–5155, jul 2018.
- [12] Sarah M. Eichfeld, Lorraine Hossain, Yu-Chuan Lin, Aleksander F. Piasecki, Benjamin Kupp, A. Glen Birdwell, Robert A. Burke, Ning Lu, Xin Peng, Jie Li, Angelica Azcatl, Stephen McDonnell, Robert M. Wallace, Moon J. Kim, Theresa S. Mayer, Joan M. Redwing, and Joshua A. Robinson. Highly scalable, atomically thin WSe₂ grown via metal–organic chemical vapor deposition. *ACS Nano*, 9(2):2080–2087, feb 2015.
- [13] Ana Laura Elías, Néstor Perea-López, Andrés Castro-Beltrán, Ayse Berkdemir, Ruitao Lv, Simin Feng, Aaron D. Long, Takuya Hayashi, Yoong Ahm Kim, Morinobu Endo, Humberto R. Gutiérrez, Nihar R. Pradhan, Luis Balicas, Thomas E. Mallouk, Florentino López-Urías, Humberto Terrones, and Mauricio Terrones. Controlled synthesis and transfer of large-area ws₂ sheets: From single layer to few layers. *ACS Nano*, 7(6):5235–5242, 2013. PMID: 23647141.
- [14] Meyer L. Freedman. The tungstic acids. *Journal of the American Chemical Society*, 81(15):3834–3839, aug 1959.
- [15] Qi Fu, Wenhui Wang, Lei Yang, Jian Huang, Jingyu Zhang, and Bin Xiang. Controllable synthesis of high quality monolayer WS₂ on a SiO₂/si substrate by chemical vapor deposition. *RSC Advances*, 5(21):15795–15799, 2015.
- [16] Yang Gao, Zhibo Liu, Dong-Ming Sun, Le Huang, Lai-Peng Ma, Li-Chang Yin, Teng Ma, Zhiyong Zhang, Xiu-Liang Ma, Lian-Mao Peng, Hui-Ming Cheng, and Wencai Ren. Large-area synthesis of high-quality and uniform monolayer WS₂ on reusable au foils. *Nature Communications*, 6(1), oct 2015.
- [17] Thanasis Georgiou, Huafeng Yang, Rashid Jalil, James Chapman, Kostya S. Novoselov, and Artem Mishchenko. Electrical and optical characterization of atomically thin WS₂. *Dalton Transactions*, 43(27):10388, 2014.
- [18] Yongji Gong, Junhao Lin, Xingli Wang, Gang Shi, Sidong Lei, Zhong Lin, Xiaolong Zou, Gonglan Ye, Robert Vajtai, Boris I. Yakobson, Humberto Terrones, Mauricio Terrones, Beng Kang Tay, Jun Lou, Sokrates T. Pantelides, Zheng Liu, Wu Zhou,

- and Pulickel M. Ajayan. Vertical and in-plane heterostructures from WS₂/MoS₂ monolayers. *Nature Materials*, 13(12):1135–1142, sep 2014.
- [19] Yongji Gong, Zhong Lin, Gonglan Ye, Gang Shi, Simin Feng, Yu Lei, Ana Laura Elías, Nestor Perea-Lopez, Robert Vajtai, Humberto Terrones, Zheng Liu, Mauricio Terrones, and Pulickel M. Ajayan. Tellurium-assisted low-temperature synthesis of MoS₂ and WS₂ monolayers. *ACS Nano*, 9(12):11658–11666, nov 2015.
- [20] Humberto R. Gutiérrez, Nestor Perea-López, Ana Laura Elías, Ayse Berkdemir, Bei Wang, Ruitao Lv, Florentino López-Urías, Vincent H. Crespi, Humberto Terrones, and Mauricio Terrones. Extraordinary room-temperature photoluminescence in triangular ws₂ monolayers. *Nano Letters*, 13(8):3447–3454, dec 2013. PMID: 23194096.
- [21] Wolfgang K. Hofmann. Thin films of molybdenum and tungsten disulphides by metal organic chemical vapour deposition. *Journal of Materials Science*, 23(11):3981–3986, nov 1988.
- [22] Xiaoping Hong, Jonghwan Kim, Su-Fei Shi, Yu Zhang, Chenhao Jin, Yinghui Sun, Sefaattin Tongay, Junqiao Wu, Yanfeng Zhang, and Feng Wang. Ultrafast charge transfer in atomically thin MoS₂/WS₂ heterostructures. *Nature Nanotechnology*, 9(9):682–686, aug 2014.
- [23] Peng Hu, Jun Ye, Xuexia He, Kezhao Du, Keke K. Zhang, Xingzhi Wang, Qihua Xiong, Zheng Liu, Hui Jiang, and Christian Kloc. Control of radiative exciton recombination by charge transfer induced surface dipoles in MoS₂ and WS₂ monolayers. *Scientific Reports*, 6(1), apr 2016.
- [24] Xuan Hu, Poya Yasaee, Jacob Jokisaari, Serdar Öğüt, Amin Salehi-Khojin, and Robert F. Klie. Mapping thermal expansion coefficients in freestanding 2d materials at the nanometer scale. *Physical Review Letters*, 120(5), feb 2018.
- [25] Wang Yao Di Xiao Hualing Zeng, Junfeng Dai and Xiaodong Cui. Valley polarization in mos₂ monolayers by optical pumping. *Nature Nanotechnology*, 7(8):490–493, jun 2012.
- [26] Yeung Yu Hui, Xiaofei Liu, Wenjing Jie, Ngai Yui Chan, Jianhua Hao, Yu-Te Hsu, Lain-Jong Li, Wanlin Guo, and Shu Ping Lau. Exceptional tunability of band energy in a compressively strained trilayer MoS₂ sheet. *ACS Nano*, 7(8):7126–7131, jul 2013.

- [27] Aftab M. Hussain, Galo A. Torres Sevilla, Kelly R. Rader, and Muhammad M. Hussain. Chemical vapor deposition based tungsten disulfide (WS_2) thin film transistor. In *2013 Saudi International Electronics, Communications and Photonics Conference*. IEEE, apr 2013.
- [28] M Waqas Iqbal, M Zahir Iqbal, M Farooq Khan, M Arslan Shehzad, Yongho Seo, Jong Hyun Park, Chanyong Hwang, and Jonghwa Eom. High-mobility and air-stable single-layer WS_2 field-effect transistors sandwiched between chemical vapor deposition-grown hexagonal BN films. *Scientific Reports*, 5(1), jun 2015.
- [29] Muhammad Waqas Iqbal, Muhammad Zahir Iqbal, Muhammad Farooq Khan, Muhammad Arshad Kamran, Abdul Majid, Thamer Alharbi, and Jonghwa Eom. Tailoring the electrical and photo-electrical properties of a WS_2 field effect transistor by selective n-type chemical doping. *RSC Advances*, 6(29):24675–24682, 2016.
- [30] Muhammad Waqas Iqbal, Muhammad Zahir Iqbal, Muhammad Farooq Khan, Muhammad Arslan Shehzad, Yongho Seo, and Jonghwa Eom. Deep-ultraviolet-light-driven reversible doping of WS_2 field-effect transistors. *Nanoscale*, 7(2):747–757, 2015.
- [31] Sanghyun Jo, Nicolas Ubrig, Helmuth Berger, Alexey B. Kuzmenko, and Alberto F. Morpurgo. Mono- and bilayer ws2 light-emitting transistors. *Nano Letters*, 14(4):2019–2025, 2014. PMID: 24669957.
- [32] Kibum Kang, Saien Xie, Lujie Huang, Yimo Han, Pinshane Y. Huang, Kin Fai Mak, Cheol-Joo Kim, David Muller, and Jiwoong Park. High-mobility three-atom-thick semiconducting films with wafer-scale homogeneity. *Nature*, 520(7549):656–660, apr 2015.
- [33] Kyung Nam Kang, Kyle Godin, and Eui-Hyeok Yang. The growth scale and kinetics of WS_2 monolayers under varying h₂ concentration. *Scientific Reports*, 5(1), aug 2015.
- [34] A. Kuc, N. Zibouche, and T. Heine. Influence of quantum confinement on the electronic structure of the transition metal sulfide ts_2 . *Phys. Rev. B*, 83(24):245213, Jun 2011.

- [35] Jens Kunstmann, Fabian Mooshammer, Philipp Nagler, Andrey Chaves, Frederick Stein, Nicola Paradiso, Gerd Plechinger, Christoph Strunk, Christian Schüller, Gotthard Seifert, David R. Reichman, and Tobias Korn. Momentum-space indirect interlayer excitons in transition-metal dichalcogenide van der waals heterostructures. *Nature Physics*, 14(8):801–805, apr 2018.
- [36] Changyong Lan, Chun Li, Yi Yin, and Yong Liu. Large-area synthesis of monolayer WS₂and its ambient-sensitive photo-detecting performance. *Nanoscale*, 7(14):5974–5980, 2015.
- [37] Yi-Hsien Lee, Lili Yu, Han Wang, Wenjing Fang, Xi Ling, Yumeng Shi, Cheng-Te Lin, Jing-Kai Huang, Mu-Tung Chang, Chia-Seng Chang, Mildred Dresselhaus, Tomas Palacios, Lain-Jong Li, and Jing Kong. Synthesis and transfer of single-layer transition metal disulfides on diverse surfaces. *Nano Letters*, 13(4):1852–1857, mar 2013.
- [38] Shisheng Li, Shunfeng Wang, Dai-Ming Tang, Weijie Zhao, Huilong Xu, Leiqiang Chu, Yoshio Bando, Dmitri Golberg, and Goki Eda. Halide-assisted atmospheric pressure growth of large WSe₂ and WS₂ monolayer crystals. *Applied Materials Today*, 1(1):60–66, nov 2015.
- [39] Tianshu Li and Giulia Galli. Electronic properties of mos₂ nanoparticles. *The Journal of Physical Chemistry C*, 111(44):16192–16196, nov 2007.
- [40] Xinru Li, Ying Dai, Mengmeng Li, Wei Wei, and Baibiao Huang. Stable si-based pentagonal monolayers: high carrier mobilities and applications in photocatalytic water splitting. *Journal of Materials Chemistry A*, 3(47):24055–24063, 2015.
- [41] Yilei Li, Yi Rao, Kin Fai Mak, Yumeng You, Shuyuan Wang, Cory R. Dean, and Tony F. Heinz. Probing symmetry properties of few-layer mos₂ and h.bn by optical second-harmonic generation. *Nano Letters*, 13(7):3329–3333, jun 2013. PMID: 23718906.
- [42] Liangxu Lin, Yaoxian Xu, Shaowei Zhang, Ian M. Ross, Albert C. M. Ong, and Dan A. Allwood. Fabrication of luminescent monolayered tungsten dichalcogenides quantum dots with giant spin-valley coupling. *ACS Nano*, 7(9):8214–8223, 2013. PMID: 23968363.

- [43] Hongwei Liu, Junpeng Lu, Kenneth Ho, Zhenliang Hu, Zhiya Dang, Alexandra Carvalho, Hui Ru Tan, Eng Soon Tok, and Chorng Haur Sow. Fluorescence concentric triangles: A case of chemical heterogeneity in WS₂ atomic monolayer. *Nano Letters*, 16(9):5559–5567, aug 2016.
- [44] Zheng Liu, Matin Amani, Sina Najmaei, Quan Xu, Xiaolong Zou, Wu Zhou, Ting Yu, Caiyu Qiu, A. Glen Birdwell, Frank J. Crowne, Robert Vajtai, Boris I. Yakobson, Zhenhai Xia, Madan Dubey, Pulickel M. Ajayan, and Jun Lou. Strain and structure heterogeneity in MoS₂ atomic layers grown by chemical vapour deposition. *Nature Communications*, 5(1), nov 2014.
- [45] He Keliang Lee Changgu Lee Gwan Hyoung Hone James Heinz Tony F. Mak, Kin Fai and Jie Shan. Tightly bound trions in monolayer. *Nature Materials*, 12(3):207–211, dec 2013.
- [46] He Keliang Shan Jie Mak, Kin Fai and Tony F. Heinz. Control of valley polarization in monolayer mos₂ by optical helicity. *Nature Nanotechnology*, 7(8):494–498, jun 2012.
- [47] Kin Fai Mak, Changgu Lee, James Hone, Jie Shan, and Tony F. Heinz. Atomically thin mos₂: A new direct-gap semiconductor. *Phys. Rev. Lett.*, 105(13):136805, Sep 2010.
- [48] H. Martinez, A. Benayad, D. Gonbeau, P. Vinatier, B. Pecquenard, and A. Levasseur. Influence of the cation nature of high sulfur content oxysulfide thin films MOySz (m=w, ti) studied by XPS. *Applied Surface Science*, 236(1-4):377–386, sep 2004.
- [49] Mitsuhiro Okada, Takumi Sawazaki, Kenji Watanabe, Takashi Taniguchi, Hiroki Hibino, Hisanori Shinohara, and Ryo Kitaura. Direct chemical vapor deposition growth of ws₂ atomic layers on hexagonal boron nitride. *ACS Nano*, 8(8):8273–8277, 2014. PMID: 25093606.
- [50] Dmitry Ovchinnikov, Adrien Allain, Ying-Sheng Huang, Dumitru Dumcenco, and Andras Kis. Electrical transport properties of single-layer WS₂. *ACS Nano*, 8(8):8174–8181, jul 2014.
- [51] Eric Parzinger, Bastian Miller, Benno Blaschke, Jose A. Garrido, Joel W. Ager, Alexander Holleitner, and Ursula Wurstbauer. Photocatalytic stability of single- and few-layer MoS₂. *ACS Nano*, 9(11):11302–11309, nov 2015.

- [52] Namphung Peimyoo, Jingzhi Shang, Chunxiao Cong, Xiaonan Shen, Xiangyang Wu, Edwin K. L. Yeow, and Ting Yu. Nonblinking, intense two-dimensional light emitter: Monolayer ws₂ triangles. *ACS Nano*, 7(12):10985–10994, 2013. PMID: 24266716.
- [53] Namphung Peimyoo, Weihuang Yang, Jingzhi Shang, Xiaonan Shen, Yanlong Wang, and Ting Yu. Chemically driven tunable light emission of charged and neutral excitons in monolayer WS₂. *ACS Nano*, 8(11):11320–11329, oct 2014.
- [54] Federico M. Pesci, Maria S. Sokolikova, Chiara Grotta, Peter C. Sherrell, Francesco Reale, Kanudha Sharda, Na Ni, Pawel Palczynski, and Cecilia Mattevi. MoS₂/WS₂ heterojunction for photoelectrochemical water oxidation. *ACS Catalysis*, 7(8):4990–4998, jul 2017.
- [55] Filip A. Rasmussen and Kristian S. Thygesen. Computational 2d materials database: Electronic structure of transition-metal dichalcogenides and oxides. *The Journal of Physical Chemistry C*, 119(23):13169–13183, jun 2015.
- [56] Faizan Raza, Jung Hyun Park, Hye-Rim Lee, Hye-In Kim, Su-Ji Jeon, and Jong-Ho Kim. Visible-light-driven oxidative coupling reactions of amines by photoactive WS₂ nanosheets. *ACS Catalysis*, 6(5):2754–2759, mar 2016.
- [57] Francesco Reale, Pawel Palczynski, Iddo Amit, Gareth F. Jones, Jake D. Mehew, Agnes Bacon, Na Ni, Peter C. Sherrell, Stefano Agnoli, Monica F. Craciun, Saverio Russo, and Cecilia Mattevi. High-mobility and high-optical quality atomically thin WS 2. *Scientific Reports*, 7(1), nov 2017.
- [58] Youmin Rong, Ye Fan, Ai Leen Koh, Alex W. Robertson, Kuang He, Shanshan Wang, Haijie Tan, Robert Sinclair, and Jamie H. Warner. Controlling sulphur precursor addition for large single crystal domains of WS₂. *Nanoscale*, 6(20):12096–12103, sep 2014.
- [59] Prasana K. Sahoo, Shahriar Memaran, Yan Xin, Luis Balicas, and Humberto R. Gutiérrez. One-pot growth of two-dimensional lateral heterostructures via sequential edge-epitaxy. *Nature*, 553(7686):63–67, jan 2018.
- [60] Jingzhi Shang, Xiaonan Shen, Chunxiao Cong, Namphung Peimyoo, Bingchen Cao, Mustafa Eginligil, and Ting Yu. Observation of excitonic fine structure in a 2d transition-metal dichalcogenide semiconductor. *ACS Nano*, 9(1):647–655, 2015. PMID: 25560634.

- [61] Jianping Shi, Donglin Ma, Gao-Feng Han, Yu Zhang, Qingqing Ji, Teng Gao, Jingyu Sun, Xiuju Song, Cong Li, Yanshuo Zhang, Xing-You Lang, Yanfeng Zhang, and Zhongfan Liu. Controllable growth and transfer of monolayer MoS₂ on au foils and its potential application in hydrogen evolution reaction. *ACS Nano*, 8(10):10196–10204, sep 2014.
- [62] Kevin Sivula and Roel van de Krol. Semiconducting materials for photoelectrochemical energy conversion. *Nature Reviews Materials*, 1(2), jan 2016.
- [63] Andrea Splendiani, Liang Sun, Yuanbo Zhang, Tianshu Li, Jonghwan Kim, Chi-Yung Chim, Giulia Galli, and Feng Wang. Emerging photoluminescence in monolayer mos2. *Nano Letters*, 10(4):1271–1275, apr 2010. PMID: 20229981.
- [64] Haruna Tada, Amy E. Kumpel, Richard E. Lathrop, John B. Slanina, Patricia Nieva, Paul Zavracky, Ioannis N. Miaoulis, and Peter Y. Wong. Thermal expansion coefficient of polycrystalline silicon and silicon dioxide thin films at high temperatures. *Journal of Applied Physics*, 87(9):4189–4193, may 2000.
- [65] Chaoliang Tan, Junze Chen, Xue-Jun Wu, and Hua Zhang. Epitaxial growth of hybrid nanostructures. *Nature Reviews Materials*, 3(2), jan 2018.
- [66] Xiaona Liu Pingheng Tan Tengfei Yan, Xiaofen Qiao and Xinhui Zhang. Photoluminescence properties and exciton dynamics in monolayer wse₂. *Applied Physics Letters*, 105(10):101901, sep 2014.
- [67] Sefaattin Tongay, Joonki Suh, Can Ataca, Wen Fan, Alexander Luce, Jeong Seuk Kang, Jonathan Liu, Changhyun Ko, Rajamani Raghunathanan, Jian Zhou, Frank Ogletree, Jingbo Li, Jeffrey C. Grossman, and Junqiao Wu. Defects activated photoluminescence in two-dimensional semiconductors: interplay between bound, charged and free excitons. *Scientific Reports*, 3(1), sep 2013.
- [68] Damien Voiry, Jieun Yang, and Manish Chhowalla. Recent strategies for improving the catalytic activity of 2d TMD nanosheets toward the hydrogen evolution reaction. *Advanced Materials*, 28(29):6197–6206, feb 2016.
- [69] Qianwen Wang, Ping Wu, Gengyu Cao, and Min Huang. First-principles study of the structural and electronic properties of MoS₂–WS₂and MoS₂–MoTe₂monolayer heterostructures. *Journal of Physics D: Applied Physics*, 46(50):505308, nov 2013.

- [70] Qing Hua Wang, Kourosh Kalantar-Zadeh, Andras Kis, Jonathan N. Coleman, and Michael S. Strano. Electronics and optoelectronics of two-dimensional transition metal dichalcogenides. *Nature Nanotechnology*, 7:699 EP –, Nov 2012. Review Article.
- [71] Kiran Kumar Amara Jing Ren Pang Minglin Toh Xin Zhang Christian Kloc Ping Heng Tane Weijie Zhao, Zohreh Ghorannevis and Goki Eda. Lattice dynamics in mono- and few-layer sheets of ws_2 and wse_2 . *Nanoscale*, 5(20):9677-9683, August 2013.
- [72] J.A. Wilson and A.D. Yoffe. The transition metal dichalcogenides discussion and interpretation of the observed optical, electrical and structural properties. *Advances in Physics*, 18(73):193–335, may 1969.
- [73] F. Withers, O. Del Pozo-Zamudio, A. Mishchenko, A. P. Rooney, A. Gholinia, K. Watanabe, T. Taniguchi, S. J. Haigh, A. K. Geim, A. I. Tartakovskii, and K. S. Novoselov. Light-emitting diodes by band-structure engineering in van der waals heterostructures. *Nature Materials*, 14(3):301–306, feb 2015.
- [74] Freddie Withers, Thomas Hardisty Bointon, David Christopher Hudson, Monica Felicia Craciun, and Saverio Russo. Electron transport of WS₂ transistors in a hexagonal boron nitride dielectric environment. *Scientific Reports*, 4(1), may 2014.
- [75] Ryan J. Wu, Michael L. Odlyzko, and K. Andre Mkhoyan. Determining the thickness of atomically thin MoS₂ and WS₂ in the TEM. *Ultramicroscopy*, 147:8–20, dec 2014.
- [76] Di Xiao, Gui-Bin Liu, Wanxiang Feng, Xiaodong Xu, and Wang Yao. Coupled spin and valley physics in monolayers of mos_2 and other group-vi dichalcogenides. *Phys. Rev. Lett.*, 108(19):196802, May 2012.
- [77] Zai-Quan Xu, Yupeng Zhang, Shenghuang Lin, Changxi Zheng, Yu Lin Zhong, Xue Xia, Zhipeng Li, Ponraj Joice Sophia, Michael S. Fuhrer, Yi-Bing Cheng, and Qiao-liang Bao. Synthesis and transfer of large-area monolayer ws₂ crystals: Moving toward the recyclable use of sapphire substrates. *ACS Nano*, 9(6):6178–6187, 2015. PMID: 25961515.
- [78] Xiaoyun Yu, Néstor Guijarro, Melissa Johnson, and Kevin Sivula. Defect mitigation of solution-processed 2d WSe₂ nanoflakes for solar-to-hydrogen conversion. *Nano Letters*, 18(1):215–222, dec 2017.

- [79] Xiaoyun Yu and Kevin Sivula. Toward large-area solar energy conversion with semi-conducting 2d transition metal dichalcogenides. *ACS Energy Letters*, 1(1):315–322, jun 2016.
- [80] Xiaoyun Yu and Kevin Sivula. Photogenerated charge harvesting and recombination in photocathodes of solvent-exfoliated WSe₂. *Chemistry of Materials*, 29(16):6863–6875, aug 2017.
- [81] Long Yuan and Libai Huang. Exciton dynamics and annihilation in WS₂ 2d semiconductors. *Nanoscale*, 7(16):7402–7408, 2015.
- [82] Seok Joon Yun, Sang Hoon Chae, Hyun Kim, Jin Cheol Park, Ji-Hoon Park, Gang Hee Han, Joo Song Lee, Soo Min Kim, Hye Min Oh, Jinbong Seok, Mun Seok Jeong, Ki Kang Kim, and Young Hee Lee. Synthesis of centimeter-scale monolayer tungsten disulfide film on gold foils. *ACS Nano*, 9(5):5510–5519, apr 2015.
- [83] Longhui Zeng, Lili Tao, Chunyin Tang, Bo Zhou, Hui Long, Yang Chai, Shu Ping Lau, and Yuen Hong Tsang. High-responsivity UV-vis photodetector based on transferable WS₂ film deposited by magnetron sputtering. *Scientific Reports*, 6(1), jan 2016.
- [84] Yu Zhang, Yanfeng Zhang, Qingqing Ji, Jing Ju, Hongtao Yuan, Jianping Shi, Teng Gao, Donglin Ma, Mengxi Liu, Yubin Chen, Xiuju Song, Harold Y. Hwang, Yi Cui, and Zhongfan Liu. Controlled growth of high-quality monolayer ws₂ layers on sapphire and imaging its grain boundary. *ACS Nano*, 7(10):8963–8971, 2013. PMID: 24047054.
- [85] Weijie Zhao, Zohreh Ghorannevis, Leiqiang Chu, Minglin Toh, Christian Kloc, Ping-Heng Tan, and Goki Eda. Evolution of electronic structure in atomically thin sheets of ws₂ and wse₂. *ACS Nano*, 7(1):791–797, dec 2013. PMID: 23256505.
- [86] Z. Y. Zhu, Y. C. Cheng, and U. Schwingenschlögl. Giant spin-orbit-induced spin splitting in two-dimensional transition-metal dichalcogenide semiconductors. *Phys. Rev. B*, 84(15):153402, Oct 2011.